LABORATOIRE NATIONAL DES CHAMPS MAGNETIQUES INTENSES

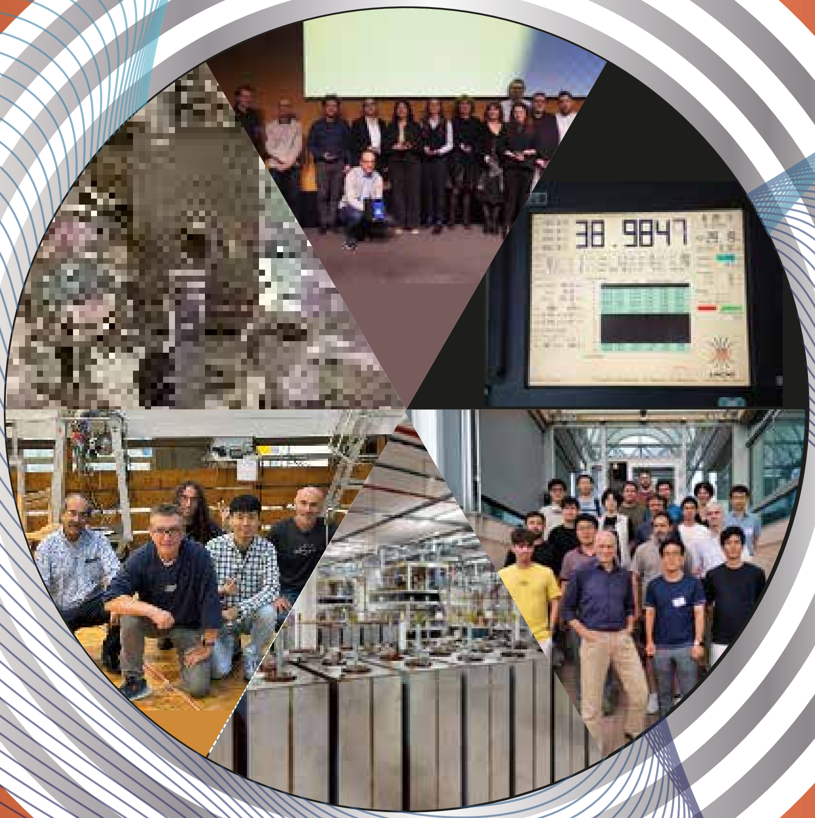

ANNUAL REPORT

2025

Laboratoire National des Champs Magnétiques Intenses

Grenoble–Toulouse

Centre National de la Recherche Scientifique

http://lncmi.cnrs.fr/

Annual Report

2025

LNCMI is formally associated with the "Université Grenoble Alpes", the "Université Paul Sabatier", Toulouse and the "Institut National des Sciences Appliquées", Toulouse.

Typeset using LaTeX
Editor: Duncan K. Maude

Preface

Dear Reader,

It is my pleasure to present you here the 2025 annual report of the Laboratoire National des Champs Magnétiques Intenses (LNCMI). This report aims at providing you a comprehensive overview of our in-house and collaborative science.

LNCMI underwent a major leadership transition in the summer of 2025. Charles Simon stepped down from his role as director at the end of June, and I would like to take this opportunity to introduce myself as his successor. My name is Rolf Lortz, and I have been serving as the new director since July 2025. I joined LNCMI as an external candidate following an academic career at the Hong Kong University of Science & Technology. High magnetic fields have always been central to my research on superconductors and magnetic materials, making LNCMI a natural choice for taking on new challenges and responsibilities at this stage of my career.

I would like to express my sincere gratitude to Charles for his outstanding dedication. Under his leadership, the laboratory has seen remarkable progress; the completion of the new power infrastructure in Grenoble, the renewal of the capacitor banks in Toulouse, and, most notably, the successful construction of the new hybrid magnet, which has already reached 42 T. This achievement establishes a new high-field platform that will soon be available to our user community.

My thanks also go to the other members of the directorate team. Their commitment, hard work and unwavering support has greatly facilitated my transition into this new role.

Magnetic fields serve as a vital control parameter across numerous scientific disciplines in both academia and industry. They enable the exploration of quantum phenomena, such as the quantum Hall effect, and exotic states of condensed matter, support applied research in medical technologies, including cancer treatment, and advanced imaging, drive innovation in energy through superconducting magnets for nuclear fusion, and provide essential tools for testing fundamental theories in particle physics.

A high magnetic field laboratory such as LNCMI has the mission of providing magnetic fields at strengths far beyond what is commercially available to standard research laboratories. Commercial magnet systems typically come in the form of permanent magnets, which reach up to about 1 T, or superconducting coils. While superconducting platforms can exceed 20 T, their cost rises steeply beyond this threshold. Reaching fields approaching 30 T and above requires the dedicated infrastructure of a high magnetic field facility. These magnetic fields are produced using several complementary technologies; resistive magnets capable of delivering static fields up to roughly 40 T, hybrid magnets that extend static fields beyond 40 T, and pulsed-field systems that reach nearly 100 T over short durations of about 100 ms. In addition, LNCMI Toulouse operates a MegaGauss facility that generates fields well above 100 T in a semi-destructive regime, in which the magnet coil is sacrificed while the experimental apparatus remains intact. Such techniques are extremely costly and can only be provided by major research infrastructures like LNCMI.

Generating such extreme fields also demands highly specialized experimental probes, including custom-designed thermometry and sensors, all of which must be developed in-house to withstand the unique constraints of these environments. Only a small number of laboratories worldwide operate facilities capable of producing these field strengths, located in Europe, the USA, China, and Japan. LNCMI is one of these few centers, and forms, together with HFML-FELIX in Nijmegen and the Hochfeld-Magnetlabor Dresden (HLD), the European Magnetic Field Laboratory (EMFL).

Like many major research infrastructures across Europe, LNCMI is navigating significant challenges, especially those linked to the climate emergency and the ongoing energy crisis. Thanks to sustained investments in advanced materials and innovative techniques in recent years, we are now exceptionally well positioned to deliver world-class magnetic field capabilities, as detailed in this report. We remain confident that LNCMI will continue to be a key contributor to scientific progress in the years ahead.

Rolf Lortz
January 2026

CONTENTS

LIST OF FIGURES

The LNCMI user facility

INTRODUCTION

The Laboratoire National des Champs Magnétiques Intenses (LNCMI) is one of the large scale facilities of the CNRS. It works as a research facility available both to its own researchers, as well as to external users. The high field facility is open to users from all over the world.

The LNCMI is also a member of the European Magnetic Field Laboratory (EMFL). EMFL is a legal entity (Association Internationale Sans But Lucratif, AISBL) in Brussels, Belgium, that provides the highest possible fields (both continuous and pulsed) for researchers. EMFL was founded in order to unite, coordinate and reinforce the three existing medium scale European high magnetic field laboratories - the Dresden High Magnetic Field Laboratory (Germany), the Laboratoires National des Champs Magnétiques Intenses in Grenoble and Toulouse (France), and the High Magnetic Field Laboratory in Nijmegen (The Netherlands) - within a single body in order to provide such an infrastructure. The British, Polish and Italian high magnetic field communities have also joined EMFL. The EMFL organization is the single entry point for users to obtain access to all European pulsed and DC field facilities. The access to superconducting magnets is treated separately by each facility.

HIGH MAGNETIC FIELDS AND INSTRUMENTATION AVAILABLE TO THE USERS

The LNCMI has resistive magnets at the Grenoble site, pulsed magnets at the Toulouse site, as well as several superconducting magnets at both sites, achieving continuous magnetic fields up to 37 T (resistive) or 42 T (hybrid), and pulsed fields up to 90 T in which it is possible to install various experimental set-ups. The Toulouse site also operates a Megagauss facility producing pulsed fields up to 180 T in a semi-destructive magnet. Mobile generators and coils, designed for use in combination with other very large scale facilities, produce high fields for users of synchrotron, neutrons sources and intense lasers.

The technical and experimental environment also allows the user to combine very low temperatures and high pressures with very high fields. The laboratory offers a wide variety of instrumentation, allowing measurements in high magnetic fields in the following techniques:

- **Optical spectroscopy and magneto-optics-** optical microscope imaging, birefringence, dichronism and Faraday rotation, (micro-)photoluminescence spectroscopy, (micro-)Raman scattering, (far-)infrared spectroscopy.
- **Thermodynamic properties-** specific heat, thermopower and Nernst-Ettinghausen, DC/AC susceptibility, compensated-coil magnetometry, torque magnetometry, ultrasonic measurements (sound velocity and attenuation).
- **Magnetotransport-** magnetotransport with in-situ sample rotation, critical current of superconductors (wires, tapes and coils),contactless transport (TDO, PDO).
- **Magnetic resonance-** electron spin resonance, nuclear magnetic resonance.
- **Advanced sources-** mobile 1 MJ installation allowing X-rays, laser and neutron scattering under pulsed magnetic fields, levitation, thermometry.
- **Environments-** ^{4}He cryostats (1.5-300 K,) ^{3}He cryostats (down to 300 mK), dilution refrigerators (down to 30-100 mK), thermostats up to 300 °C, high pressure.
- **Other-** Megagauss facility (semi-destructive fields > 170 T).

ACCESS TO THE FACILITIES

Scientists who wish to obtain access to the resistive or pulsed magnets of the LNCMI must apply through the User Portal of the EMFL website (https://emfl.eu/SelCom/login.php). This application is drawn up according to a specific form and provides information demonstrating the relevance of the research work to be undertaken. The application is also used to ensure that the experimental conditions requested can be satisfied. Furthermore, scientists will find a large part dedicated to the user access on the EMFL website that includes relevant details about experimental possibilities with examples, instrumental set-ups and available magnets. More information about the LNCMI facilities as well as practical information for users coming to the LNCMI facilities to perform their experiments can be found on the LNCMI website ((https://lncmi.cnrs.fr/).

For the use of the LNCMI mobile pulsed field facility, users must apply directly to the relevant very large scale facilities (ESRF, ILL, LULI).

Access to the superconducting magnets of the LNCMI goes through an in-house procedure, which is open all year (https://lncmi.cnrs.fr/devenir-utilisateur/).

In the frame of the EMFL-ISABEL project, novel access procedures in order to satisfy the needs of all current and potential users have been developed, implemented and evaluated. These procedures are based on feedback from the user community and on a study of ongoing practices at other research institutions (RIs). They are listed below:

- **Dual access-** introduced in 2021, this procedure allows users to apply, in a single proposal, for access to one of the regional partner facilities of EMFL for preliminary experiments in moderate fields, which if successful are followed by high-field experiments at one of the EMFL high-field facilities. These combined proposals have to be submitted during the regular calls, the EMFL selection committee will judge the pertinence of the low-field experiments and grant conditional access to the EMFL installations.
- **Fast-track access-** introduced in fall 2022, the fast-track access is permanently open for convincingly urgent scientific cases. The request will be evaluated and decided within typically 2 weeks by the EMFL board of directors who may optionally consult one or more EMFL selection committee members, and check the feasibility with the facility manager and the local contact.
- **Technical development access-** introduced in fall 2022, this method is dedicated to the interest of scientists wishing to develop and improve technical installations and metrological procedures that could also be of great interest to other EMFL users. These developments aim at improving the quality of EMFL installations with clear benefit to the wide EMFL user community. Technical proposals must be submitted during the regular call periods and will be evaluated by the EMFL board of directors as a special category. In convincingly urgent cases they can also be submitted using the fast-track access mode.
- **First-time access-** introduced in spring 2022, this access mode aims to lower the barrier for researchers who want to use the EMFL facilities for the first time. EMFL will offer reinforced support in preparing a proposal as well as reinforced on-site support. The first-time access can be combined with regular access proposals or any other access mode listed above.
- **Industrial access-** To meet the needs of industry, EMFL makes its infrastructures available to industrial users. The request can be addressed anytime via a dedicated form on the industry section of the EMFL website.

SUBMITTED PROPOSALS

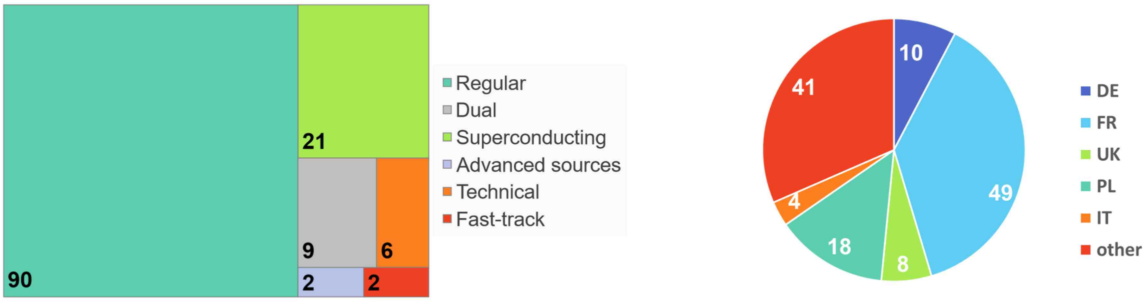

FIG. 1. *(left) Submitted proposals by proposal type and (right) by affiliation country of PI distinguishing EMFL member countries, EMFL partners and other.*

A total of 130 proposals have been submitted in 2025. Figure 1 shows on the left the distribution by proposal type (regular and novel access mode proposals submitted to EMFL, proposals using advanced sources submitted to the very large scale facilities, proposals for superconducting magnets going through the in-house procedure). The right part of figure 1 represents the affiliation country of the principal investigator (PI) by EMFL member countries, EMFL partners and other countries.

In the period 2018 − 2025, 1216 projects have been submitted to the LNCMI, of which 553 proposals were requests for the different configurations of DC resistive magnets at the Grenoble facility, 462 demands for pulsed magnets at the Toulouse facility, 45 for using the mobile capacitor bank in combination with beam-lines at other research institutions and 156 external projects submitted for superconducting magnets (see figure 2). The in-house projects performed on superconducting magnets are not considered here. The particular success of the possibility of working in different bore diameters of the 30 MW DC magnets with fields of 37 T in a 34 mm bore, 31 T in a 50 mm bore and 20 T in a 170 mm bore must be underlined.

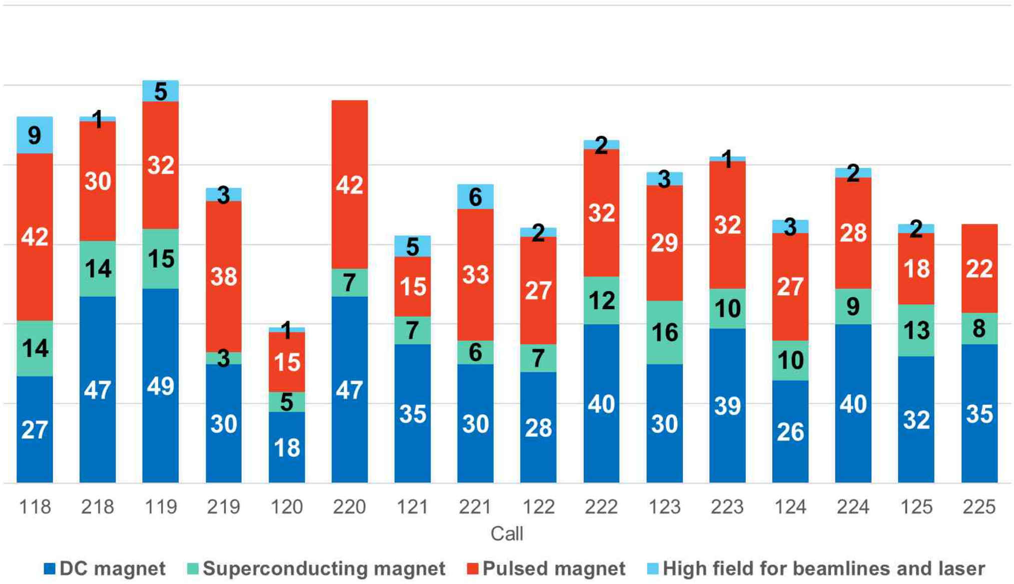

FIG. 2. *Number of projects submitted; the projects on DC magnets use the Grenoble facility, on pulsed magnets the Toulouse facility, the mobile capacitor bank is used in combination with beam-lines or lasers, those on superconducting magnets refer only to the external users at the Grenoble facility.*

Furthermore, some users are particularly interested in large bore diameters such as 130 mm or 376 mm that use 12 MW. These configurations are needed for the development of applied superconductivity, magneto-electrochemistry and magneto-hydrodynamics. The 12 MW magnets can also be used with the standard bore diameters of 34 and 50 mm achieving fields up to 25 T which can be of considerable interest for the preparation of very high field experiments or the development and testing of new experimental set-ups. This allows the LNCMI to offer access for very different types of experiments.

PROPOSAL EVALUATION

The EMFL applications are examined and ranked by the EMFL selection committee, or EMFL board of directors as described above. The evaluation of the proposals is carried out twice a year, in the course of December and at the end of June; fast-track proposals are evaluated at any time. The applications are ranked A, B or C. Projects rated A will be executed, those classified B are performed if the magnet time is available, and applications rated C are rejected. The ranking is made on the same basis for all applications, including those submitted by local scientists. The proposals for using the mobile pulsed field capacitor bank are evaluated directly by the relevant very large scale facility, the projects are rated A (accepted) or C (rejected). Figure 3 shows the high quality of the submitted proposals for the LNCMI sites for 2025, with 37 proposals rated A or A-, 49 rated B+, 18 rated B or B- and only 5 rated C.

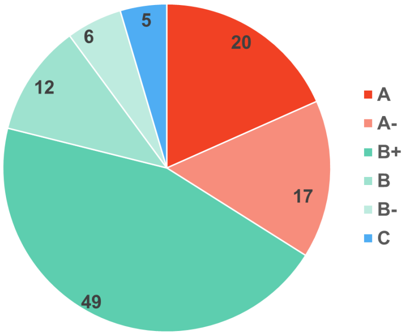

FIG. 3. *Evaluation of proposals submitted in 2025 (EMFL calls 125 and 225).*

Accepted experiments are subsequently programmed during the two semesters following the ranking of the selection committee. If the experiment has not been performed in this period, the principal investigator is required to resubmit the proposal mentioning the reasons why it could not be performed (issue with sample preparation, high pressure on the magnet time schedule, *etc*). The acceptance of an application means that for non-industrial users the entire cost of the experiment (scientific and technical support, electricity, cryogenic fluids, *etc*) will be covered by the budget of the laboratory, for industrial users a financial basis for the performance of the proposal will be defined.

The selection committee is divided into five groups, each with a different area of expertise (semiconductors, metals and superconductors, magnetism, applied superconductors, soft materials). In each area there are international experts from outside the EMFL consortium, as well as scientists from the different high magnetic field laboratories of the EMFL consortium, whose presence ensures that a project can technically be performed in the laboratory.

PERFORMING AN EXPERIMENT

Local contact

When the applicant is informed of the acceptance of his/her proposal, and of the number of pulses/shifts scheduled for the experiment, he/she is at the same time informed of the name of the local contact in charge of facilitating their work at the LNCMI. The local contact is a research scientist or an engineer of the laboratory. If an applicant has not identified a local contact, the laboratory management will appoint a scientist that the user can contact in order to define with him/her the conditions for the organization of the experimental work. The instrumentation groups of both sites of the LNCMI assure the technical support for the experiments.

Operation and magnet time

The periods of operation of the DC field facility, maintenance, work for upgrading and shut-down are fixed one year in advance. In general, the facility is stopped twice a year for maintenance with an additional short break of one week in spring. Further stops of the power installation can be decided for work, upgrading or commissioning a new magnet.

The 21 MJ, 3 MJ and 1 MJ generators are available to users for long pulse experiments. The 90 T multi-stage coils are fully available to users. In 2026, an upgrade of the user facility is planned, the installation will probably be shut down few months during the summer. The megagauss facility will be open to users for optical spectroscopy and magnetization experiments up to 150 T at $T = 10\,\mathrm{K}$ from the middle of 2026.

The magnet time schedule is drawn up for one semester and regularly updated. The demand for the facilities being high, visitors are strongly urged to get in touch with their local contact at the beginning of each semester, in January and in July, to discuss the scheduling of their experiment. LNCMI will do its maximum to satisfy the requests of its users and find the most suitable period for carrying out the experiments. The user support on the magnet sites is assured by the scientific local contacts and the instrumentation team.

The magnets operate on a schedule taking into account the availability of staff, magnets and instrumentation. For the DC field facility, the installation is operational up to 24 hours per day 7 days a week including weekends and bank holidays. In 2025, the experiments were mostly scheduled during daytime or evening with two standard shifts from 9 a.m. to 4 p.m. and 4 p.m. to 11 p.m., and a weekly maintenance on Wednesdays from 9 a.m. to 4 p.m. If needed, the daily shift time can be flexible and adapted to the experiment's needs. An LNCMI operator must be contacted during working hours for any operational request whereas outside normal working hours, a safety agent provides a presence in the laboratory.

Twice a month the technical teams (power facility group, magnet group, instrumentation group, operators etc.) and scientists of the currently scheduled projects come together in an interdisciplinary coordination meeting. This allows the exchange of information (planned experiments and special demands, observed incidents, technical improvements, organization issues etc.) and the coordination of technical interventions.

Regarding the superconducting magnets, the schedule is managed by the relevant scientific teams. The magnet time using the mobile capacitor bank in combination with beam-lines or lasers is directly attributed by the relevant very large scale facility.

ADMINISTRATION, FEEDBACK AND REPORTING

Users are invited to fill out and submit an online Admin form on the User Portal as soon as possible after scheduling of the experiment. The Admin form provides the facility with the information necessary to prepare the visit of the experimental team. The main proposer and all participants on the proposal are listed by default on the Admin form. The form can be modified and additional scientists added. Users will also indicate their travel and accommodation information for each participant. By submitting, the Admin form will be sent to the facility's user support who will take care of accomplishing various formalities (declaring a presence to the central administration, authorizations and access to the campus, IT charter and safety formalities, logistics).

After performing the experiment, the user committee would like to receive feedback in order to constantly improve user access at the EMFL facilities. The feedback form can be filled out online. The data is handled confidentially by the User Committee (https://emfl.eu/emfl-user-organisation/).

Within two months following the experiment, users are required to submit a progress report. It can be filled online via the EMFL User Portal (https://emfl.eu/SelCom/login.php). This report is essential and is requested by the Selection Committee. It is also used to justify the use of the facilities.

ELECTRICITY COSTS & ENERGY MANAGEMENT AT THE DC FIELD FACILITY

Electricity costs

The laboratory has to deal with steeply increasing electricity prices. From 2016 to 2019 the DC field facility bought its own electricity on the open market. Since 2020, the costs for electricity are negotiated at the national level to have a more stable price over one or two years but with the drawback that the high degree of flexibility in power consumption and consequently a more interesting contract cannot be taken into account. The electricity price evolution is shown in figure 4.

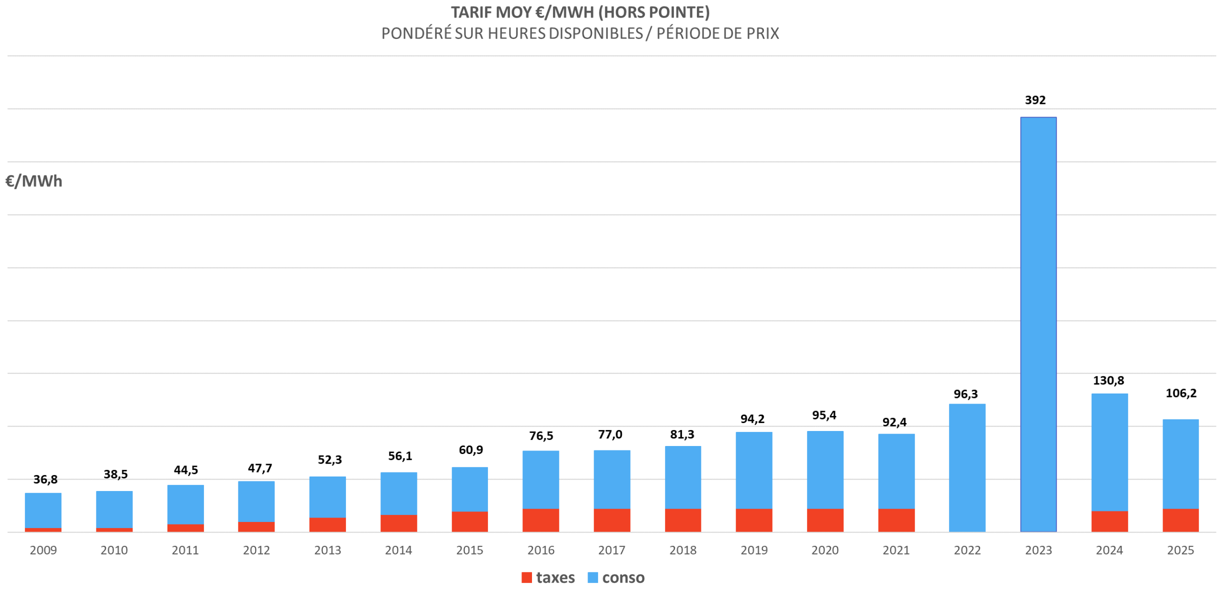

FIG. 4. *Evolution of average electricity price.*

Energy management

The DC field facility has set up different ways to optimize the relation of the number of scientific projects that can be performed with a tighter and tighter energy budget.

Firstly, users are invited to estimate the required field profile in advance with the help of the local contact and the user access manager. A special tool has been developed and can be made available to simulate the field profile and calculate the corresponding power consumption. An electricity consumption is then allocated to each project. Furthermore, a thorough and detailed preparation of each experiment is essential in order to use the available magnet time efficiently.

Secondly, a new magnet operation mode has been developed and is in use since September 2021. It allows reducing the mean power consumption by 10 to 15%, taking advantage of the new materials available for magnets and of advanced piloting of the facility.

PROJECTS CARRIED OUT IN 2025

The statistics presented here summarize the use of the LNCMI facilities in 2025.

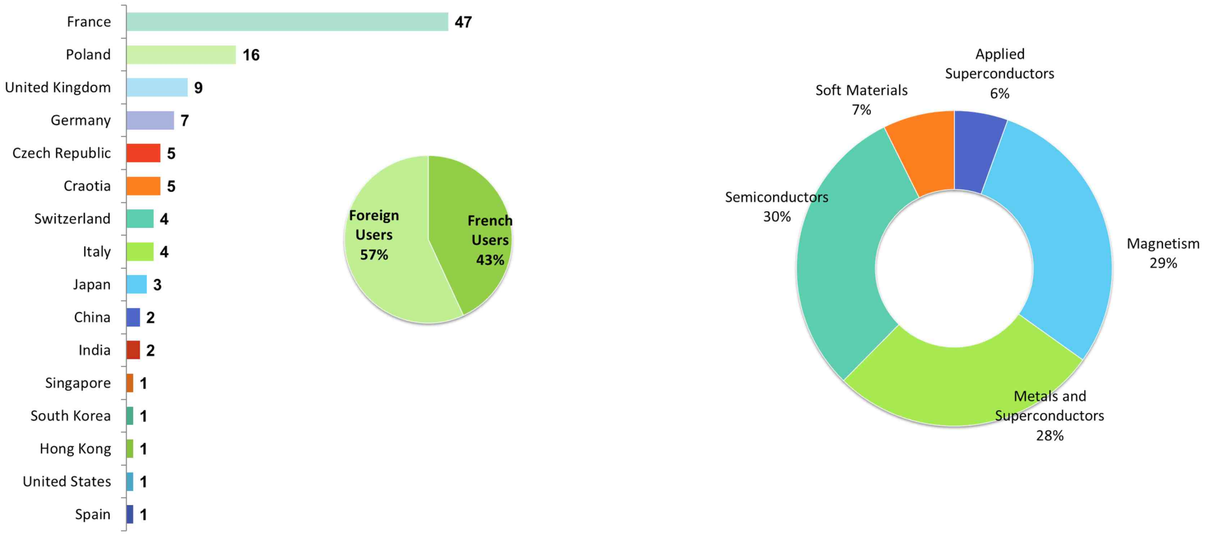

FIG. 5. *Performed proposals in 2025 by country of origin (left) and by research area (right).*

The left panel of figure 5 shows the country of origin of the projects that were performed on all magnets, the resistive, pulsed and superconducting magnets. Most of the projects were performed by scientists outside France. The users came mostly from Poland, Germany, and the United Kingdom who are members or partners of EMFL, but also from Switzerland and followed by users from the Czech Republic and the Netherlands.

Generally, most scientists who have already used our facilities come back regularly, introducing and progressively forming scientists who become themselves, in turn, new users. Nevertheless, every year the laboratory also welcomes completely new users. The projects realized at the LNCMI facilities are thematically distributed as shown in the right panel of figure 5 with focus on projects in the semiconductors, the metals and superconductors and the magnetism areas.

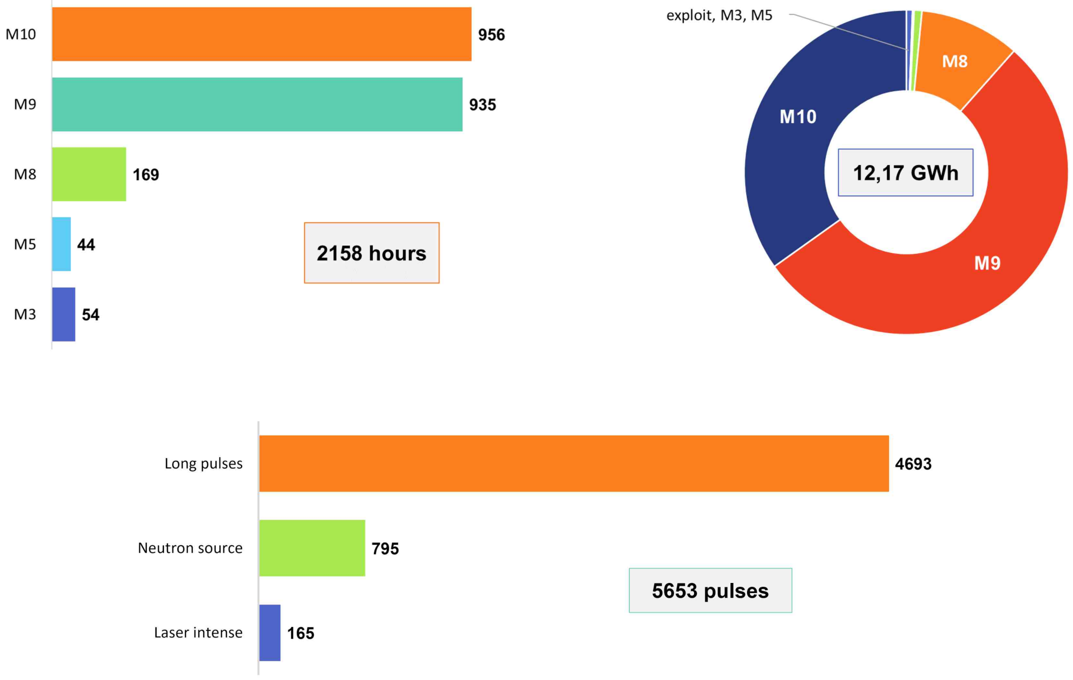

FIG. 6. *Distribution of the number of magnetic field shots at pulsed facility and magnet hours and power used at the DC field facility in* 2025.

The top panel of figure 6 shows the magnet time and power used at the DC field facility. In total, the facility has provided 2158 hours of magnet time, mostly used on the 24 MW magnet sites (left) with a total power consumption of 12.17 GWh (right). 169 hours of magnet time were used on the M8 magnet site, which is the new 42 T hybrid magnet, for technical commissioning and first scientific experiments aiming to validate the use of this magnet for different scientific needs and experimental set-ups. This work will continue in 2026.

The bottom panel of figure 6 shows the distribution of the number of shots, depending on the power supply used, performed at the Toulouse pulsed field facility or using the mobile capacitor bank in combination with the neutron source at the ILL, intense laser sources at LULI and the Lawrence Livermore National Laboratory. The long pulse field facility in Toulouse has provided 4693 shots at high field on a total of 5653 shots and 960 shots using the mobile capacitor bank in combination with neutrons or intense laser sources.

CONCLUSION

The technical and scientific environment of LNCMI, adapted to research in high magnetic fields, is highly appreciated by the international scientific community. A large majority of users shows great interest in the laboratory and they come regularly in order to perform their experiments, thereby strengthening collaborations between research groups. The number of projects submitted and performed at the LNCMI demonstrates the international scope of the laboratory. As the schedule of the Grenoble 24 MW magnets is extremely tight and the electricity costs high, it is essential to optimize the use of these magnets. Experiments may also be transferred from one facility to the other, after discussion with the scientists, if the schedule is too tight, or in case another facility has a better adapted set-up for an experiment.

C. Warth-Martin, N. Bruyant, M. Druart, A. Gasparini, S. Buisson, C. Grandclément

Outreach activities

LNCMI-Grenoble: One off interventions

In 2025 we organized about 15 group visits for both school children and members of the general public (figure 7). We focus here on some of them:

- On the 12th of March we welcomed a group of Student from the Lycée Roland Garros (Ile de La Reunion) for a visit to LNCMI. The lively visit of the high magnetic field facility of the 18 students was combined with a visit of the ESRF.
- A "coupled" visit was also organized during the General Assembly of the FLEXRICAN project on the 10th of April), permitting the administrative and technical staff engaged in this European project to acquire an overview of the projects linked to energy management and decarbonation developed in the two facilities.
- On the 19th of September a special visit of the new 60 MVA transformer was organized permitting the administrative staff involved in this large project to gain insight into the real object!

LNCMI-Grenoble: Recurrent and other events

- On Saturday the 11th of October, the "fête de la Science" was an opportunity to organize complete tours of the installation for a wide range of public of every age.

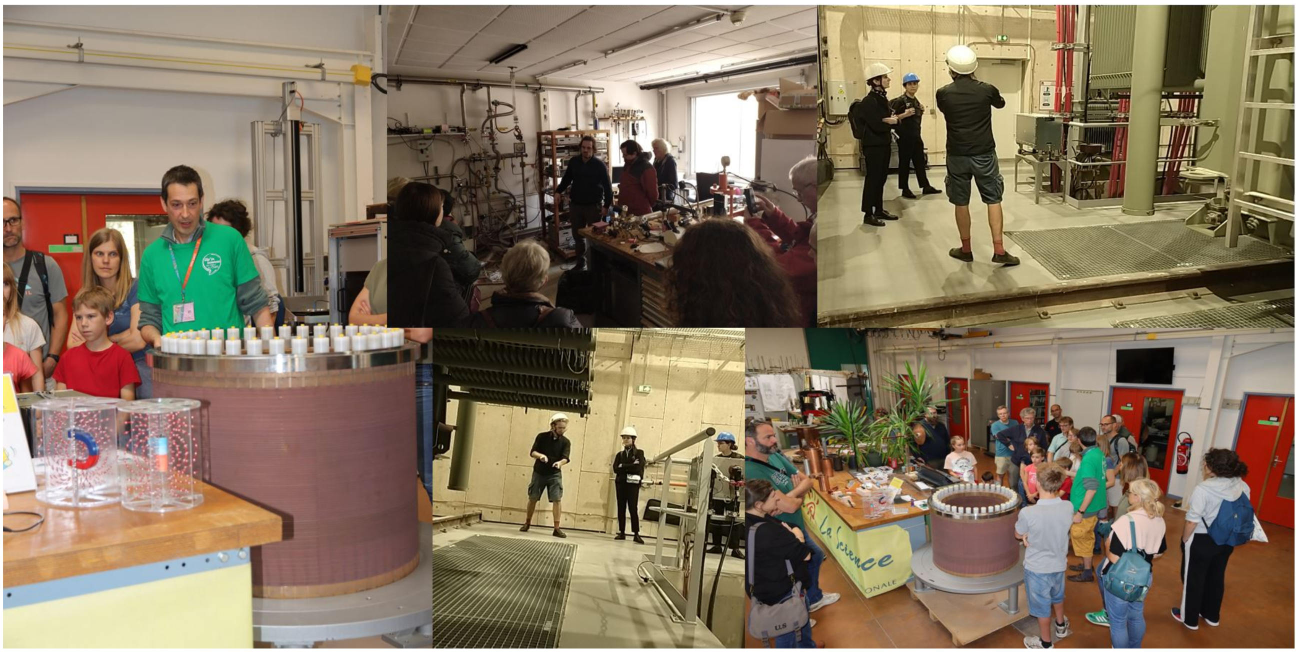

FIG. 7. *Visitors at the LNCMI-G during some of the group visits organized during 2025.*

LNCMI-Toulouse: One off interventions

- Animation/demonstration on electromagnetism for elementary school "Petit Collège du Caousou" (30 pupils).
- Two visits were organized during the year for "Ô-Talents - Egalité des chances" program which aims to combat social, cultural, territorial and gender barriers (30 students from high school level).
- Participation in the Quantum images project led by "La physique autrement".

LNCMI-Toulouse: Recurrent and other events

For many years, the scientific and technical staffs have been fully involved in and actively contributing to the Science Festival (October 2025). On Friday, we hosted two classes from a high school and a middle school

FIG. 8. *A large number of visitors at LNCMI-T on the occasion of "fête de la science".*

(figure 8). The open day for the general public on Saturday was also a success, with nearly 100 visitors coming to explore the laboratory facilities and the various demonstration booths (phase transitions, superconductivity, magnetism...) we presented.

E. Beaugnon, F. Debray, A. Demuer, C. Faugeras, O. Jay, S. Krämer, R. Raison, J. Sarrade, L.Ronayette, G. Seyfarth, B. Vincent, S. Badoux, M. Barragan, J. Béard, J. Billette, N. Bruyant, C. Duffy, N. Ferreira, F. Lecouturier-Dupouy, M. Leroux, E. Noël, M. Pierre, S. Tardieu, D. Vignolles, A. Zitouni

Emerging Layered Materials

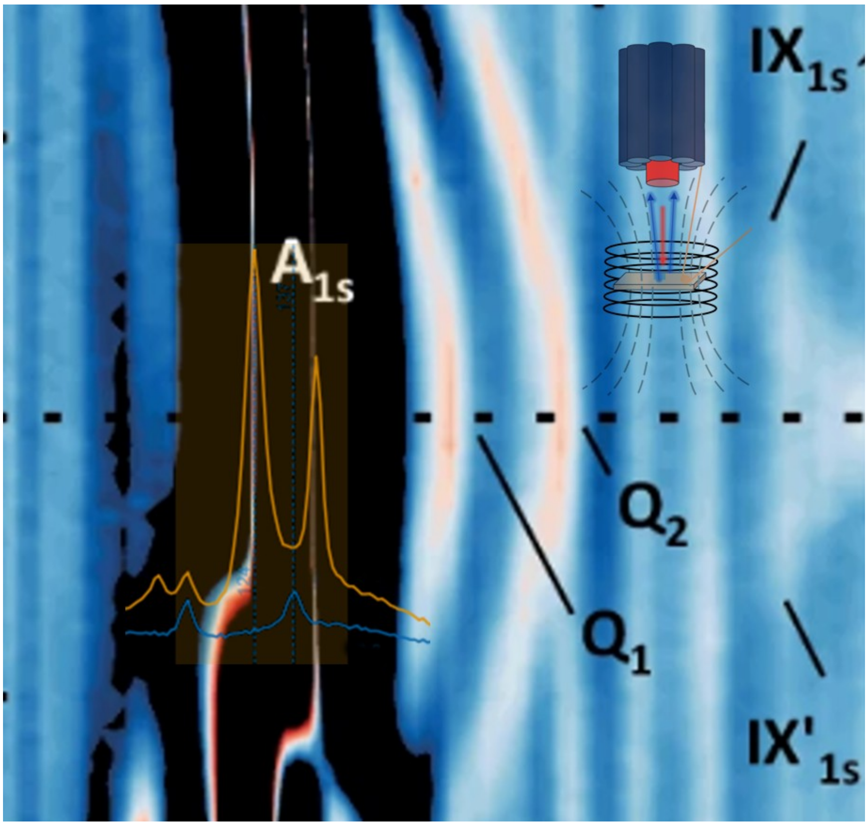

Magnetic-field-induced break of the in-plane isotropy in graphite above the quantum limit

Graphite is an allotrope of carbon, composed by a Bernal stacking of graphene layers. In this material, the interlayer coupling is made by van-der-Waals forces, which results in highly anisotropic electronic properties.

Perhaps one of the most curious properties of graphite regards its resistance in the presence of strong magnetic fields. It is conventionally observed that, in low temperatures, the resistance of the material increases almost-linearly with magnetic fields, reaching a maximum for magnetic fields around 15 T. Above this field, a region of negative magnetoresistance is observed, before the emergence of a high resistance state is triggered by magnetic fields between 35 T and 55 T.

The triggering of the high-resistance state is proposed as a c-axis electronic instability in the material [Nakamura *et al.*, J. Phys. Soc. Jap. **52**, 2875 (1983)], associated with a 3D to 1D dimensional crossover when the degeneracy of the lowest Landau subbands is adequately lifted. In this context, no in-plane anisotropy should manifest as a consequence of the high resistance state, as this would be an exclusively out-of-plane phenomenon.

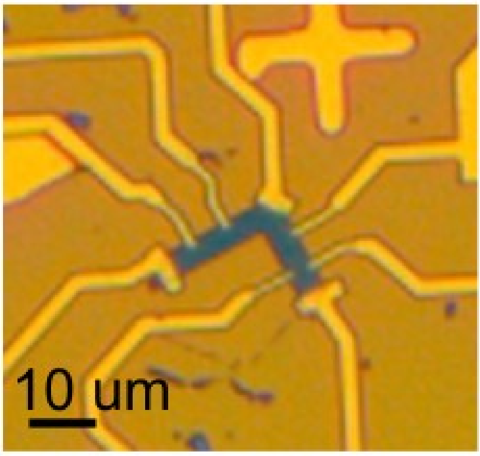

FIG. 9. *Electrically-contacted L-shaped graphite nanostructure.*

However, as graphite is not a single crystal, attempts to probe such an (an)isotropy invariably run into the issue of bulk graphite not possessing well-defined in-plane crystallographic axes. In this work, we address this issue by probing the in-plane isotropy of microscopic flakes extracted using the conventional exfoliation method from bulk graphite crystals grown by diffusion through single-crystalline Ni foils. Graphite obtained with this technique has been shown to present long-range crystalline order, permitting the measurement of electrical transport properties along its in-plane zig-zag and arm-chair directions.

By studying L-shaped microstructures in exfoliated devices, we demonstrate the emergence of an in-plane resistivity anisotropy for measurements along and perpendicular graphite's a-axis. Results in different graphite samples suggest that the effect manifests above 20 T, and is suppressed by the increase of sample temperature, indicating a surprising planar ordering during the out-of-plane, magnetic-field-induced electronic transition in the material.

Such results constitute the first experimental observation of a magnetic-field-induced electronic state with broken in-plane symmetry in graphite in the quantum regime. These results provide an unambiguous demonstration of the in-plane nature of the high resistance state. It challenges the current understanding of the high resistance state in graphite.

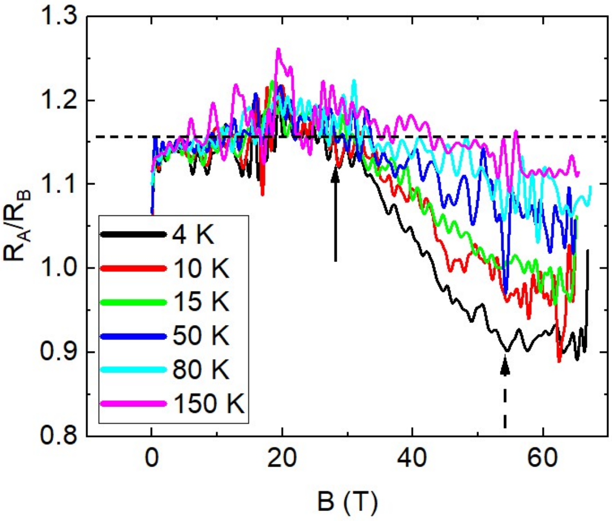

FIG. 10. *Magnetic field dependence up to 70 T of the ratio between the resistance of the two perpendicular branches of an L-shaped graphite nanostructure. The plain-line arrow shows the deviation from isotropy. The dashed arrow highlights the anisotropy in the high resistance state.*

M. Pierre, L. Veyrat, M. Leroux, M. Goiran, W. Escoffier
E. Sa, B. Camargo (University of Warsaw)

Quadrupolar excitons in $MoSe_2$ bilayers

Two-dimensional (2D) layered semiconductors, particularly transition metal dichalcogenides (TMDs), provide an excellent platform for studying exciton physics due to strong Coulomb interactions, reduced dielectric screening, and valley-selective properties in the monolayer limit. The development of van der Waals heterostructures has further expanded this field by enabling lattice-mismatch-free stacking and precise control of material composition and orientation. In such systems, long-lived interlayer excitons (IXs), with electrons and holes residing in different layers, can be efficiently tuned by external electric fields and exhibit strong dipolar interactions. Recently, even more complex quasiparticles-quadrupolar excitons-have been proposed, arising from the hybridization of two dipolar excitons with opposite dipole moments. These states exhibit higher-order, non-local interactions that enable access to novel many-body phenomena beyond monopolar and dipolar regimes.

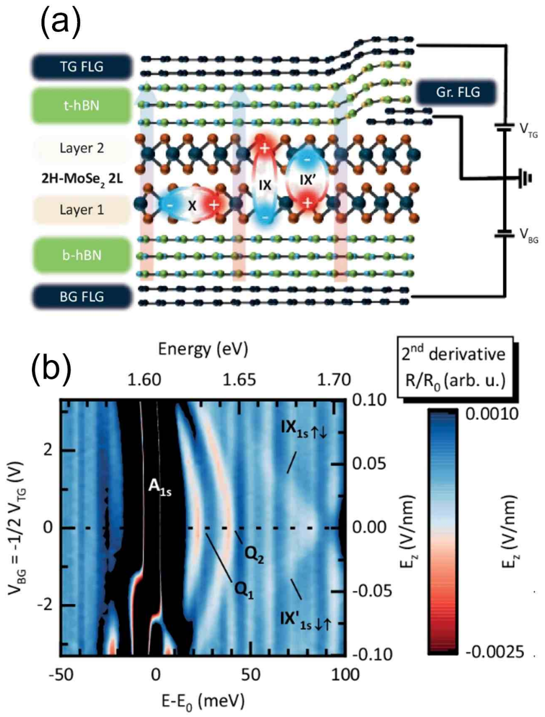

FIG. 11. *(a) Schematic of the device. 2H-stacked natural bilayer of MoSe2 encapsulated by insulating bottom and top hBN layers. (b) False-color map of the 2nd derivative of reflectivity as a function of the gate voltages (left axis) and the corresponding E_z (right axis).*

Here, we demonstrate the formation of quadrupolar excitons in a natural 2H-stacked $MoSe_2$ homobilayer. Using a double-gated device and electric-field-dependent reflectivity measurements (figure 11(a-b)) we identify dipolar and quadrupolar interlayer transitions and their complex interaction with intralayer excitonic species. Our results establish natural $MoSe_2$ bilayers as a robust platform for tunable multipolar exciton physics.
The false-colour map (figure11 reveals distinct excitonic features and their mutual interactions. The states labelled $IX_{1s,\uparrow\downarrow}$ exhibit a linear Stark shift, consistent with their dipolar interlayer character. By matching the experimental shift with model simulations, we extract a dipole moment of $d \simeq 0.55e\,\mathrm{nm}$, in agreement with reported values for $MoSe_2$ bilayers. In contrast, the states labelled Q1 and Q2 show a pronounced quadratic Stark shift at low electric fields, providing clear evidence of their quadrupolar nature. These states originate from the coupling of anti-aligned dipolar excitons and possess a vanishing dipole moment at zero field. With increasing electric field, charge displacement induces a finite dipole moment, resulting in a nonlinear Stark response and a gradual crossover toward dipolar behavior.

Extended reflectivity measurements (not shown here) reveal pronounced anti-crossings between the A_{1s} exciton and multiple interlayer states, including dipolar and quadrupolar excitons, at high electric fields. This behaviour is well reproduced by simulations that incorporate electron tunnelling, demonstrating its essential role despite being nominally symmetry-forbidden in natural homobilayers. While hole tunnelling primarily drives hybridisation between intra- and interlayer excitons, electron tunnelling governs the observed anti-crossings and electric-field-induced changes in exciton character. These tunnelling-mediated interactions are crucial for an accurate description of the excitonic energy landscape in $MoSe_2$ bilayers.

In summary, we have explored the evolution of the excitonic energy landscape in natural $MoSe_2$ homobilayers under an external electric field. For the first time, we report the observation of quadrupolar exciton states in a natural $MoSe_2$ bilayer. These excitonic transitions exhibit a pronounced nonlinear electric-field response and a substantially stronger dipolar exchange interaction compared to previously studied heterotrilayer systems. Our experimental findings are well reproduced by a many-particle effective Hamiltonian model. Within this framework, dipolar excitons are identified as spin-triplet interlayer states, while quadrupolar excitons arise from exchange coupling between interlayer spin-singlet excitons. Furthermore, the model emphasises the crucial role of electron and hole tunnelling in shaping the excitonic spectrum and its evolution under applied electric fields. More details can be found in [Jasiński, *et al.*, Nature Comm. **16**, 1382 (2025)].

J. Jasiński, N. Bruyant, D.K. Maude, P. Plochocka
M. Dyksik, A. Surrente, M. Baranowski (Wroclaw University of Science and Technology), J. Hagel (Chalmers University of Technology, Gothenburg), S. Brem, E. Malic (Philipps-Universität Marburg), E. Wietek, A. Chernikov (Technische Universität Dresden), T. Taniguchi, K. Watanabe (NIMS, Tsukuba)

Excitonic anisotropy in single-crystalline two-dimensional silver phenylchalcogenides

Two-dimensional metal-organic chalcogenides constitute a class of hybrid semiconducting materials composed of metal cations, organic ligands, and chalcogenide anions. In this work, silver phenylchalcogenides (AgEPh, E = S, Se, Te) form a layered, two-dimensional van der Waals framework. Unlike 2D perovskites, these materials are characterised by covalent bonding between the organic and inorganic subunits, which imparts enhanced chemical stability in air and common solvents. Their low crystal symmetry gives rise to pronounced in-plane anisotropy, making them promising platforms for polarisation-sensitive optoelectronic and photonic applications.

A combination of ab initio calculations (DFT and GW-Bethe-Salpeter equation) and polarisation-resolved optical micro-spectroscopy was used to establish a direct link between the low-symmetry crystal structure of these materials and their anisotropic optical response.

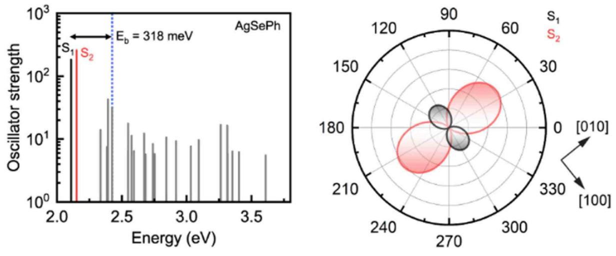

FIG. 12. *Left: Log scale excitation spectrum of AgSePh compound calculated using GW-BSE. Vertical bars represent excitons, blue dotted line represents GW band gap. Right: Calculated absorption intensity of two lowest-energy bright excitons in AgSePh projected onto the ab-plane in real space.*

Density functional theory and GW-Bethe-Salpeter equation calculations reveal that all AgEPh compounds exhibit strongly anisotropic in-plane electronic band structures, particularly in the valence band. These anisotropies lead to the formation of multiple bright, Wannier-like excitons confined within the inorganic Ag-E layers, with high binding energies ($\simeq 300-480$ meV, depending on composition) and well-defined polarisation directions (figure 12, shown on the example of AgSePh). Room-temperature (RT) polarisation-resolved absorption and photoluminescence measurements confirm these predictions and reveal distinct material-dependent behaviour. However, some observations at RT differ from the theoretical predictions. For example, in AgSePh the two lowest-energy excitonic features, X_1 and X_2, are polarised along the [010] and [100] crystal axes, respectively, in contrast to GW-BSE calculations. Polarisation-resolved measurements were then performed at low temperature (T=4 K), in order to exclude the effects related to the lattice vibrations and thermal broadening of spectral features, which were not included in the theoretical model.
At 4 K, reflectance spectra of AgSePh reveal a clear splitting of the lowest excitonic feature X_1 into two closely spaced resonances (X_{1X} and X_{1Y}, figure 13, left). Polarisation-resolved analysis demonstrates that these two states possess well-defined orthogonal in-plane polarisations. Importantly, their energy ordering, relative oscillator strengths, and polarisation directions (figure 13, right) are consistent with the two lowest bright excitons (S1 and S2, figure 12) predicted by GW-BSE calculations. These results show that the room-temperature X_1 feature is composed of multiple unresolved excitonic states and directly reconcile experimental observations with theoretical predictions.

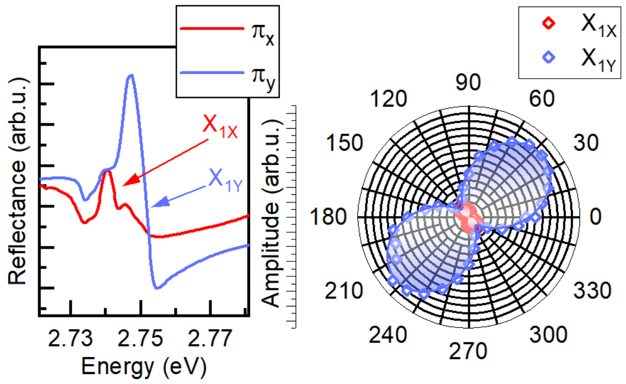

FIG. 13. *Left: Polarisation-resolved reflectance spectra measured from AgSePh single crystal in two orthogonal polarisations, oriented along two characteristic crystallographic axes of the crystal: [100] (red) and [010] (blue), revealing the substructure of X_1 excitonic feature, labelled X_{1X} and X_{1Y}. Right: Amplitude of two features X_{1X} and X_{1Y} obtained from fitting the reflectance spectra with sum of two Lorentz resonances. Solid line is the $\cos^2\theta$ fit to the data. T=4 K.*

Overall, the work provides a comprehensive experimental and theoretical description of in-plane excitonic anisotropy in 2D silver phenylchalcogenides, clarifying how structural anisotropy, chemical composition, and thickness govern their optical properties. These results establish AgEPh materials as a promising platform for anisotropic optoelectronic and photonic applications. For more details please see [Lee *et al.*, Advanced Optical Materials **13**, e02435 (2025)].

K. Posmyk, P. Peksa, P. Plochocka
M. Dyksik, M. Baranowski (Wroclaw University of Science and Technology), W.S. Lee, Y. Cho, N. Samulewicz, H.J. Kulik, W. A. Tisdale (Massachusetts Institute of Technology, Cambridge, Massachusetts)

Magneto-optical response of Frenkel and Wannier excitons in CrSBr

Chromium Sulfur Bromide (CrSBr) is a layered A-type antiferromagnet (AFM) which optical response exhibits two prominent excitonic resonances, X_A and X_B, located at 1.38 eV and 1.8 eV, respectively. By means of magneto-optical spectroscopy in low (DC) and high magnetic field (up to 90 T) combined with QS$G\hat{W}$ calculations, we show that these two excitons have distinct microscopic origins; X_A exhibits a strongly localised Frenkel-like character, while X_B is a delocalised Wannier-Mott-like state spanning over several chromium atomic sites.

The transition to the ferromagnetic (FM) phase in external magnetic field causes a dramatic difference in exciton behaviour; X_B shifts by 100 meV, an order of magnitude more than X_A (10 meV) (figure 14(a-b)). The Wannier-Mott-like X_B closely tracks the reduction of the fundamental band gap between AFM and FM states (110 meV), whereas the strongly bound X_A exciton does not depend on it as much. This is further backed up by the calculations of oscillator strength of excitons in both magnetic phases. High-field measurements allow us to access the diamagnetic coefficients σ of both excitons (figure 14(c)), which are related to the in plane exciton radius as $\sigma = \frac{e^2}{8\mu}\langle r^2\rangle$. X_B has $\sigma = 0.22\,\mathrm{meV/T^2}$, more than four times the value of X_A ($\sigma = 0.05\,\mathrm{meV/T^2}$), demonstrating its larger spatial extent.

QS$G\hat{W}$ wavefunction isosurfaces confirm that X_B extends to 4.5 nm in-plane and spreads into neighbouring layers when the spin confinement is lifted in FM phase, while X_A is confined to 1.2 nm, with reduced interlayer delocalisation (figure 14(d-g)). The in plane size ratio of X_A to X_B is 3.75, aligning well with the high field data.

Temperature-dependent measurements ($2-130\,\mathrm{K}$) further demonstrate that the AFM-FM redshift of X_B decreases from 110 meV to 85 meV with increasing temperature, whereas X_A remains nearly unchanged. Frozen-phonon QS$G\hat{W}$ calculations identify out of plane A_g phonon modes as the dominant source of the temperature dependent renormalisation of X_B's energy, while X_A shows negligible exciton-phonon coupling in both AFM and FM phases.

CrSBr hosts two excitonic species with contrasting real-space character and sensitivity to band gap changes and lattice perturbations. Their coexistence places CrSBr in an intermediate regime not captured by conventional ligand-field or Rydberg models, challenging the standard dichotomy of Wannier-Mott and Frenkel excitons. For more information, please see [Smiertka *et al.*, arXiv:2506.16426 [2025]].

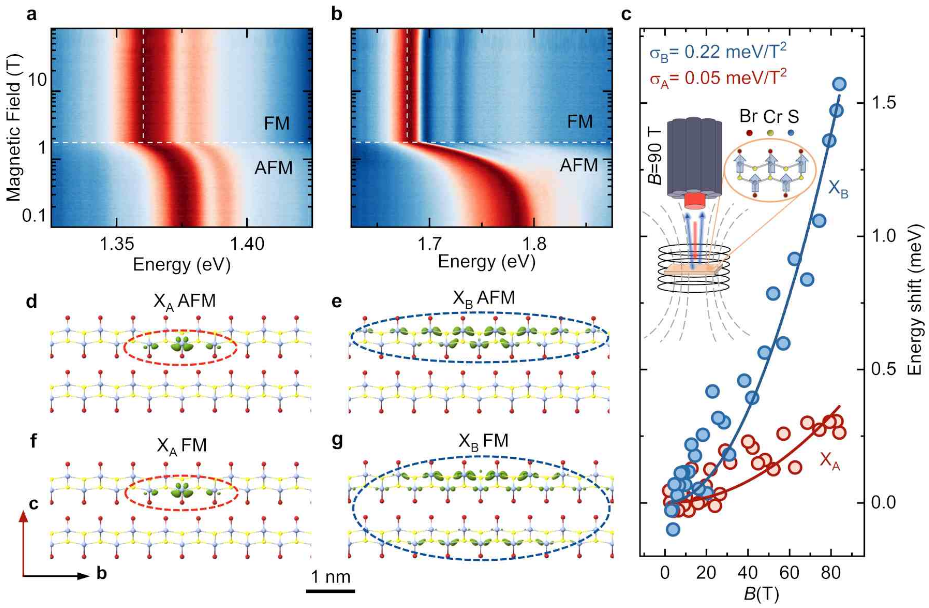

FIG. 14. *(a-b) False color plots of reflectivity spectra in magnetic field up to 90 T, on a log scale, for both excitons (c) Diamagnetic shifts of X_A and X_B measured in 4K. (d-e) Wave-function isosurface simulations for excitons in AFM phase and (f-g) FM phase.*

M. Śmiertka, M. Rygala, K. Posmyk, P. Peksa, P. Plochocka
M. Dyksik, M. Baranowski (Wroclaw University of Science and Technology), S. Acharya, M. van Schilfgaarde, (National Renewable Energy Laboratory, Golden), D. Pashov (King's Collage London), F. Dirnberger (Technical University of Munich, Garching), K. Mosina, Z. Sofer (University of Chemistry and Technology Prague)

Excitons in the magnetic 2D semiconductor alloy CrSBr$_{1-x}$Cl$_x$

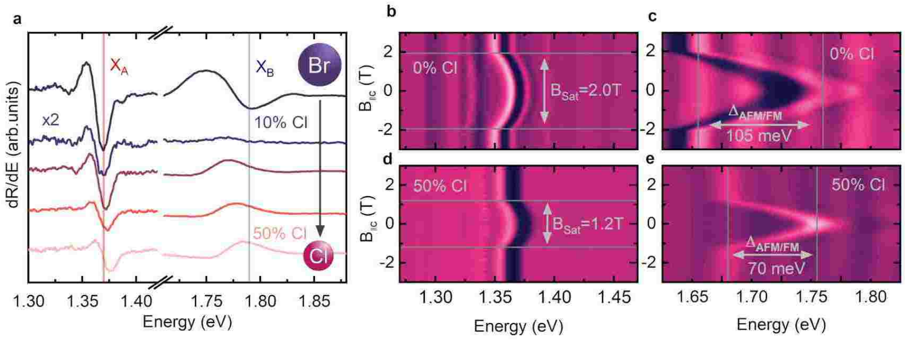

FIG. 15. *(a) Derivative reflectance spectra of CrSBr$_{1-x}$Cl$_x$ flakes showing the evolution and blue-shift of X_A and X_B with increasing Cl content. (b-e) Derivative reflectance spectra in DC field $B \parallel c$, for $x = 0$ and $x = 0.5$ samples. Arrows and lines indicate the different critical field B_{sat} and $\Delta_{AFM/FM}$ for X_A and X_B, respectively.*

Chromium sulfide bromide (CrSBr) is a layered A-type antiferromagnet. In it's optical response there are two prominent excitonic states, $\mathrm{X_A}$ and $\mathrm{X_B}$ at 1.38 eV and 1.8 eV, respectively. In pristine crystals these states have distinct microscopic character; $\mathrm{X_A}$ is strongly localized and Frenkel-like, while $\mathrm{X_B}$ is a delocalized Wannier-Mott-like exciton extending over several Cr sites and more strongly coupled to band structure, magnetic order and lattice vibrations than $\mathrm{X_A}$. This results, for instance in an order of magnitude larger redshift ($\Delta_{\mathrm{AFM/FM}}$) of $\mathrm{X_B}$ state compared to the $\mathrm{X_A}$ upon antiferromagnetic (AFM) to ferromagnetic (FM) transition [Smiertka *et al.*, arXiv:2506.16426 [2025]].

Here, we investigate how this excitonic landscape is affected by Br substitution with Cl forming CrSBr$_{1-x}$Cl$_x$ alloys. Chlorine incorporation reduces the lattice constants and increases the band gap, leading to a systematic blueshift of both excitonic resonances (figure 15(a)). The delocalised $\mathrm{X_B}$ follows the band gap evolution with increasing Cl content more closely and blue-shifts by 30 meV, while $\mathrm{X_A}$ shifts by only 10 meV. Crucially, the excitonic transition observed in CrSBr$_{1-x}$Cl$_x$ preserves coupling to magnetic order as in the case of pure CrSBr, as shown in figure 15(b-c). However, the strength of this coupling scales differently with Cl content for the two excitonic states.

This can be clearly seen from the $\Delta_{\mathrm{AFM/FM}}$ values extracted for each sample (figure 16(a)). The magnetic order dependent energy difference of $\mathrm{X_B}$ is strongly suppressed by alloying (by 40 meV), while that of $\mathrm{X_A}$ remains nearly unchanged. This shows that chlorine progressively reduces the magnetic sensitivity of the Wannier-Mott-like exciton and drives it toward a more Frenkel-like regime. To confirm this hypothesis, we performed high field magneto-reflectance up to 90 T which provides complementary information on the in-plane spatial extent of the excitons. From the quadratic diamagnetic shift we extract diamagnetic coefficients σ which are directly linked with the exciton radiuses via $\sigma = \frac{e^2}{8\mu}\langle r^2\rangle$. With increasing Cl content, the diamagnetic coefficient of $\mathrm{X_B}$ decreases, by about 30% at $x = 0.5$, while $\mathrm{X_A}$ is almost unaffected. This suggests that unlike $\mathrm{X_B}$, the spatial character of $\mathrm{X_A}$ is not changed significantly.

Ligand substitution also tunes the saturation field $\mathrm{B_{sat}}$ which is associated with a characteristic kink in the energy versus B curves. It decreases monotonically (figure 16(c)) with increasing Cl content, indicating weakened interlayer exchange and magnetic anisotropy.

The simultaneous decrease of the AFM-FM shift of $\mathrm{X_B}$, it's radius, and saturation field demonstrates that halogen alloying is not only an efficient way to engineer basic magnetic properties like critical fields and the magneto-excitonic coupling, but also allows to scale the excitonic character between the two standard regimes of Wannier-Mott and Frenkel excitons in magnetic materials.

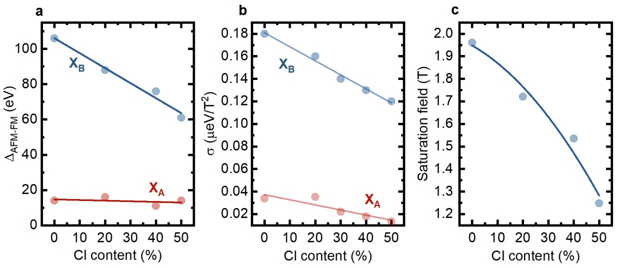

FIG. 16. *(a) AFM-FM splitting for X_A and X_B as a function of Cl concentration. (b) Diamagnetic coefficients σ of X_A and X_B. (c) Magnetic saturation field versus Cl content.*

M. Śmiertka, M. Rygala, P. Plochocka
O. Janikowska, A. Surrente, M. Baranowski (Wroclaw University of Science and Technology), K. Mosina, Z. Sofer (University of Chemistry and Technology, Prague)

Laser patterning of the room temperature van der Waals ferromagnet 1T $CrTe_2$

The discovery of antiferromagnetic and ferromagnetic phases in two-dimensional (2D) crystals had considerable echo recently, setting large communities on track to revisit low-dimensional magnetic ordering and spintronic phenomena. Magnetic 2D materials give access to a wealth of fascinating properties, such as optimum electric-field control of magnetism, multifunctionalities, moiré effects, and flexible membrane-like architectures. In that context, 2D materials exhibiting above-room-temperature magnetism are of particular interest. However, such 2D compounds are rare and only very few bulk van der Waals materials, from which 2D flakes may be exfoliated, have a Curie temperature $T_c > 300\,\mathrm{K}$.

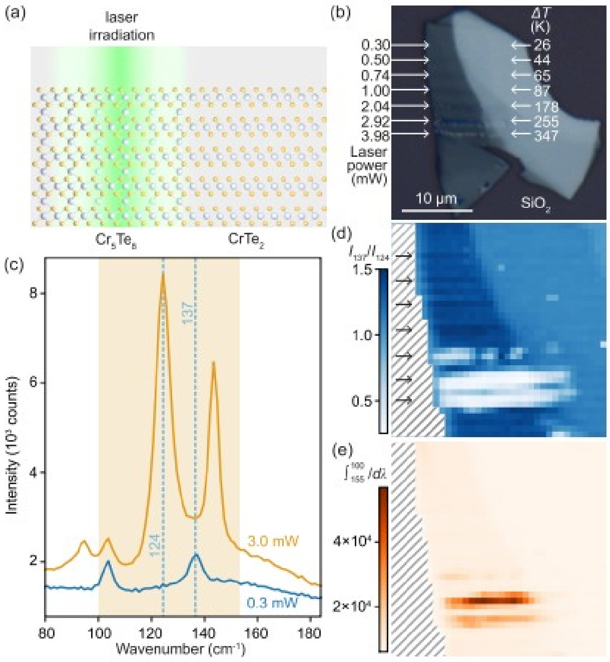

FIG. 17. *Direct laser patterning of 1T $CrTe_2$. a) Crosssection of the atomic structure representing the laser-induced transformation of 1T $CrTe_2$ into a Cr self-intercalated Cr/Te compound. b) Optical image of a flake on SiO_2/Si, laser-irradiated along line scans of increasing power. The laser induced increases of temperature 1T are indicated. The flake has regions of different thicknesses; here we specifically consider the thinner region of darkest optical contrast, whose thickness is $\simeq$ 20 nm. c) Representative Raman spectra measured with a low (0.3 mW) and a high (3.0 mW) laser power. d-e) Hyperspectral Raman mapping (0.3 mW laser power for acquisition): d) Ratio of the intensity averaged around 137 cm^{-1} and 124 cm^{-1} (transformed 1T CrTe2 appears with deep hue of blue); (e) Area under the spectra between 100 cm^{-1} and 155 cm^{-1} (unaltered 1T $CrTe_2$ appears with deep hue of orange)*

So far, van der Waals heterostructures essentially consist of vertical junctions of thin (or even purely 2D) materials. Their functionality relies on an ultimately sharp interface between the layers, which are separated by a van der Waals gap. Additionally, or alternatively, in plane structuration can be introduced to pattern lateral junctions. Such lateral junctions offer further degrees of freedom for micro/nanostructuration and are suited for implementing or detecting various spin dependent effects or functions, such as giant magnetoresistance, large spin accumulation, long distance spin transport, or nonlocal measurements of (inverse) spin Hall effect. Lateral patterning can be achieved during the synthesis by tuning growth conditions, as recently shown with Cr/Te compounds. Planar modulation of the electronic properties was demonstrated accordingly. Rather than a bottom up approach, a top down strategy is also possible but requires to locally transform the material, with the help of a structural phase engineering under a focused laser beam. This strategy already allowed patterning ohmic junctions in a transition metal dichalcogenide, but was not used yet in the prospect of magnetic lateral junctions with van der Waals materials.

Here, we implement this laser patterning approach using thin flakes of the room temperature ferromagnet 1T $CrTe_2$, see figure 17. Under certain conditions, this material readily transforms into other Cr/Te compounds that are self intercalated with Cr and whose T_c falls below 300 K. This tendency to polymorphism explains why chemical vapor deposition of Cr/Te flakes can naturally produce (magnetic) Cr_2Te_3/Cr_5Te_8 lateral junctions, and the reason why moderate heating of 1T $CrTe_2$ transforms it into other Cr/Te compounds (especially, Cr_5Te_8). Using specific peaks in Raman scattering spectra as a thermometer and focused Kerr magnetometry, we show that: i) laser induced thermal transformation of 1T $CrTe_2$ can be controlled using an appropriate substrate; ii) patterns can be laser-imprinted within a ferromagnetic matrix, with a spatial resolution set by the optical beam, or with a potentially better resolution. We finally find that iii) full hBN encapsulation, usually prescribed to limit the physico-chemical interaction of 2D materials with airborne species, is also valuable to protect ultra thin flakes, which are particularly susceptible to laser-induced heating already at low laser powers, and thereby demonstrate room temperature ferromagnetism for a 1T $CrTe_2$ thickness below 7 nm.

More details concerning this work can be found in [Riccardi *et al.*, Phys. Rev. Mat. **9**, 024001 (2025)].

T. Riccardi, A. Pawbake, C. Faugeras
S. Sarkar, A. Purbawati, A. Arrighi, M. Kostka, A. Hadj-Azzem, J. Vogel, J. Renard, L. Marty, M. Nunez-Regueiro, N. Rougemaille, N. Bendiab, J. Coraux (Institut Néel, CNRS, Grenoble), A. Finco, V. Jacques (L2C, University of Montpellier), L. Ren, X. Marie, C. Robert (LPCNO, INSA, Toulouse), K. Watanabe, T. Taniguch (NIMS, Tsukuba)

Resonant X-ray spectroscopy of CrSBr: Probing the electronic structure through chromium d-d excitations

In the ever-evolving landscape of materials science, the discovery and exploration of novel phases hold immense promise for technological advancements. Among the various kinds of materials with potential applications, van der Waals (vdW) compounds are extremely promising due to their high tunability, both in terms of structure and characteristics. In particular, the emerging field of vdW magnets offers unique opportunities to create novel devices and to advance our understanding of two-dimensional (2D) magnetism.

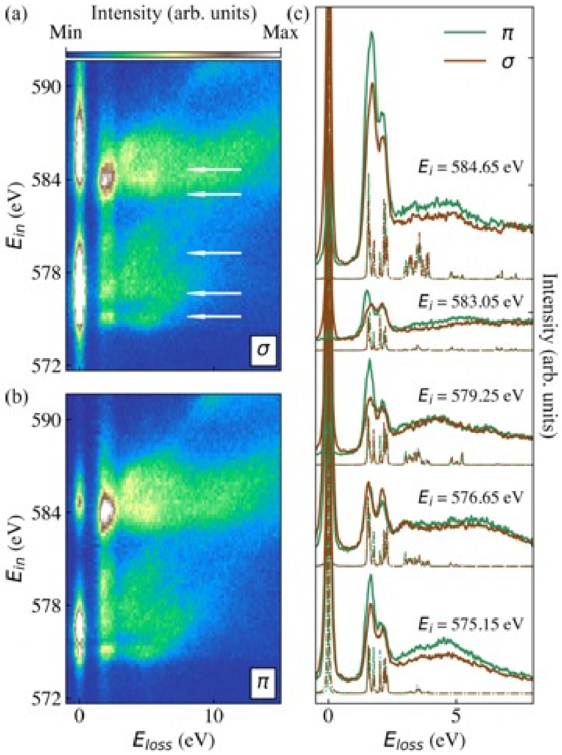

FIG. 18. *RIXS maps measured at 150 K using linear a) σ and b) π incident polarizations. The white arrows in panel a) point to the incident energies used for the high-statistics spectra of panels c). c) RIXS spectra measured in both linear polarizations (σ in brown and π in green) collected at 25 K with incident energies as indicated in panel a). The curves are shifted upward with increasing incident energies for better visualization. These measurements were performed at a momentum transfer $k = (0, 0.152, 0.367)$. Dashed lines represent the corresponding simulated spectra generated with the CEF model, assuming no broadening.*

In this context, Cr-based vdW magnets have emerged as particularly promising in the fields of magnetism, optoelectronics, and spintronics, exhibiting properties such as magneto-optical effects and giant tunneling magnetoresistance.

Among them, CrSBr is an air stable semiconducting vdW material hosting optically active excitonic excitations at the origin of intriguing photoluminescent properties. Below its Néel temperature (132 K), the system stabilizes an A-type antiferromagnetic structure, which can be ferromagnetically polarized by applying a moderate magnetic field. Of topical interest is the observed coupling of the photoluminescence with the underlying magnetic structure in CrSBr. Upon transiting from an antiferromagnet to a ferromagnet, its photoluminescence emissions experience a redshift, an effect that is further tunable by controlling the number of monolayers or under pressure.

This behavior is attributed to a transition becoming spin-allowed in the ferromagnetic state, causing a band splitting at both sides of the band gap and lowering the excitons energy. In the polarized phase, some of the excitons are also able to extend out of plane, while they were essentially constrained to a given monolayer in the antiferromagnetic state. Additionally, the lowest exciton displays a strong optical anisotropy, being visible for incident polarization along the b axis and absent in the a axis, further suggesting its low-dimensional character.

To gain a deeper understanding of the Cr^{3+} electronic states in bulk CrSBr, particularly the crystal electric field (CEF) splitting of its 3d orbitals, we conducted X-ray absorption spectroscopy (XAS), resonant inelastic X-ray scattering (RIXS) and X-ray excited optical luminescence (XEOL) measurements at the Cr $L_{2,3}$ edges, see figure 18. The resonant nature of XAS and RIXS makes them element-specific and highly sensitive to Cr states, providing access to unoccupied states and both occupied and unoccupied states. This integrated approach supports the development of a CEF model based on multiplet calculations and paves the way for future in situ and operando studies of CrSBr-based devices.

More details concerning this work can be found in [Porée *et al.*, Phys. Rev. B **112**, 125103 (2025)].

A. Pawbake, C. Faugeras
V. Porée, A. Zobelli, A. Nicolaou (Synhrotron SOLEIL, Gif-sur-Yvette), J. Regner, Z. Sofer (University of Chemistry and Technology, Prague)

Strong and selective magnon-phonon coupling in the van der Waals antiferromagnet $\mathrm{CoPS_3}$

The interplay between lattice vibrations (phonons) and spin-wave excitations (magnons) in magnetic materials has attracted significant attention due to its fundamental importance and potential applications in fields such as spintronics, magnonics, and quantum information processing. Investigating magnon and phonon excitations and their possible hybridization is particularly compelling in van der Waals (vdW) magnets, especially antiferromagnets.

These materials are of interest not only from a fundamental perspective, particularly in the strictly two-dimensional (2D) limit, but also from an applied standpoint. In magnetically anisotropic vdW antiferromagnets, magnons are gapped excitations (with finite energy at $k = 0$), and these magnon gaps often lie at sufficiently high energies near optical phonon modes.

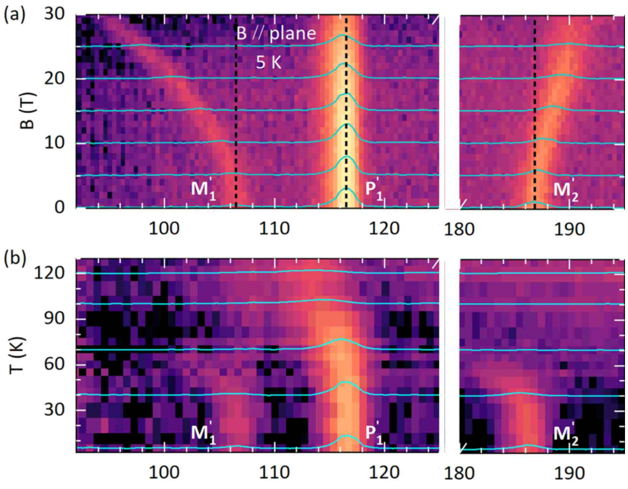

FIG. 19. *False-color map of the Raman scattering response of the $\mathrm{CoPS_3}$ antiferromagnet together with selected characteristic spectra. The coupled magnon-like modes are labeled M_i', while the phonon-like modes are labeled P_i'. (a) Low-temperature (5 K) data collected as a function of the magnetic field B, applied potentially along the in-plane crystal a axis. Vertical dashed lines are drawn at the central energies of the phonon-like features measured at zero magnetic field. Common red or blue B shifts for different pairs of P_i' and M_i' modes point out the repulsion and thus selective coupling of M_1 with P_1 and P_3 but M_2 with P_2'. (b) Evolution of M_i' and P_i' modes with temperature (at $B = 0$ T). Redshifts and softening of M_i' modes underline their magnon-like character.*

Such systems are especially relevant for terahertz technologies, potentially at micro- and nanoscale dimensions. This is particularly the case when these magnons couple to optically active phonon modes, enabling efficient manipulation and detection of spin-lattice dynamics and, possibly, tunability of the modes amplitude and/or frequency. Coupling between $k = 0$ magnon and phonon modes, resulting in the formation of magnon-polarons, was already demonstrated in iron-based vdW antiferromagnets such as $\mathrm{FePS_3}$ and $\mathrm{FePSe_3}$, where magnon and phonon excitations nearly coincide in energy.

Crucially, the identification of this coupling relies on detecting characteristic mode repulsion when effectively tuning the $k = 0$ magnon-like mode via applied magnetic fields. Magnon and phonon modes are also expected to nearly coincide in the cobalt-based vdW antiferromagnet $\mathrm{CoPS_3}$, making it another candidate for exploring magnon-phonon interactions.

Here, we report a Raman scattering study of low energy excitations (in the spectral range of 90-200 cm−1) in the van der Waals antiferromagnet $\mathrm{CoPS_3}$. The measurements were performed as a function of the magnetic field, applied along different crystallographic directions, and as a function of temperature. In addition to the previously reported phonon-like excitations, we identify two additional Raman peaks consistent with zone-center ($k = 0$) magnontype modes. All observed features are interpreted as arising from coupled magnon-phonon excitations. By analyzing their evolution with magnetic field and temperature, we extract characteristic coupling strengths and determine the energies of the uncoupled (bare) magnon and phonon modes. In particular, we find that the coupling involving a nearly degenerate phonon doublet, centered around 157 cm−1, is exceptionally strong and selective: One component of the doublet hybridizes with the lower-energy magnon, while the other couples to the higher-energy magnon. Notably, the phonon doublet, nearly degenerate in the uncoupled case, becomes distinctly split as a result of the hybridization with magnon modes. Based on the extracted bare magnon-gap energies and their magnetic-field evolution, we propose an updated set of exchange interaction and magnetic anisotropy parameters for $\mathrm{CoPS_3}$. Furthermore, our results point to a strongly anisotropic g factor in this van der Waals antiferromagnet.

More details concerning this work can be found in [Jana *et al.*, Phys. Rev. B **112**, 165427 (2025)].

D. Jana, D. Vaclavkova, M. Orlita, C. Faugeras, M. Potemski
R.K. Ulaganathan, R. Shankar (Academia Sinica, Taipei), M.E. Zhitomirsky (University Grenoble Alpes), M. Koperski (National University of Singapore)

Magnetic phases and zone-folded phonons in a frustrated van der Waals magnet

On-lattice frustration, in certain magnetic compounds featuring spin-spin interactions of various kinds between first, second, and neighboring lattice sites, leads to very rich magnetic phase diagrams comprising highly degenerate disordered phases and complex spin orders. Varying the temperature, magnetic field, or hydrostatic pressure, one can navigate through these exotic phase diagrams.

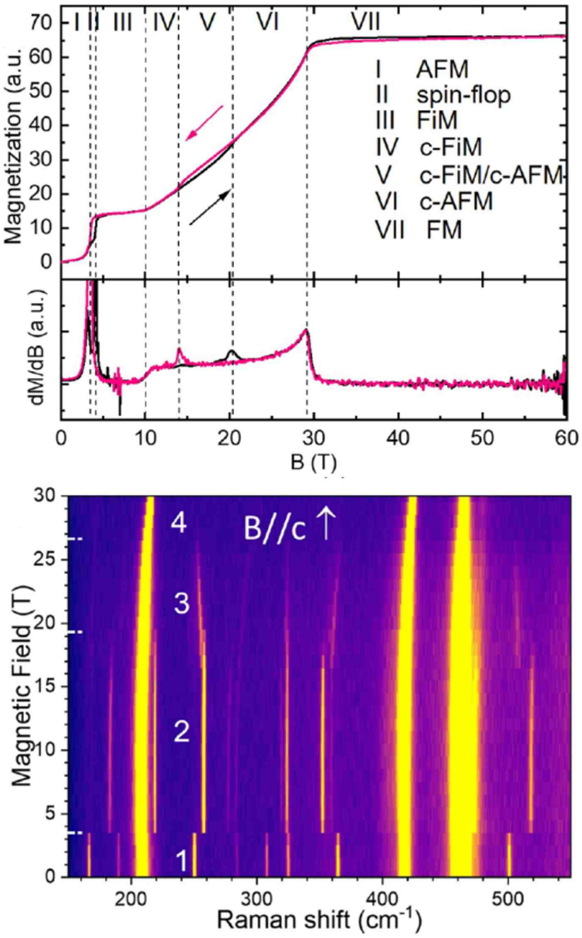

FIG. 20. *Top: Low-temperature (4.5 K) magnetization curve of bulk CrOCl with the magnetic field applied along c axis. Bottom : Magneto-Raman scattering spectra acquired when sweeping the magnetic field along c (c) from 0 to 30 T measured with 1 T field increments. Four different regions can be defined when sweeping the magnetic field up or down, labeled with Arabic and primed Arabic labels, respectively.*

Spectacular examples of emerging exotic quantum phases and cascades of magnetic ground states driven by an external magnetic field or hydrostatic pressure have been reported in the last years. van der Waals magnetic materials are layered materials that can be thinned down to the monolayer limit, while retaining collective magnetic properties, different in nature from those of the bulk parent material.

They altogether offer a broad portfolio of intralayer magnetic ordered states, such as ferromagnetism (FM), Neel-like zigzag, or stripe antiferromagnetism (AFM), combined with ferro- or antiferromagnetic interlayer interactions. Accordingly, they represent a rich platform to revisit and further explore low-dimensional magnetism, with new opportunities as they can be inserted within van der Waals heterostructures to induce specific properties in the neighboring layers via proximity effects; they may even pave the way to an ultimately thin (van der Waals) spintronics.

In this work, we present magneto-Raman scattering and magneto-infrared (IR) absorption spectroscopy analysis of phonon modes in bulk CrOCl, confronted with magnetization versus magnetic field measurements up to high magnetic fields (30 T continuous, 60 T pulsed) and DFT calculations. Our results show that the magnetic frustration in this van der Waals magnet induces magnetic phases with unit cells much larger than the crystallographic one. This additional magnetic periodicity changes both the phonon Raman scattering and the infrared responses by folding the phonon Brillouin zone onto the Γ point.

We observe a series of zone-folded phonons (ZFPs) in the low-temperature AFM phase, see figure 20, which changes under an external magnetic field into another series of ZFP modes in the FiM phase and which persists up to $B = 19\,\mathrm{T}$. Above this magnetic field, the series of ZFP modes transforms again into another series of ZFP similar to that observed at $B = 0$, indicating, at high magnetic fields, the presence of a magnetic phase with the same periodicity as the AFM phase. For $B > 19\,\mathrm{T}$, all Raman-active phonons experience a gradual change of their energies, as large as 1 meV, up to the saturation magnetic field of $B = 30\,\mathrm{T}$. In particular, the ZFP modes allow for spectroscopy of the magnetic ground states and also reflect the magnetic hysteresis as observed when sweeping the magnetic field in opposite directions. DFT calculations allowed to unfold the phonon dispersion and to identify the particular points in the Brillouin zone giving rise to folded mode series.

More details concerning this work can be found in [Pawbake *et al.*, ACS Nano **19**, 23693 (2025)].

A. Pawbake, F. Le Mardelé, T. Riccardi, B.A. Piot, M. Orlita, J. Dzian, C. Faugeras
F. Petot, J. Léveque, B. Grémaud, A. Saul (CINaM, Marseille), M. Hubert, M. Veis (Charles University, Prague), Bing Wu, Z. Sofer (University of Chemistry and Technology, Prague), Y. Skourski (HLD-EMFL, Dresden)

Semiconductors and Nanostructures

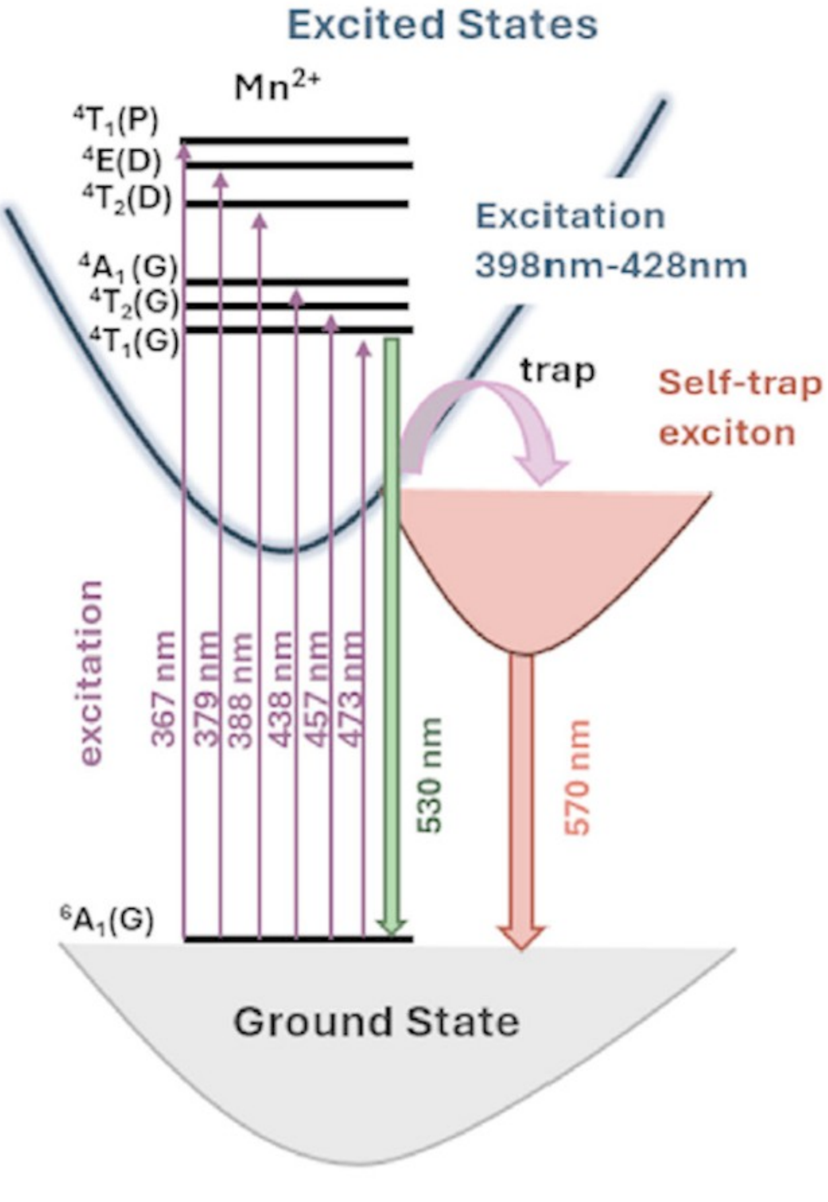

Indirect excitons in the van der Waals semiconductor SnSe

The van der Waals semiconductor SnSe has exceptional thermoelectric properties with a high figure of merit (ZT) of 2.6. SnSe has a camel's back valence band structure, which is commonly regarded as an indicator for high thermoelectric performance. However, its interband excitonic properties are not fully understood. Here, we report near-infrared magneto-transmission spectroscopy measurements on SnSe thin films in pulsed magnetic fields B of up to 60 T. The observed energy shift in the absorption spectrum as a function of magnetic field is well described by a combination of indirect excitonic (hydrogen like) and interband Landau level transitions associated with two closely spaced valence band maxima (VB1 and VB2).

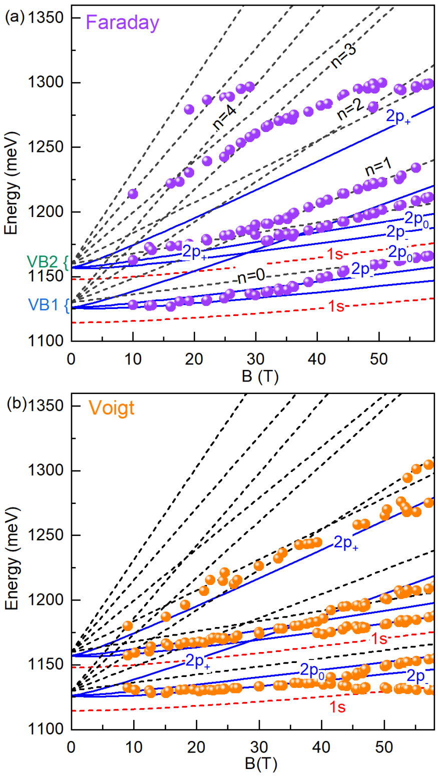

FIG. 21. *Excitonic transition and inter-Landau level transitions versus B at 2 K in Faraday and Voigt geometries. The dashed black lines are the interband transition between Landau levels (n indicates the orbital quantum number of the Landau levels involved), and red and blue lines are the 1s and 2p hydrogen-like transitions, calculated for VB1 and VB2 using the parameters in table I.*

In figure 21 we plot the evolution of the photon energies of the observed spectral features in transmission versus magnetic field. A series of optical transitions are observed with widely different dispersions at these high magnetic fields. We expect to see excitonic (hydrogen-like) transitions at lower energies, and free carrier (Landau level) transitions at higher energies. Given the camel's back structure of the valence band we should observe two series of excitonic features, with an energy separation given by the splitting of the valence band maximum, accompanied by two Landau level fan charts (free carrier transitions) with an identical energy splitting.

The situation is further complicated for SnSe by the optical selection rules due to the parity of the conduction and valence band wave functions. The conduction and valence band extrema of SnSe involve mainly the p-orbitals of Sn and Se. In such a case, due to parity conservation, transitions to the s-like exciton states are dipole-forbidden. This is analogous to the well-known "yellow exciton" series of Cu_2O.

In order to interpret the data, we calculate the magnetic field evolution of the hydrogenic and free carrier transitions. For the hydrogenic transitions we use the numerical results of the variational calculation of Makado and McGill. Neglecting the spin degree of freedom, the 1s state is singly degenerate and the 2p state is threefold degenerate at zero magnetic field, splitting into three distinct branches in magnetic field. The calculated energies of the interband hydrogenic transitions agree well with the observed features in transmission (solid and broken lines in figure 21). The parameters used are summarized in table I.

TABLE I. Summary of parameters used to calculate the magneto-optical transitions of SnSe at 2 K. The reduced exciton masses (μ^*) are calculated using the literature hole masses from ARPES, and the DFT electron mass.

Band	E_g (meV)	$m_h^*(m_e)$	μ^* (m_e)	R_y^* (meV)	a_B (nm)
VB1	1130	0.24	0.093	15.6	6.54
VB2	1160	0.14	0.073	12.2	5.13

Thus we have direct evidence to support the formation of indirect excitons associated with the two valence band maxima of the camel's back structure which are separated by $\simeq 30$ meV. Transitions involving s-states are largely absent due to parity conservation, similar to the case of Cu_2O.

For more details please see [Yang *et al.* Phys. Rev. B **112**, 85203 (2025)].

D.K. Maude
Z. Yang, A. Miyata, Y.Kohama (ISSP, The University of Tokyo), T. Nomura (Shizuoka University), L. Eaves, A. Patanè (University of Nottingham)

Exciton wavefunction anisotropy in lead halide nanoplatelets

The synthesis of colloidal nanocrystals with near-unity photoluminescence (PL) quantum yields has vastly extended the potential of metal halide perovskites for solid-state lighting and display applications. It is possible to template the growth of these nanocrystals to form planar, ultrathin perovskite sheets embedded between long organic molecules, which stabilize the colloids, referred to as nanoplatelets. These colloidal quantum wells are of interest as highly efficient emitters in the blue spectral region.

We investigated the optical properties of perovskite nanoplatelets consisting of two (2ML) or three (3ML) lead halide octahedral slabs and having different edge sizes, ranging from 12 to 53 nm. By drop casting these nanoplatelets at different temperature on a transparent substrate, we could measure the magneto-transmission spectrum up to 70 T of nanoplatelets lying flat or on their edge on the substrate. Typical magneto-transmission spectra of $n = 2$ is shown in figure 22(a), where we notice a shift of the exciton resonance as a function of magnetic field. The Zeeman and diamagnetic contribution to this shift are summarized in figure 22(b).

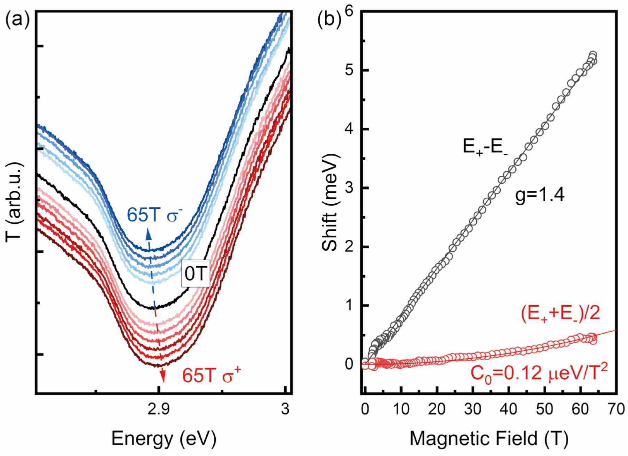

FIG. 22. *(a) Magnetotransmission spectrum of $n = 2$ lead halide pervoskite nanoplatelets measured up to 65 T. (b) Zeeman splitting and diamagnetic shift of the excitonic resonance.*

The overall energy dependence on the lateral size is summarized in figure 23(a-b) for 2 and 3 ML thick nanoplatelets. We notice a consistent decrease of the exciton resonance for larger lateral size and, correspondingly, an increase of the diamagnetic coefficient with increasing edge length, as shown in figure 23(c-d). While the interpretation of these results is still ongoing, at the moment the hypothesis of the influence of quantum confinement in the plane is excluded, given that, especially for 2ML thick nanoplatelets, the trend is observed even for lateral sizes much larger than the effective Bohr radius of the exciton in $CsPbBr_3$-based compounds. Currently, the working hypothesis is related to the influence of the size of the nanoplatelets on the strain accumulation in the lattice, similar to prior observations in colloidal nanocrystals [Zhao *et al.*, ACS Energy Lett. **5**, 238 (2020)]. The renormalization of the band gap would also impact the reduced mass of the exciton, which would in turn change the diamagnetic coefficient, as we observed experimentally. Additional optical and structural characterizations are planned to confirm (or discard) this hypothesis.

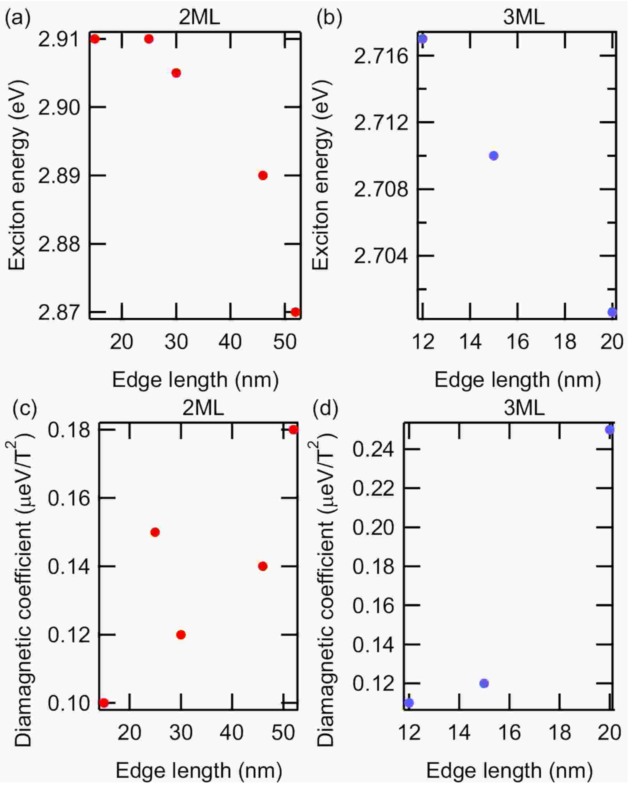

FIG. 23. *Dependence of the exciton energy as a function of the edge length for (a) 2ML (n=2) and (b) 3ML (n=3) thick lead halide perovskite nanoplatelets. Diamagnetic coefficient as a function of the lateral size for (c) 2ML and (d) 3ML thick nanoplatelets.*

P. Peksa, D.K. Maude, P. Plochocka
N. Henke, A. Urban (Ludwig-Maximillan University, Munich), M. Dyksik, M. Baranowski, A. Surrente (Wroclaw University of Science and Technology)

Steric engineering of exciton fine structure in 2D perovskites

The large exciton binding energy in 2D layered perovskites ($E_b > 100\,\text{meV}$) and hence the small effective Bohr radius ($a_B \simeq 1\,\text{nm}$) enhances the exchange interaction between electron and hole spins, which in turn, influences selection rules, radiative pathways, and ultimately emission efficiency. Band-edge excitons in these systems comprise four states; three optically active "bright" states (ψ_X, ψ_Y, ψ_Z) and one optically inactive "dark" state (ψ_D). Owing to the reduced D_{2h}-type symmetry common to layered perovskites, the bright-state degeneracy is lifted, and each bright exciton couples to linearly polarized light along distinct crystallographic directions. Crucially, for practical devices, it is not sufficient to characterize only the easily observed in-plane bright states: knowing the energetic position of both the dark exciton ψ_D and the out-of-plane bright (often "gray") exciton ψ_Z is essential.

To access these "dark" states, we performed magneto-optical measurements in Voigt geometry ($\mathbf{c} \parallel \mathbf{k} \perp \mathbf{B}$). In a finite magnetic field, the zero-field excitons are no longer eigenstates; the in-plane bright states mix with ψ_Z and ψ_D, making them optically active ("brightened") and allowing their energies to be extracted by tracking field-dependent transition shifts. By separately measuring transmission in two linear polarizations—$\mathbf{E} \parallel \mathbf{B}$ (longitudinal) and $\mathbf{E} \perp \mathbf{B}$ (transverse)—we independently resolved two coupled pairs of field-induced states. This polarization-selective approach revealed characteristic signatures such as a longitudinal bright state that blue shifts with field and an emergent, field-activated transition attributable to a brightened dark exciton at higher fields, as well as transverse behavior consistent with brightened ϕ_Z features in suitable phases (see figure 24(a-b).

In [Dyksik *et al.*, Advanced Energy Materials, **15**, 9 (2025)] we present a rich landscape of exciton ordering across compounds, phases, and metal cations. Across investigated materials, the dark state is generally lowest in energy and followed by a bright triplet; however, the ordering within the bright manifold is not universal. For example, in HT $(BA)_2PbI_4$ the out-of-plane ψ_Z state sits highest above the in-plane bright states, while in $(BA)_2SnI_4$ (figure 24(b) the out-of-plane-related state can be pushed below the in-plane bright states—consistent with predictions that structural changes can reorganize the manifold. We also observed that the in-plane states ψ_X and ψ_Y can reverse their order between the HT and LT phases of $(BA)_2PbI_4$, highlighting that octahedral distortions linked to phase transitions can directly reshape the fine structure.

We quantify how the structural parameters influence the bright–dark Δ_{BD} splitting. In general the splitting increases with exciton binding energy E_b (figure 24(c), consistent with reduced exciton size and enhanced exchange interaction. Importantly, we also identified that BA-based compounds in low-temperature phase (strongly distorted motifs) exhibit reduced Δ_{BD}, pointing to lattice corrugation/distortion as a key control knob beyond E_b alone.

To interpret these findings, we employ an effective-mass exchange framework that parameterizes the manifold energies via an exchange energy I and orbital-mixing coefficients a_x, a_y, a_z, with

$$E_X = 2a_x^2 I, \qquad E_Y = 2a_y^2 I, \qquad E_Z = 2a_z^2 I,$$

and $a_x^2 + a_y^2 + a_z^2 = 1$. Such a toy model provides a route to extract the exchange energy from the measured exciton ladders. We further show that I forms distinct trends ("families") depending on distortion/corrugation (figure 24(c), and that increasing lattice distortion reduces the relative exchange energy contribution to the exciton binding energy I/E_b (figure 24(d-e), underscoring the importance of the steric effect controlled by the organic spacer.

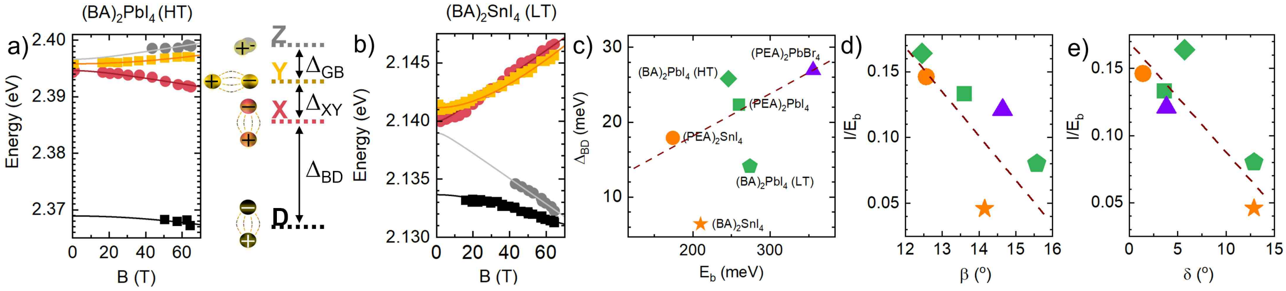

FIG. 24. *Evolution of optical transition energy for dark state and three bright states for (a) HT* $(BA)_2PbI_4$ *(b)* $(BA)_2SnI_4$*. The inset to panels (a) depicts the energy structure of the exciton manifold for a given sample. (c) The bright – dark energy splitting* (Δ_{BD}) *at* $B = 0\,T$ *in function of exciton binding energy* E_b*. (d) The ratio of the exchange energy* I *and exciton binding energy* E_b *in the function of in-plane distortion angle* β *and (e) out-of-plane corrugation angle* δ*.*

P. Plochocka
M. Dyksik, M. Baranowski (Wroclaw University of Science and Technology), Z. Yang (ISSP, University of Tokyo), J. Thompson, E. Malic (Philipps-Universität Marburg)

Tunable room temperature polaritons in the very strong coupling regime in quasi 2D Ruddlesden Popper perovskites

Quasi-two-dimensional layered perovskites exhibit strongly bound excitons and large oscillator strengths, making them excellent candidates for exciton–polariton physics in optical microcavities. When an excitonic transition couples coherently to a cavity photon mode, hybrid light–matter states (upper and lower polariton branches) form, separated by the Rabi splitting Ω_R. A central material parameter for assessing the coupling regime is the exciton binding energy E_b, which sets the characteristic Coulomb energy scale of the electron–hole pair. In the *very strong coupling* (VSC) limit, the light–matter interaction becomes comparable to the excitonic binding energy, such that coupling can begin to modify the excitonic spectrum itself rather than merely mixing a fixed exciton resonance with the cavity mode.

In this work we demonstrate a widely tunable, room-temperature polaritons in an open microcavity containing mechanically exfoliated quasi-2D perovskite crystals of the $n = 3$ phase $(BA)_2(MA)_2Pb_3I_{10}$. A key result is the observation of large splittings (up to $\Omega_R \simeq 155\,\mathrm{meV}$) together with an experimentally determined binding energy $E_b \simeq 100 \pm 10\,\mathrm{meV}$, placing the device at the onset of the VSC regime.

The binding energy is obtained from low-temperature optical spectroscopy by extracting the band-edge energy E_g and the 1s exciton resonance energy E_{1s}, and evaluating $E_b = E_g - E_{1s}$.

The band edge is determined using an Elliott-type fitting of the absorption/reflectivity spectrum (accounting for the excitonic enhancement near the continuum onset and spectral broadening), while E_{1s} is obtained from the excitonic resonance position. For $(BA)_2(MA)_2Pb_3I_{10}$ at cryogenic temperature such procedure yields $E_b = 100 \pm 10\,\mathrm{meV}$.

The determined E_b value is corroborated by high-magnetic-field optical spectroscopy. In the low-field regime, the 1s excitonic resonance is typically a quadratic diamagnetic shift, $\Delta E(B) = c_0 B^2$, where the c_0 coefficient depends on the in-plane spatial extent of the exciton (often expressed through an effective Bohr radius) and the reduced mass. A more strongly bound exciton (larger E_b) generally corresponds to a smaller real-space extent and thus a smaller diamagnetic response for a given mass.

Figure 25a shows the reflectivity spectrum of $(BA)_2(MA)_2Pb_3I_{10}$ in the range of 1s excitonic resonance measured at 0 and 65 T. The extracted 1s exciton energy versus the magnetic field is presented in figure 25b. The fitting procedure yields $c_0 = 0.95\mu\mathrm{eV}/\mathrm{T}^2$, a value consistent with similar studies on other quasi-2D perovskites with $E_b \simeq 100\,\mathrm{meV}$ [Urban *et al.*, Journal of Physical Chemistry Letters, **11**, 15 (2020)].

With $E_b \approx 100\,\mathrm{meV}$ and Ω_R reaching $\sim 155\,\mathrm{meV}$, the system operates in a regime where the coupling strength is comparable to the Coulomb binding scale. This comparison underpins the interpretation that the microcavity platform approaches the VSC limit, where coupling can involve higher excitonic states and the continuum and may renormalize excitonic parameters. The high-magnetic-field corroboration of E_b is therefore a central supporting element; it strengthens the quantitative basis for the VSC claim by anchoring the exciton binding energy to field-dependent excitonic physics rather than a single zero-field spectral model.

For more details please see [Adl *et al.*, Advanced Optical Materials, **13**, 30 (2025)].

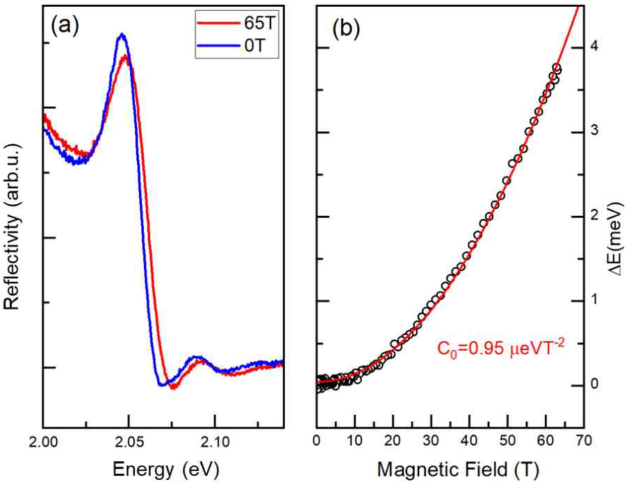

FIG. 25. *The reflectivity spectra at $T = 2\,K$ in $0\,T$ (blue) and $65\,T$ (red) for $(BA)_2(MA)_2Pb_3I_{10}$. (b) Relative energy shift of the 1s exciton energy as a function of the magnetic field together with a fit to the diamagnetic shift $E(B) = c_0 B^2$.*

P. Peksa, P. Plochocka
H. Adl, C. Bennenhei, M. Struve, M. Gittinger, C. Lienau, M. Esmann, C. Schneider (Universität Oldenburg), M. Dyksik, M. Baranowski (Wroclaw University of Science and Technology), K. W. Song (Xiamen University Malaysia, Sepang), J. Konig, J. M. Fitzgerald, E. Malic (Philipps-Universität Marburg), N. Jasti (Weizmann Institute of Science, Rehovot), F. Eilenberger (Fraunhofer-Institute for Applied Optics and Precision Engineering, Jena), O. Kyriienko (University of Sheffield)

Spin-flip Raman scattering investigation of the electron g-factor in 2D layered perovskites

2D layered perovskites provide a versatile platform for exploring spin-related phenomena in strongly spin–orbit-coupled semiconductors. Their natural quantum-well structure—where electronically active Pb–I layers are separated by organic spacer cations—offers an unusual degree of structural tunability without changing the inorganic composition. The modifications of the organic spacer can induce octahedral tilting and lattice distortions in the PbI_6 framework, which in turn reshape the electronic band structure and influence carrier spin properties. Quantifying how these structural degrees of freedom affect the electron g-factor is therefore important for understanding and controlling spin physics in metal–halide perovskites, with implications for magneto-optical response and spin-dependent scattering processes.

Spin-flip Raman scattering (SFRS) provides a direct optical route to measure Zeeman splittings and extract carrier g-factors with high precision. While SFRS is generally extremely weak in conventional semiconductors, the combination of a soft lattice and strong spin–orbit coupling in layered lead–halide perovskites makes spin-dependent light scattering unusually accessible. Here, we use low-temperature SFRS to determine electron g-factors in a series of 2D iodide perovskites with systematically varied organic spacers, and we relate the extracted g-factors to structural distortion parameters and excitonic energetics.

We have investigated a series of layered 2D perovskites—$(PEA)_2PbI_4$, $(BA)_2PbI_4$, $(p\text{-}BrPEA)_2PbI_4$, $(o\text{-}BrPEA)_2PbI_4$, and $(OA)_2PbI_4$. SFRS measurements were performed in external magnetic fields up to 16 T, with resonant 473 nm excitation.

A representative SFRS map for $(BA)_2PbI_4$ is shown in figure 26. For each compound, we determine the electron g-factor (g_e) from the slope of the spin-flip energy shift versus magnetic field. The extracted values are $g_e = 2.072$ for $(PEA)_2PbI_4$, 2.086 for $(p\text{-}BrPEA)_2PbI_4$, 2.128 for $(o\text{-}BrPEA)_2PbI_4$, 2.150 for $(BA)_2PbI_4$, and 2.162 for $(OA)_2PbI_4$.

2D perovskites exhibit octahedral tilting distortions that can be tuned by changing the organic spacer while preserving the Pb–I inorganic framework. These distortions are commonly quantified by two characteristic angles: the in-plane tilt angle β and the out-of-plane tilt angle δ [Dyksik *et al.*, Advanced Energy Materials, **15**, 9 (2025)].

The right panels in figure 26 show g_e as a function of the distortion angles and the 1s exciton energy. Overall, g_e increases with increasing structural distortion and with higher exciton energy. Although the dependence is not strictly linear, the trend suggests that both octahedral tilting and the associated changes in electronic structure contribute to tuning the electron spin response in these materials.

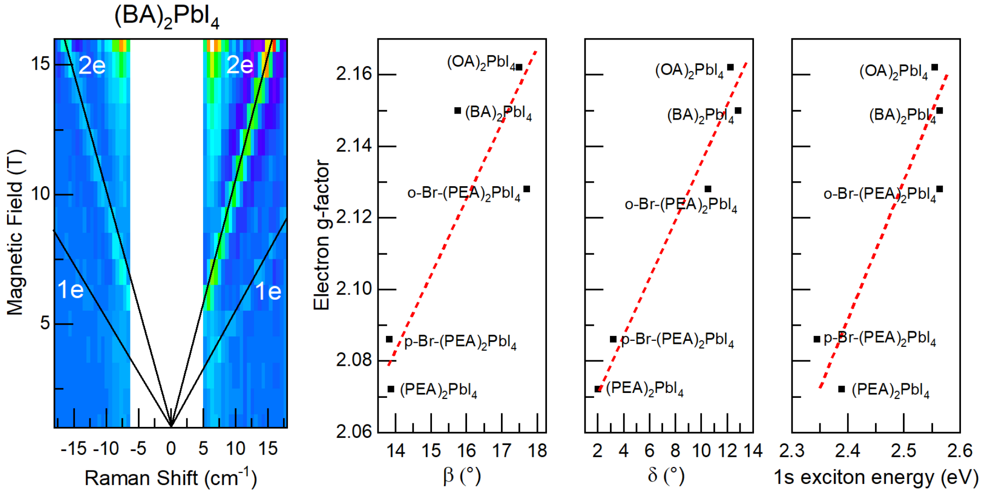

FIG. 26. *(a) False color map of SFRS intensity as a function of Raman shift and magnetic field for $(BA)_2PbI_4$. Single electron spin-flip line is marked as 1e and the double spin-flip as 2e. (b-d) Extracted electron g-factor plotted against in-plane distortion angle β, out-of-plane distortion angle δ, and 1s exciton energy.*

P. Plochocka
K. Widaj, M. Dyksik (Wroclaw University of Science and Technology), M. Molas, Ł. Kipczak (Warsaw University), Van Gompel, A. Maufort (Hasselt University)

Tunable broadband emission via self-trapped excitons and Mn^{2+} energy transfer in a 0D hybrid manganese bromide

Low-dimensional (2D, 1D, and 0D) hybrid organic-inorganic perovskite-like materials are a rapidly developing class of compounds with strong potential for light-emitting applications. Derived from self-assembled metal-organic frameworks with tunable composition, these materials allow emission properties to be tailored through structural design. While many low-dimensional perovskites show excellent luminescence, their lead content and limited stability motivate the search for lead-free alternatives. $MnBr_{4-}$ based compounds have attracted significant interest due to their low cost and potential as efficient white-light sources. Luminescent Mn^{2+} complexes exhibit color-tunable, high-efficiency, and long-lived emission, making them promising for optoelectronic applications. In particular, 0D $MnBr_{4-}$ based halides show bright photoluminescence arising from diverse coordination environments. Octahedrally coordinated Mn^2+ ions emit broadband red light, while tetrahedral coordination yields green emission, both originating from Mn^{2+} d-d transitions. Current consensus attributes this efficient emission primarily to self-trapped excitons or Mn^{2+} electronic transitions, driven by strong electron-phonon coupling.

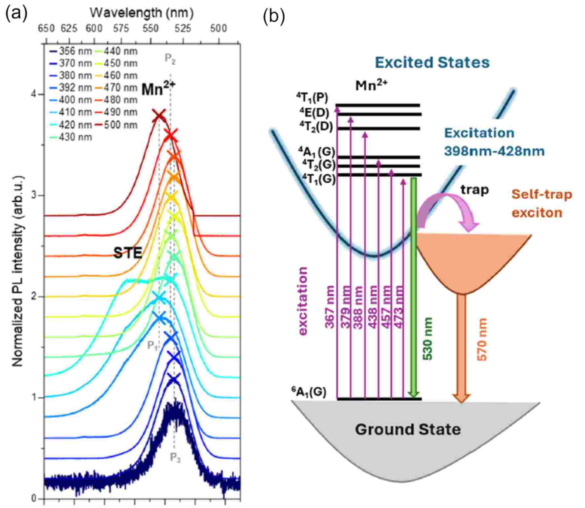

FIG. 27. *(a) Comparison of normalized PL spectra measured at 4 K for* $(TMBM)_2MnBr_4$ *single crystal at different excitation wavelengths; the vertical lines P1, P2, and P3 correspond to different positions of* Mn^{2+} *in the crystal structure; STE and* Mn^{2+} *indicate bands corresponding to exciton and manganese(II) emission. (b) Schematic illustration of the energy transition and exciton dynamics leading to the dual-band emission in* $(TMBM)_2MnBr_4$

Photoluminescence studies of $(TMBM)_2MnBr_4$ reveal a complex emission mechanism governed by the interplay between Mn^{2+} *d–d* transitions and self-trapped exciton emission (STE), which is strongly influenced by temperature and external magnetic field. At low temperatures, the compound exhibits intense broadband green emission centred near 2.30 eV, primarily originating from tetrahedrally coordinated Mn^{2+} ions. In addition, a weaker, lower-energy band is observed and attributed to STE emission, characterised by a strong excitation wavelength dependence (figure 27(a) and rapid thermal quenching.

Magneto-photoluminescence measurements performed in pulsed magnetic fields up to 65 T show a clear magnetic-field-induced shift of the PL peak at low temperatures. At 30 K and below, the emission exhibits a gradual red-shift with increasing magnetic field (figure 28(a), while no significant shift is detected at higher temperatures (figure 28(b), consistent with the paramagnetic nature of the material. The magnitude of the field-induced red-shift increases upon cooling, indicating enhanced coupling between localized excitonic states and Mn^{2+} spins. These results suggest that the magnetic field modifies the energy landscape of STEs and/or excited Mn^{2+} states, stabilizing localized excitons at low temperatures. As temperature increases, STEs are thermally destabilized, and the emission becomes dominated by Mn^{2+} recombination, resulting in a reduced magnetic-field response. Overall, the PL studies demonstrate a clear magneto-optical response arising from the coexistence of STEs and Mn^{2+} emission in this zero-dimensional hybrid system. More details can be found in [Peksa, *et al.*, Small, **21**, e04786 (2025)]

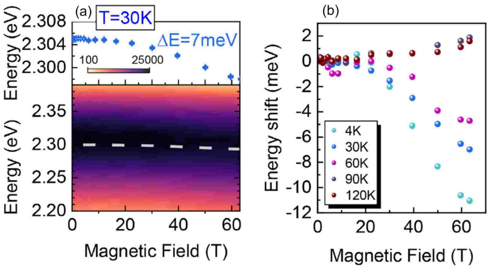

FIG. 28. *(a) The false-colour plot of the PL spectrum shows the energy shift in extreme magnetic fields (bottom graph) and magnetic field-induced energy shift of the PL (top graph) at 30 K. (b) Peak energy shift in the magnetic field at 4, 30, 60, 90, and 120 K.*

P. Peksa, P.Plochocka
M. Dyksik, A. Surrente, M. Baranowski, A. Sieradzki (Wroclaw University of Science and Technology), M. Ptak, D.Drozdowski, A.Gagor, J.Osmólska, A. Pikul, D. Szewczyk (Institute of Low Temperature and Structure Research, Polish Academy of Sciences, Wroclaw), J. Osmólska (Cavendish Laboratory, University of Cambridge), A. Kuc (Helmholtz-Zentrum Dresden-Rossendorf)

Transport evidence of surface states in the magnetic topological insulator $MnBi_2Te_4$

In ultra-thin films, magnetic topological insulators are known for their dissipation-less transport properties, associated to the quantum anomalous Hall effect, of importance for quantum metrology. For thicker nanostructures, quantization is severely reduced by the co-existence of edge states with other quasi-particles (usually attributed to bulk states). However, due to a strong degree of disorder, it remains difficult to identify the nature of these electronic sub-bands by electrical measurements.

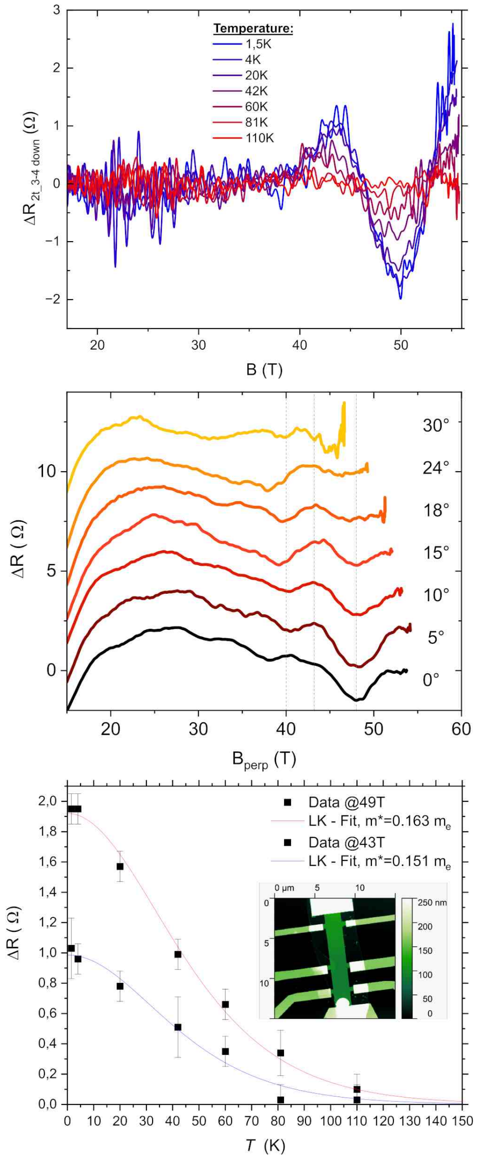

FIG. 29. *Nanostructure of* $MnBi_2Te_4$ *(inset) showing clear Shubnikov de Haas oscillations as a function of temperature and angle. The temperature dependence yields the effective mass (bottom). The angular dependence (middle) shows these oscillations come from a 2D band.*

Here, we report on 2D surface-state transport in $MnBi_2Te_4$ nanostructures, as evidenced by angular dependent high-field transport measurements up to 55 T. These states are clearly identified through Shubnikov de Haas (SdH) oscillations, and the results are supported by a detailed analysis of their temperature and angle dependence. Moreover, by considering all transport results including the Hall response, a quantitative band-bending model allows us to identify both bulk and surface states in thick $MnBi_2Te_4$ nanostructures. This finding of 2D surface states is important to better understand the transport properties in magnetic topological insulators. Especially in the quantum anomalous Hall regime as additional electronic states increase the backscattering rate of topological edge states. Current efforts in topological quantum and nanoscale materials research are constrained by the difficulty of studying independently the electronic properties of bulk and surface states, especially in systems where bulk conduction masks the topological signatures. Our study provides a direct way of accessing the properties of the surface states through Landau level spectroscopy in very high magnetic fields, despite relatively strong disorder.

The detailed analysis of the temperature-dependence of the SdH oscillations and the Hall effect (figure 29), yields quantitative values of mobility, charge carrier density and effective mass of the surface state. The band-bending model yields properties of both surface and bulk states that are consistent with known details on the band structure from ARPES. Finally, the analysis of the dimensionality of the SdH oscillations through angle-dependent measurements and the consistency of the band-bending model clearly exclude 3D bulk states as the origin of the observed SdH oscillations and prove their 2D nature.

These findings offer new insight into the charge transport properties of magnetic topological insulator nanostructures, by showing how topological surface states affect the band structure at interfaces, and how they can be directly probed and analyzed by means of transport measurements. This research on magnetic topological insulators is of interest both for materials science and functional quantum devices.

For more details please see [Wissmann *et al.* Arxiv.2512.04063].

M. Leroux, M. Pierre, M. Goiran, W. Escoffier, L. Veyrat
M. Wissmann, R. Giraud, B. Mehlhorn, J. Dufouleur, B. Büchner (Leibniz Institute for Solid State and Materials Research, IFW Dresden), A. Isaeva (Institute of Physics, University of Amsterdam))

Wide electrical tunability of the valley splitting in a doubly-gated silicon-on-insulator quantum well

The valley in which electron reside in the momentum space of the Brillouin zone (BZ) is a pivotal quantum degree of freedom in solid-state physics. While it can potentially be used in a similar fashion as spins are used to convey quantum information, within the emerging field of "valleytronics", a valley degeneracy can also be an undesirable source of quantum decoherence in low dimensional spin-based Quantum-bits (qubits) systems. Silicon, which is both the pillar of modern electronics and a suitable material for the realization of spin qubits, has a six-fold bulk valley degeneracy in the conduction band with degenerate energy minima lying close to the six X points of the BZ. In electronic systems confined into a plane perpendicular to the [100] direction, this six-fold bulk degeneracy is thus reduced to two because of the different [100] effective masses in longitudinale and in-plane valleys.

In spite of the ubiquitous use of 2D silicon, our understanding of how the degeneracy of these two valley energy levels can be lifted in actual devices is still uncomplete. Early theories have pointed out that inter-valley scattering (leading to "valley splitting") can occur in the presence of an abrupt interface. Measurements in singly-gated MOSFETs systems have demonstrated that the valley splitting increases with increasing densities of carriers n, consistent with a role played by the (density-induced) electric field at the interface. While such observations can be qualitatively foreseen with the theory of the "electric breakthrough" (where the electric field tends to push the electronic wave function into the barrier and enhance the role of the interface), the absence of a systematic disentanglement between vertical electric fields and carrier density and the remaining quantitative variations from one system to another call for further characterization of silicon devices displaying different interfaces in the presence of variable (and controlled) electric fields.

In this work [Aubergier *et al*, Nanoletters **25**, 13557 (2025)], we present a study of the valley splitting in doubly-gated silicon-on insulator quantum wells (see figure 30(a)) using low temperature transport measurements under magnetic and electric fields. The double gate configuration allows for a disentanglement of effects related to the electron density, on the one hand, and to electrostatic bias $\delta n = n_B - n_F$ where n_B (n_F) is the contribution from the back (front) gate to the total density, on the other hand. This latter is found to be the key parameter driving the strength of the valley splitting, which can reach value as high as 6.3 meV as electrons are pushed towards the bottom SiO_2 thermal oxide of our device, independent from the channel total carrier concentration $n = n_B + n_F$.

More precisely, we show that the wave function modulus at the interface ($\mid \Psi(z = z_i) \mid^2$) and its penetration within the barrier, which are the relevant quantities in the theoretical description of interface-induced valley splitting made by Saraiva *et al* [Saraiva *et al*, Phys. Rev. B. **80**, 081305 (2009)], are both proportional to the electrostatic bias δn and independent of n. The role of the nature of the interface in determining the valley splitting is confirmed by the lower splitting observed a the front interface of our device made out of a thin "high-k" dielectric. The interface and electric field-dependent valley splitting therefore results in a wide tunability within a single device, opening new perspectives to engineer valley-tunable devices or maximize the valley splitting to enhance spin coherence in silicon spin qubits.

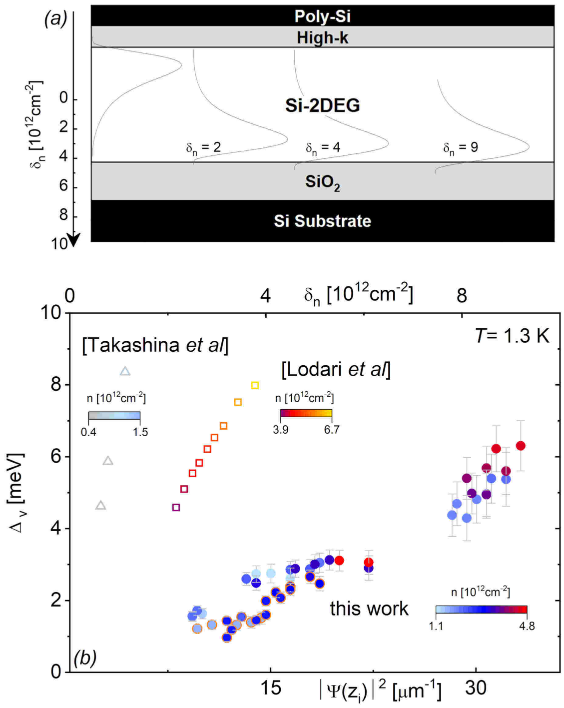

FIG. 30. *(a) Schematic representation of the studied doubly-gated silicon-on-insulator transistors. (b) Valley splitting Δ_V as a function of the electrostatic bias δn (top axis) or the electronic wave function modulus at the interface $\mid \Psi(z = z_i) \mid^2$. Data were obtained from a revisited Landau level "coincidence" method. Data obtained for other silicon 2DEGs in the literature are shown as open symbols. For these latter, only the bottom x-axis scale ($\mid \Psi(z = z_i) \mid^2$) is relevant in this plot.*

N. Aubergier, B.A. Piot
V.T. Renard (Université Grenoble Alpes, CEA, IRIG, PHELIQS, Grenoble), S. Barraud (CEA, LETI, Grenoble), K. Takashina (University of Bath)

Metals, Superconductors and Strongly Correlated Systems

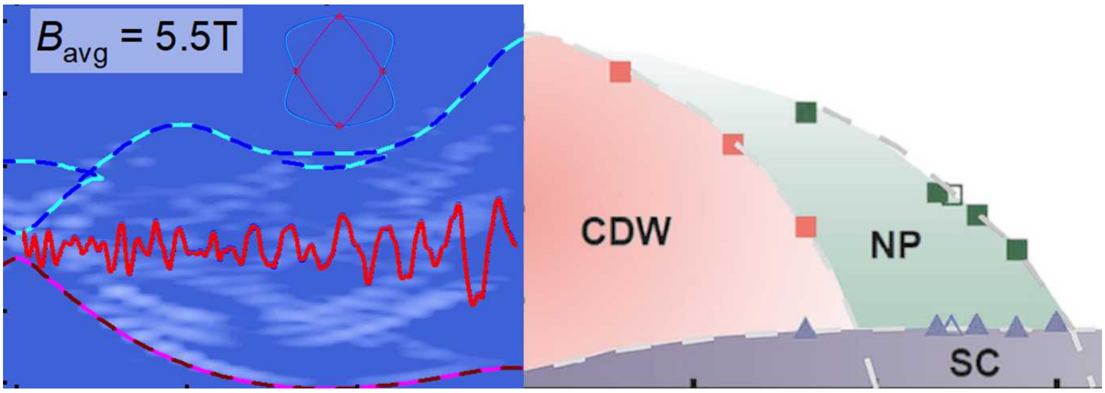

Quantum confinement effects in the topological Dirac semi-metal α-Sn on InSb(111)

α-Sn is one of the most promising and especially attractive candidates in the field of topological materials, due to the presence of various quantum phases that are tunable via material properties or by applying external electromagnetic fields. Epitaxy on a non-commensurate substrate is one of the conventional strategies to reduce the lattice symmetry and tailor the electronic structure and the quantum phase. Specifically, in the case of a compressive strain, α-Sn turns out to be a three-dimensional (3D) topological Dirac semi-metal (TDS), whereas a tensile strain yields a 3D topological insulator (TI).

In this work, we conduct thickness-dependent investigations through electrical and magneto-optical measurements of thin films grown directly on InSb(111) substrates, whose thickness of α-Sn was varied between 5 and 50 nm.

α-Sn is deposited by MBE at room temperature on undoped Sb-terminated InSb(111) substrate. The samples are characterized by in situ X-ray photoelectron spectroscopy (XPS) and by Raman spectroscopy. The transport properties of different α-Sn epilayer thicknesses have been characterized (5, 10, and 20 nm) using the single-channel structure schematized in figure 31. A drastic increase in the amplitude of the thermal gap takes place as the epilayer thickness decreases. Similarly, the peak resistance scales with the film thickness. Such a finding provides striking evidence for the emergence of quantum-size effects in the conduction of α-Sn/InSb(111). To gain a more quantitative understanding of conduction mechanisms, particularly at the Γ-valley, we measured the low-temperature absorption in the far-infrared (IR), focusing on as-grown α-Sn films of 10, 20, and 50 nm. In figure 32(a-c), we report the set of data for all three samples investigated.

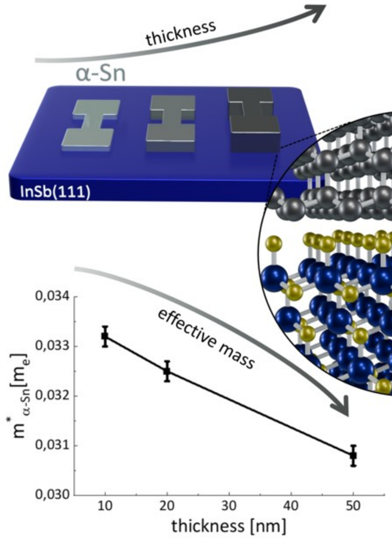

FIG. 31. *The application of a compressive strain on α-Sn turned out to induce a topological Dirac semi-metal phase. Quantum confinement effects on thin α-Sn films reveal a thickness-dependent electrical transport and the change of the effective masses of the charge carriers.*

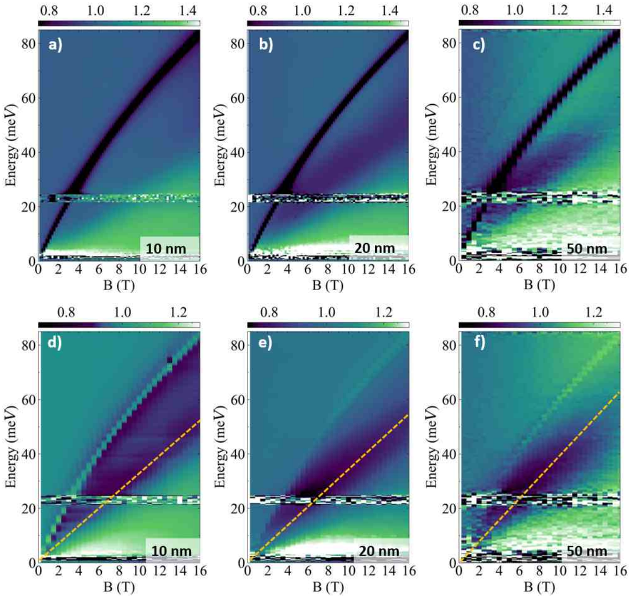

FIG. 32. *Relative magneto-transmission, $T_s(B)/T_s(0)$, collected on α-Sn samples with the thicknesses of a) 10 nm, b) 20 nm, and c) 50 nm. For comparison, the same set of data with additional normalization by relative magnetotransmission of the bare InSb substrate is reported in (d-f), respectively. The yellow dashed lines highlight the CR line in the α-Sn films.*

The pronounced dip is easily identified as cyclotron resonance of bulk electrons in bulk InSb. To enhance the signal from the α-Sn layer, we also plot the substrate normalized magneto-transmission. This corresponds to relative magneto-transmission of the sample, $T_s(B)/T_s(0)$, additionally normalized by relative magneto-transmission of the bare InSb substrate, $T_{ref}(B)/T_{ref}(0)$ (see figure 32(d-f)). The transmission minima at the resonance lines, provide us with the effective masses ($m^\star$). The thickness-induced change in $m^\star$ demonstrates that the TDS transport is governed by carriers that become progressively lighter as the α-Sn thickness increases. Such data represent the first estimate of the effective masses for α-Sn directly grown on InSb(111).

More details about this work can be found in [Massetti *et al.*, Matter, **8**, 102194 (2025)].

M. Orlita, F. Le Mardelé, I. Mohelsky
C. Massetti, C. Martella, A. Molle, C. Grazianetti (CNR-IMM, Agrate Brianza), C. Crosta, F. Pezzoli (Dip. di Scienza dei Materiali, Università degli Studi di Milano-Bicocca, Milan)

Fermi surface and magnetic breakdown in PdGa

The class of B20 materials comprises a variety of compounds with interesting magnetic, optical, and transport properties. Recently, there has been increased interest in the non-magnetic members that feature topologically non-trivial band structures. The crystalline symmetries enforce multifold band crossing points and nodal plane degeneracies that extend over the entire Brillouin zone (BZ) boundary and may carry a large topological charge without upper bound. Another common theme in these materials is a SOC-induced band splitting that splits the Fermi surface at general points in the BZ. Combined with the nodal plane degeneracies this results in mutually intersecting, nested Fermi surface pockets at the BZ boundary.

We have performed a comprehensive quantum oscillation study on PdGa. By combining Shubnikov-de Haas and de Haas-van Alphen measurements, we resolved the entire Fermi surface. A detailed analysis revealed the importance of SOC-induced band splitting and magnetic breakdown (MB) between individual trajectories and their interplay with the nodal plane degeneracies. Using torque magnetometry in high magnetic fields (figure 33 (a)), we tracked the evolution of MB trajectories, including higher-order branches that involve multiple revolutions around the Fermi surface.

Figure 33 (b) shows an example of such trajectories. The part of the Fermi surface centered around the R-point features two inner and two outer pockets that pairwise intersect each other at the boundary of the Brillouin zone. MB may occur where the inner and outer trajectories are close to each other, as indicated by the red circles. In the case of nested pockets, MB leads to oscillation frequencies in the range bounded by the non-breakdown frequencies.

Figure 33 (c-d) show the dHvA oscillation spectra as a function of the angle of the applied magnetic field θ for two different field windows. The frequency range shown corresponds to the frequencies arising from the trajectories shown in (b). The frequency branches predicted from first principles calculations without considering magnetic breakdown are marked by dashed lines. These two branches correspond to the outer and inner pairs of trajectories. Even at low magnetic fields [Figure 33 (c)], frequency contributions in between these branches are detected, indicating that magnetic breakdown is already possible. When the data is evaluated at higher fields (figure 33 (d)), the spectral weight shifts strongly towards the branches in the center of the frequency range. These inner branches correspond to trajectories for which magnetic breakdown occurs at every breakdown junction.

Using the Fermi surface obtained from DFT, we calculated the various MB trajectories, their respective probabilities, and expected oscillation amplitudes. We find a very good agreement with the experimentally detected spectra. Furthermore, we detected frequency branches at higher frequencies that correspond to MB trajectories involving multiple revolutions around the Fermi surface. In contrast to conventional harmonic frequencies, only certain combinations of trajectories lead to closed orbits. This results in distinct frequency branches being more pronounced in the regions containing higher-order breakdown frequencies.

Taken together our results confirm (i) the existence of nodal plane degeneracies on the BZ boundary, (ii) a SOC-induced band splitting, and (iii) partial magnetic breakdown between individual pockets that evolves with the magnetic field strength.

More details on this work are published in [Huber *et al.*, Phys. Rev. B. **112**, 085116 (2025)].

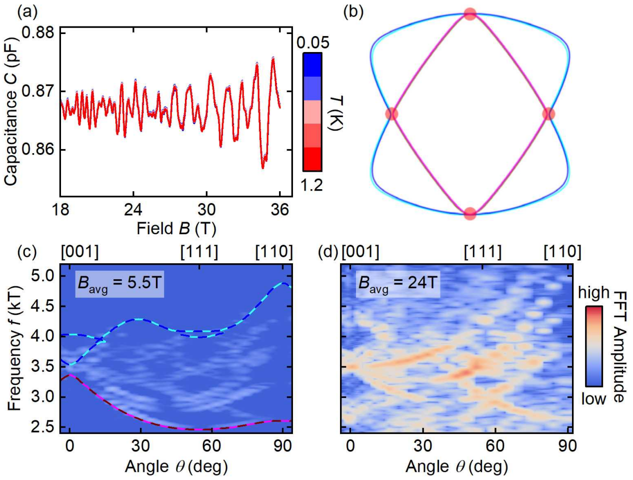

FIG. 33. *Magnetic breakdown in PdGa. (a) Quantum oscillations (QOs) detected via cantilever-based torque magnetometry. (b) Extremal trajectories on the Fermi surface pockets at the R-point perpendicular to the [110] direction. Magnetic breakdown (MB) junctions are marked by red circles. (c),(d) QO spectra arising from the R-point as a function of field angle. Dashed lines are calculated from DFT trajectories without MB. At high magnetic fields spectral weight shifts towards the center of the frequency range between the enclosing non-MB branches.*

I. Sheikin
N. Huber, I. Volkau, A. Engelhardt, A. Bauer, C. Pfleiderer, M. A. Wilde (Technical University of Munich, Garching)

Robust charge-density wave correlations in optimally-doped $\mathrm{YBa_2Cu_3O_y}$

Over the last decade, it has been established that charge-density wave (CDW) order is a key, universal property of high-T_c cuprates and that it also emerges as a ground-state property of the simplest version of the Hubbard model on a square lattice within a parameter regime relevant to real, superconducting compounds – namely a hole density $p \sim 0.1$ per unit cell and a ratio $U/t \simeq 8$ between of the on-site Coulomb repulsion U to the nearest-neighbor hopping t.

An outstanding issue, however, is whether the boundaries of the CDW phase correlate with other key features of the cuprate phase diagram as a function of p and temperature T, including superconductivity itself. More specifically, a key question is whether the critical doping up to which the CDW exists on the high-doping side coincides with any of the following; the optimal doping for superconductivity at $p \simeq 0.16$, the end of the superconducting dome at $p \simeq 0.3$, the end of the pseudogap phase at $p^* \simeq 0.19$ (and concomitant onset of the strange metal phase), or none at all. Experiments across different cuprate families and using different probes have so far provided conflicting answers.

In the present work [Zhou *et al.* Phys. Rev. Lett. **135**, 106503 (2025)], we address this question using ^{17}O nuclear magnetic resonance (NMR) measurements in near-optimally-doped single crystals of the prototypical cuprate $\mathrm{YBa_2Cu_3O_y}$ (YBCO). This extends our earlier work in the underdoped regime, which established that short-range CDW order induces a spatial inhomogeneity of the electric-field gradient that can be detected through careful measurements and analysis of the quadrupole contribution w_{quad} to the NMR line broadening.

Our key result, shown in figure 34, demonstrates that short-range static CDW order remains robust at optimal doping ($p = 0.165$), exhibiting a strength and temperature dependence in the normal state similar to those observed at $p = 0.109$ in the underdoped regime.

For a slightly overdoped sample with $p = 0.184$ (but still in the pseudogap state), we detect no static CDW down to $T = T_c$ (figure 34). However, we argue that weak CDW order plausibly emerges below T_c, which could not be probed here because of the shielding of the radio frequency in the superconducting state.

Given the proximity of $p \simeq 0.16$ to the pseudogap boundary $p^* \simeq 0.19$, we conclude that it is highly unlikely that the CDW phase terminates significantly before p^* in YBCO. This result contradicts the influential view, based on early X-ray scattering studies, that short-range CDW order is weak or absent at $p \simeq 0.16$. It also implies that one should no longer rule out the possibility that short-range CDW correlations play a role in the change of the electronic properties observed as a function of doping across p^*.

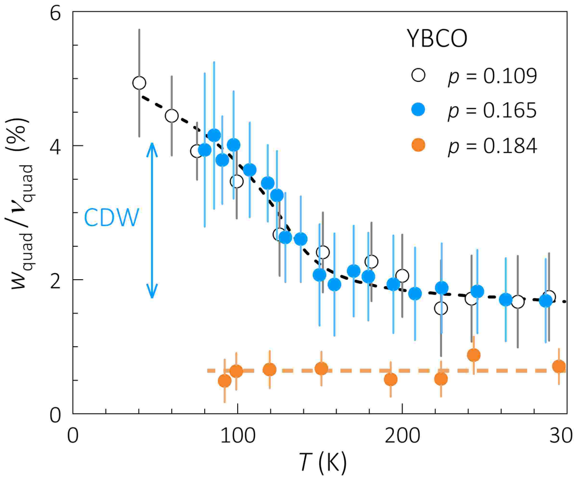

FIG. 34. *Quadrupole contribution to the width w_{quad} relative to the quadrupole frequency $\nu_{\mathrm{quad}} = (\nu_{\mathrm{HF1}} - \nu_{\mathrm{LF1}})/2$ where ν_{HF1} (ν_{LF1}) is the resonance frequency of the first high (low) frequency satellite for the O(3) site, corresponding to planar oxygen atoms involved in bonds oriented along the b axis. The temperature dependence of w_{quad} directly reflects the growth of short-range, static CDW correlations.*

Finally, it is important to recognize that a sharply defined endpoint for CDW order as a function of hole doping may simply not exist. The coexistence of spatially separated regions with and without static CDW order and doping-dependent volume fractions – often challenging to identify experimentally – remains a distinct possibility beyond optimal doping. More broadly, our work highlights that the question of the CDW phase boundaries is more intricate than often assumed; both quenched disorder and competition with superconductivity affect the p and T dependence of the CDW, which complicates the determination of its phase boundaries and likely leads to an underestimation of the intrinsic extent of this phase in the (p, T) phase diagram.

R. Zhou, I. Vinograd, H. Mayaffre, M.-H. Julien
J. Porras, H.-H. Kim, T. Loew, Y. Liu, M. Le Tacon, B. Keimer (Max-Planck-Institut für Festkörperforschung, Stuttgart)

Impact of low-energy spin fluctuations on the strange metal in a cuprate superconductor

Strange metals, which exhibit unusual properties such as a resistivity that scales linearly with temperature, challenge our understanding of charge transport in metals. A general and puzzling feature of the strange metal is a linear-in-T resistivity existing over a wide region of the phase diagram in the limit of low temperature. In contrast, linear resistivity down to the lowest T is observed in quantum critical metals, but only at a singular point in the phase diagram. A common ingredient in theories of strange metals is the existence of a low-energy degree of freedom that can effectively couple to charge carriers down to the lowest T. In high-T_c cuprate superconductors, the nature and origin of these low-lying excitations remain elusive.

We use magnetic fields as high as 86 T to explore the physics of strange metals in the cuprate superconductor $La_{2-x}Sr_xCuO_4$ (LSCO). Close to the critical doping of the pseudogap, $p^* = 0.19$, we discover that T-linear resistivity persists down to the lowest T over an extended range of magnetic field. As shown in Figure 35(a), this extended regime of linear-in-T resistivity exists between 60 and 70 T and disappears above. Above 70 T, a spin glass phase gradually emerges, as previously observed using ultrasound measurements. Nuclear Magnetic Resonance (NMR) and ultrasound studies have shown that in LSCO near p^*, low-T magnetic fluctuations exist over an extended range of magnetic field but are eventually quenched in high fields, leading to a spin glass phase.

Our transport measurements reveal that spin freezing marks the end of strange metallicity, as illustrated schematically in the phase diagram of figure 35(b). These results demonstrate that the strange metal phase can be controlled with magnetic field via spin dynamics and is closely linked to low-energy magnetic fluctuations persisting at the lowest temperatures.

Inside the magnetically frozen phase, the magnetoresistance is greatly enhanced. Resistivity upturns, a signature of the metal-insulator crossover in LSCO, appear at low temperatures in the spin glass phase. This indicates that the metal-insulator crossover is linked to spin freezing. Thus, spin freezing drives a crossover from a strange metal with linear-in-T resistivity to a distinct metallic state with insulating-like resistivity.

For more information, please refer to [Campbel *et al.*, Nature Physics **21**, 1759 (2025)].

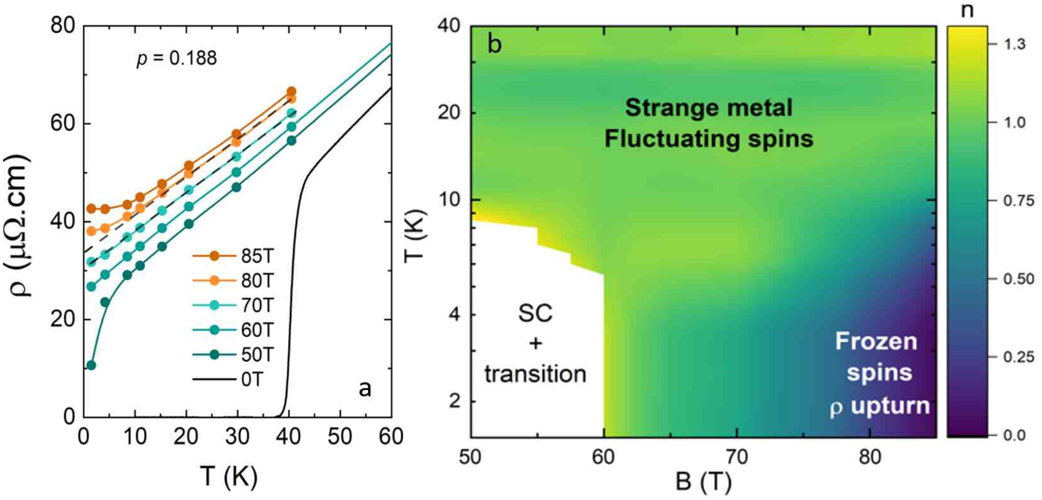

FIG. 35. *(a) Resistivity of LSCO ($p = 0.188$), near the pseudogap critical doping $p^\star = 0.19$, as a function of temperature, for various magnetic fields ranging from 50 T to 85 T (full circles). Dashed lines are fits to the data. Black line is the zero field curve showing superconducting T_c. (b) False color plot of the exponent n of the temperature-dependent in-plane resistivity $\rho(T) = \rho_0 + aT^n$ for LSCO ($p = 0.188$). It is obtained from an interpolation of $\left(\frac{d\ln(\rho(T)-\rho_0)}{d\ln T}\right)$ calculated for different magnetic fields. The white area corresponds to the superconducting phase and the resistive transition. ρ_0 is the residual resistivity extrapolated to $T = 0$ from linear fits as shown in panel* **a**. *Green-ish area shows the strange metal behaviour,* i.e. *resistivity that scales linearly with T other an extended regime of magnetic field. Darker blue-ish area indicates departure from strange metal regime, in the form of resistivity upturn, due to spin freezing.*

D. J. Campbell, M. Frachet, V. Oliviero, D. Vignolles, C. Proust, D. LeBoeuf
T. Kurosawa, M. Oda (Hokkaido University, Sapporo), N. Momono (Muroran Institute of Technology, Muroran), J. Chang (University of Zurich)

Thermal Hall conductivity in the strongest cuprate superconductor: The mean free path in the trilayer cuprate $HgBa_2Ca_2Cu_3O_{8+\delta}$

The thermal Hall conductivity of the trilayer cuprate $HgBa_2Ca_2Cu_3O_{8+\delta}$ (Hg1223), the cuprate with the highest critical temperature at ambient pressure, was measured down to 2 K for dopings $p = 0.09$, 0.10, and 0.11. Using a simple model combined with the established expression for the nodal specific heat in a d-wave superconductor, we extract the inverse mean free path $1/\ell_s$ (figure 36) of nodal quasiparticles from the measured thermal Hall response. In all Hg1223 samples, $1/\ell_s$ increases as T^3, consistent with the clean d-wave expectation. Measurements on single-layer $HgBa_2CuO_{6+\delta}$ (Hg1201, $p = 0.10$) reveal a significantly shorter mean free path, whereas an ultra-clean $YBa_2Cu_3O_y$ crystal (YBCO, $p = 0.18$) exhibits values comparable to Hg1223. These results, presented in [Altangerel *et al.*, Phys. Rev. B **112**, 014522 (2025)], demonstrate the exceptional intrinsic cleanliness of Hg1223.

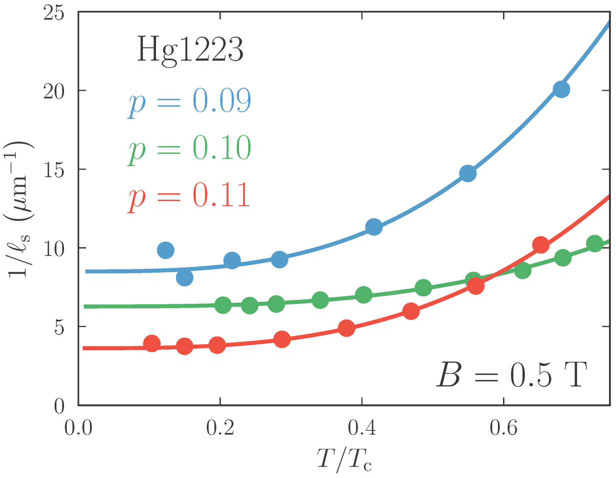

FIG. 36. *Inverse mean free path $1/\ell_s$ as a function of reduced temperature T/T_c for Hg1223 at 0.5 T: $p = 0.09$ (blue), $p = 0.10$ (green), and $p = 0.11$ (red). Markers represent the data points, while the lines correspond to T^3 fits ($a + bT^3$).*

The analysis builds on the weak-field approach to thermal Hall transport introduced in the cuprates by [Zhang *et al.*, Phys. Rev. Lett. **86**, 890 (2001)], which relates κ_{xy} to quasiparticle trajectories in the nodal regions. This framework allows one to determine the mean free path within the superconducting state, an essential advantage for materials whose normal state cannot be reached at low temperatures due to extremely large upper critical fields.

Across the three dopings of Hg1223, the temperature dependence and magnitude of κ_{xy}/B reveal a clear evolution of disorder; the $p = 0.11$ sample displays the strongest signal and the longest ℓ_{s0}, while $p = 0.09$ shows increased elastic scattering. The extracted residual mean free paths grow from $\simeq$ 1200Å at $p = 0.09$ to nearly 2800Å at $p = 0.11$. These values place Hg1223 among the cleanest known cuprates. The comparison with Hg1201 at identical doping highlights the role of structural layering: in Hg1223, the outer CuO_2 planes protect the inner plane from disorder, leading to much longer quasiparticle trajectories. YBCO at $p = 0.18$, often regarded as the benchmark for sample quality, shows a mean free path comparable to Hg1223, reinforcing the conclusion that the trilayer cuprate rivals the very cleanest YBCO crystals.

A complementary view comes from the field dependence of ℓ_s. In the cleanest samples, ℓ_{s0} nearly doubles when extrapolating from the value at 0.5 T down to $B \to 0$. This strong field dependence arises because the inter-vortex distance is much shorter than the mean free path, making ℓ_s highly sensitive to the vortex density. In contrast, in more disordered samples such as Hg1223 at $p = 0.09$ or Hg1201 at $p = 0.10$, the field dependence is much weaker: there, the average distance between impurities is shorter than the inter-vortex spacing, and ℓ_s is therefore limited by impurity scattering rather than by vortex-induced effects.

The extraction of ℓ_s depends on the effective interplane spacing d used to convert κ_{xy} into a 2D quasiparticle conductivity. If all three CuO_2 planes contribute, $d = c/3$, whereas attributing the signal solely to the inner plane, $d = c$, gives an upper bound on ℓ_s approaching 4600Å. In either scenario, Hg1223 exhibits very long mean free paths, consistent with the clean-limit behaviour and with the T^3 dependence of $1/\ell_s$, which may originate from scattering off spin fluctuations.

Overall, the combined results on Hg1223, Hg1201, and YBCO show that thermal Hall transport provides a powerful and quantitative probe of quasiparticle scattering in the superconducting state. The clean-limit behaviour and the strong sensitivity to structural layering make this approach well suited to mapping disorder and quasiparticle scattering across the cuprate phase diagram.

M. Altangerel, C. Proust
Q. Barthélemy, É. Lefrançois, J. Baglo, M. Mezidi, G. Grissonnanche, A. Vallipuram, E. Campillo, L. Taillefer (Université de Sherbrooke), A. Forget, D. Colson (Université Paris-Saclay, CEA), R. Liang, D. A. Bonn, W. N. Hardy (University of British Columbia, Vancouver)

Connecting high-field and high-pressure superconductivity in UTe_2

One of the most singular aspects of unconventional superconductivity (SC) is that a purely electronic pairing mechanism allows a multitude of possible superconducting pairing states. This opens the possibility of stabilizing several different superconducting states in the same material by varying external parameters such as temperature, magnetic field, and pressure. There are now hundreds of known unconventional superconductors, however, only a very few are known to display multiple superconducting states. The recently discovered superconductor UTe_2 is most intriguing as the field- or pressure-induced phases can have a higher critical temperature than the superconducting ground state (see figure 37).

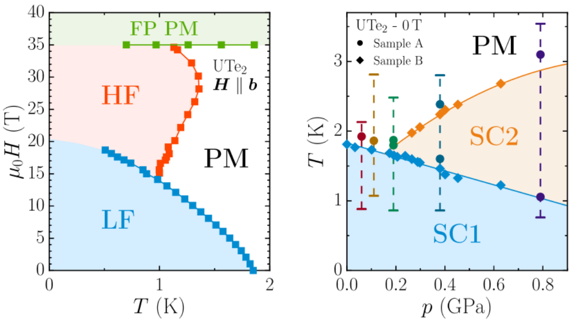

FIG. 37. *Multiple superconducting phases in UTe_2; at ambient pressure under magnetic field for $H \parallel b$ and under pressure in zero field. The dashed vertical lines show the pressures and temperature ranges for the present study. The LF phase is the same as the SC1 phase under pressure.*

It was first shown that when a small hydrostatic pressure is applied, two distinct superconducting transitions occur versus temperature. But the most remarkable phenomenon in UTe_2 with orthorhombic crystal structure is undoubtedly the effect of an applied magnetic field on its superconducting properties. In particular, when the field is applied along the b axis, a spectacular reinforcement of SC is found above 15 T up to a field of about 35 T, where a first-order metamagnetic transition H_M to a field-polarized paramagnetic state occurs (see figure 37). Precise calorimetry measurements in high magnetic field applied along b recently showed that there is a clear phase transition between a low-field (LF) and a high-field (HF) superconducting state.

Further characterizing and identifying these different superconducting phases is now a priority for UTe_2 as it is expected that some or all of them have a spin-triplet order parameter, highly sought after for its original fundamental properties as well as its interest in quantum engineering. Even the superconducting order parameter symmetry of the LF phase at ambient pressure has not been identified unambiguously. Obviously (see figure 37) the LF phase is the same as the SC1 phase under pressure, yet the link between the HF and SC2 phases still requires clarification. To resolve this question, we have performed ac calorimetry measurements under pressure in high magnetic fields for $H \parallel b$ on single crystals of UTe_2, thermodynamically tracking the different phases as well as their precise evolution with combined pressure and field.

As a result, the high-field superconducting phase (HF) at ambient pressure continuously evolves under pressure into the zero-field high-temperature superconducting phase SC2 (see figure 38). This bulk probe demonstration clarifies the complex superconducting phase diagram of UTe_2. Our results do not directly allow for a more precise determination of the symmetry of the order parameter in the SC2 phase. However, they open a new theoretical approach to the question of the mechanisms and symmetries characterizing the SC2 phase; the proposed scenarios should apply as well for the HF phase seemingly triggered by the approach to H_M, and for the high-pressure phase most likely emerging together with stronger antiferromagnetic fluctuations. This should both add guides and constraints to future models of SC in UTe_2.

For more information please see [Vasina *et al.*, Phy. Rev. Lett. **134**, 096501 (2025)].

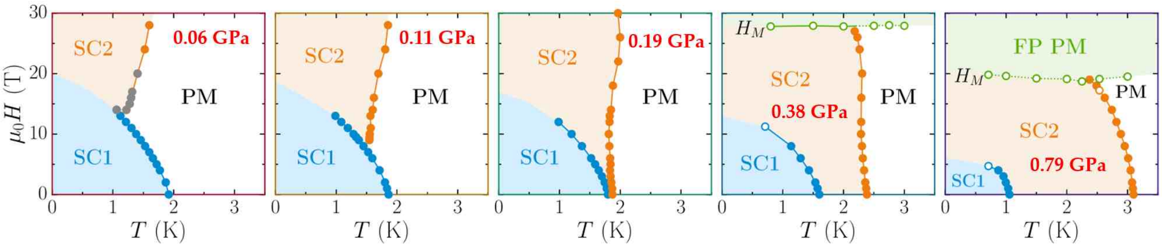

FIG. 38. *Pressure evolution of the phase diagram showing that the high-field superconducting phase at ambient pressure HF continuously evolves under pressure into the zero-field high-temperature superconducting phase SC2.*

G. Seyfarth
T. Vasina, A. Pourret, C. Marcenat, G. Lapertot, J. Flouquet, M. Amano Patino, J.-P. Brison, D. Braithwaite, G. Knebel (IRIG-PHELIQS, CEA Grenoble), D. Aoki, A. Miyake (Tohoku University, Oarai)

Quasi-2D Fermi surfaces of the antiferromagnet U_2RhIn_8

U_2RhIn_8 crystalizes into a tetragonal crystal structure with space group $P4/mmm$. It undergoes an antiferromagnetic transition at a Néel temperature $T_N = 117\,\mathrm{K}$. The Sommerfeld coefficient $\gamma = 47\,\mathrm{mJ/K^2mol}$ is rather large given the high Néel temperature. The magnetic structure determined by single-crystal neutron diffraction is commensurate with propagation vector $\mathbf{Q} = (1/2, 1/2, 0)$ and magnetic moments aligned along the c axis.

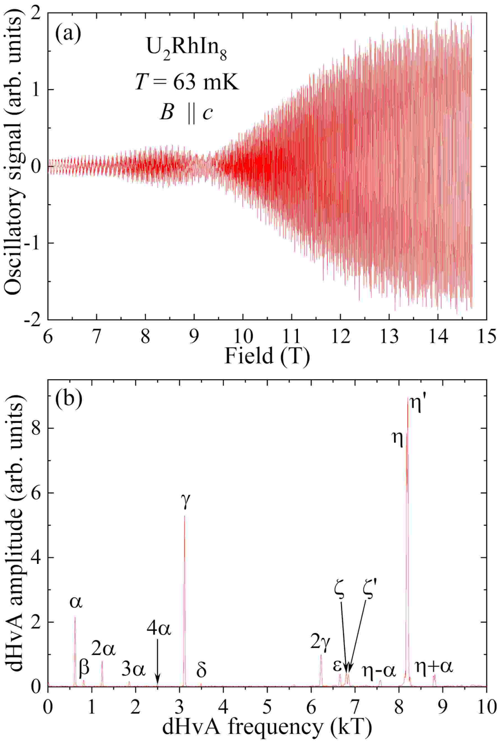

FIG. 39. *(a) The oscillatory signal after subtracting the non-oscillating background in U_2RhIn_8 for magnetic field applied along the c axis at 63 mK. (b) FFT spectrum of the dHvA oscillations from (a) over the field range from 6 to 14.7 T.*

In order to map the Fermi surface of U_2RhIn_8, we performed de Haas-van Alphen (dHvA) effect measurements. Figure 39(a) shows the oscillatory signal after subtracting the non-oscillating background for the magnetic field applied along the c axis at 63 mK. The low-frequency oscillations are clearly visible at a field as low as 6 T. At higher fields, high-frequency oscillations become dominant.

The fast Fourier transform (FFT) spectrum of the dHvA oscillations from figure 39(a) is shown in figure 39(b). For the field applied along the c axis, we observed seven fundamental frequencies denoted as α, β, γ, δ, ϵ, ζ, and η. In addition, we observed multiple harmonics of some of the dHvA frequencies as well as some linear combinations, *e.g.*, $\eta + \alpha$ and $\eta - \alpha$. Two fundamental frequencies, ζ and η, seem to be split into two close satellites.

The angle dependence of the dHvA frequencies is shown in figure 40. Branches α, $\gamma(\delta)$, and ε almost ideally follow the $1/\cos(\theta)$ dependence, where θ is the angle from the c axis. This dependence, shown by the dashed line in figure 40, is characteristic for a cylindrical Fermi surface found in 2D systems. Therefore, these branches originate from three distinct almost cylindrical Fermi surface sheets. The α branch is observed up to 35–40° from the c axis, while $\gamma(\delta)$ and ε branches can be traced up to 70–80°. The two branches γ and δ are close in frequency and converge at a small angle from the c axis. This suggests that they arise on the same quasi-2D FS sheet. The same is true for the ε and η branches. The β branch is observed only close to the c axis. It is not clear whether it corresponds to yet another quasi-2D sheet or the same one as the α branch. Several branches observed around the [110] direction probably correspond to more complex multi-connected Fermi surfaces. Remarkably, we have not observed any branches, which extend over the whole angle range. This rules out the existence of 3D isotropic Fermi surface pockets such as spherical or ellipsoidal.

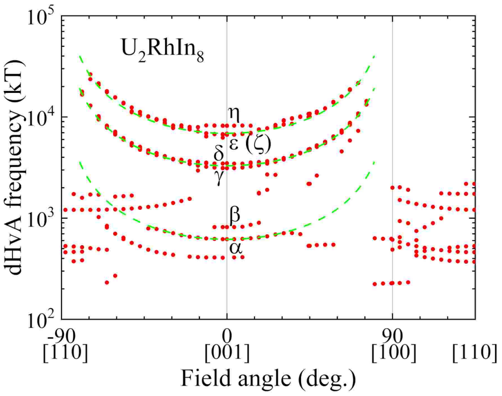

FIG. 40. *Angle dependence of the experimentally observed dHvA frequencies in U_2RhIn_8. Dashed lines represent $1/\cos(\theta)$ dependencies characteristic of cylindrical Fermi surfaces.*

Local density approximation band-structure calculations performed for the paramagnetic ground state reveal more three-dimensional Fermi surfaces than those observed in the experiment. On the other hand, Fermi surfaces obtained for the antiferromagnetic ground state by band-folding are more two-dimensional. These calculations account reasonably well for the experimental results assuming a slight modification of the calculated Fermi surfaces, as discussed in more details in [Aoki *et al.*, Phys. Rev. B **111**, 035155 (2025)].

I. Sheikin
D. Aoki, Y. Homma (Tohoku University, Oarai), H. Harima (Kobe University, Kobe)

Exotic magnetic phase diagram and extremely robust antiferromagnetism in Ce_2RhIn_8

Cerium-based intermetallic compounds exhibit a variety of fascinating phenomena including heavy-fermion behavior, quantum criticality, non-Fermi-liquid behavior, and novel states of matter such as unconventional superconductivity and, probably, electronic nematicity. Of particular interest is the $Ce_nT_mIn_{3n+2m}$ (T = transition metal) family, in which n conducting $CeIn_3$ layers are separated by m insulating TIn_2 layers along the c axis. The ground state of some of the family members, such as $CeIn_3$, $CeRhIn_5$ ($n = 1$, $m = 1$), and $CePt_2In_7$, is antiferromagnetic (AFM). All these compounds can be tuned to a magnetic quantum critical point (QCP), *i.e.*, a continuous magnetic phase transition at zero temperature, by hydrostatic pressure P or magnetic field H. In order to get further insight into field-induced QCPs, it is important to search for other compounds of the family, in which a QCP can be induced at a lower field accessible in static-field magnets. It is equally important to establish complete magnetic phase diagrams of the other AFM members of the family in order to better understand the origin of the field-induced phases in these compounds.

Ce_2RhIn_8 is another member of the family discussed above with $n = 2$ and $m = 1$. It crystallizes into a tetragonal crystal structure with space group $P4/mmm$. The electronic specific-heat coefficient $\gamma \simeq 400\,\mathrm{mJ/molK^2}$ characterizes Ce_2RhIn_8 as a moderate heavy-fermion compound. The material undergoes an AFM transition at a Néel temperature $T_N \simeq 2.8\,\mathrm{K}$. The magnetic structure determined from single-crystal neutron diffraction is commensurate with the propagation vector $\mathbf{Q} = (1/2, 1/2, 0)$ and the staggered moment of $0.55\mu_B$.

In order to establish magnetic phase diagrams of Ce_2RhIn_8, we performed high-field low-temperature specific-heat measurements on a high-quality single crystal. The measurements were carried out in static fields up to 35 T.

The resulting magnetic field temperature, $H-T$, phase diagram for field along the a axis is shown in the top panel of figure 41. Two additional field-induced phases, II and III, are observed, in agreement with previous reports. The phase II is confined in a small area of the field-temperature phase diagram. The phase III, which develops above $\simeq$2.5 T, is very robust against the field. Its transition temperature increases with field, reaches a maximum at $\simeq$12 T, and then starts to decrease. However, it tends to saturate towards the highest field of our measurements. As was already mentioned above, the zero-field phase I is commensurate AFM with a propagation vector $\mathbf{Q} = (1/2, 1/2, 0)$. The exact origin of the two other field-induced phases, II and III, is unknown at present. Nevertheless, both phases are certainly AFM. Indeed, the phase II emerges directly below T_N at low fields. As for the phase III, previous neutron-diffraction experiments, although performed for $H \parallel [110]$, revealed a finite intensity of the magnetic Bragg peak (1/2, 1/2, 1) up to 14.5 T at low temperatures.

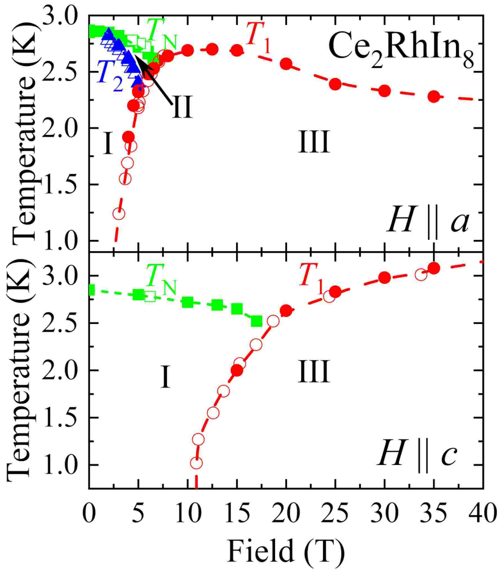

FIG. 41. *Magnetic phase diagram of Ce_2RhIn_8 obtained from specific-heat measurements performed as a function of temperature (solid symbols) and magnetic field (open symbols) for a field applied along the a (top panel) and c (bottom panel) axis.*

For a field applied along the c axis (bottom panel of figure 41), the Néel temperature, T_N, initially decreases with field, as expected for a typical antiferromagnet. Surprisingly, an additional phase, phase III, emerges above $\simeq$10 T. It is most likely to be of the same origin as its counterpart observed above 2.5 T for the other field orientation. This phase is also unusually robust: Its transition temperature increases all the way up to 35 T, where it exceeds the zero field $T_N = 2.85\,\mathrm{K}$.

The field-induced AFM phase III in Ce_2RhIn_8 is extremely robust against the magnetic field applied both along a and c axis. This is very unusual given that in ordinary antiferromagnets, antiferromagnetic order is continuously suppressed by the magnetic field, as discussed in more details in [Klein *et al.*, Phys. Rev. B **111**, L201110 (2025)]. Microscopic measurements, such as neutron diffraction and NMR, are required to establish the origin of this phase and to comprehend its unusual robustness against magnetic field.

A. Demuer, I. Sheikin
T. Klein (Université Grenoble Alpes), C. Marcenat (CEA, INP, IRIG, PHELIQS, Grenoble), D. Aoki (Tohoku University, Oarai)

Discovery of a new phase in thin flakes of KV_3Sb_5 under pressure

The Kagome lattice, a 2D network of corner-sharing triangles, intrinsically accommodates Dirac fermions, van-Hove singularities and flat bands, so that a variety of correlated many-body ground states can be realized. In Kagome metal AV_3Sb_5 (A = K, Rb, Cs), both charge density wave order and superconductivity (SC) have been revealed, yielding an intriguing interplay. While the CDW order is suppressed monotonically as pressure increases, a double-dome feature of T_c has been discovered, with T_c reaching a maximum near the CDW suppression point, suggesting the potential role of charge fluctuations on SC.

Here we report the unexpected emergence of a new phase in KV_3Sb_5 under pressure. The zero-field electrical resistance (not shown here) reveals an anomaly under pressure, marking a previously unidentified phase boundary $T^*(p)$, in addition to the established $T_{\mathrm{CDW}}(p)$ and $T_c(p)$, denoting the CDW and SC transition, respectively (see figure 42).

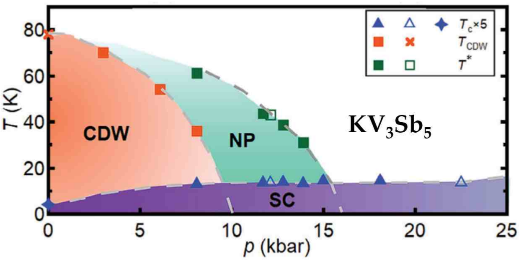

FIG. 42. *Temperature-pressure phase diagram of KV_3Sb_5 showing the charge density wave (CDW) and the superconducting (SC) phases, and the newly detected phase (NP). The T_c is multiplied by a factor 5.*

Our quantum oscillation studies up to 31 T demonstrate that the new phase does not reconstruct the Fermi surface, confirming that the translational symmetry of the pristine metallic state is preserved. Indeed, when comparing the FFT spectra in the CDW phase and beyond (within NP), the main difference (see figure 43) is the appearance under high pressure of a high frequency peak (ω), reminiscent of the large extremal orbit recently revealed in the high-pressure pristine metallic state of CsV_3Sb_5, when the CDW transition is tuned away. The CDW order introduces an in-plane superlattice modulation resulting in a larger unit cell. The reconstructed Brillouin zone areas hence are too small to host an extremal orbit corresponding to a frequency. Thus, the detection of such large frequencies is an indicator for the absence of the CDW order, and it is tempting to assign the observed 8372 T frequency in KV_3Sb_5 to the large Fermi surface of the pristine metallic state, akin to CsV_3Sb_5, even though at 12.1 kbar the $T^*(p)$-related phase is present.

The need to preserve the pristine Fermi surface in the $T^*(p)$-related phase imposes a strong constraint on the possible nature of the electronic state; nematicity is one candidate, which breaks rotational but preserves translational symmetry. The fact that $T^*(p)$ has not been observed in bulk KV_3Sb_5, but appears in our thin flakes supports this scenario, because in the bulk sample multiple nematic domains can weaken signals from experimental probes that lack spatial resolution by averaging. On our samples, not only the thickness is significantly reduced but the separation between the voltage leads is also small (10 μm), leading to the possibility of probing only a dominant nematic domain in which the nematic order parameter is uniform. In KV_3Sb_5, one can envisage a distortion of the Fermi surface from the perfect six-fold symmetry, thereby breaking the rotational symmetry, but preserving the cross-sectional area. Thus, the quantum oscillation frequency may not vary significantly.

The discovery of the new phase in KV_3Sb_5 provides a prime confirmation that the Kagome lattice is a prolific platform for realizing multiple exotic phases, and calls for complementary studies. For more details please see [Wang *et al.*, Adv. Sci. **12**, 2415012 (2025)].

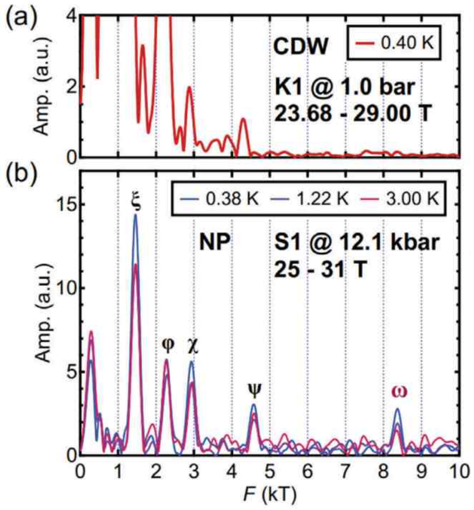

FIG. 43. *FFT spectrum of the SdH oscillation data at ambient pressure (a) from 23.68 to 29.00 T and at 12.1 kbar (b) from 25 T to 31 T. The magnetic field is always aligned along the c-axis. The main feature is the appearance of a high frequency peak under pressure at 8372 T (ω orbit).*

G. Seyfarth
Z. Wang, L. Wang, K. Yip, Y. Tsui, T. Poon, W. Wang, C. Tsang, K. Lai, W. Zhang, S. Goh (The Chinese University of Hong Kong), A. Pourret, G. Knebel (IRIG-PHELIQS, CEA Grenoble), S. Wang (Southern University Shenzhen), W. Yu (City University of Hong Kong), D. Graf (NHMFL, Tallahassee)

Magnetic Systems

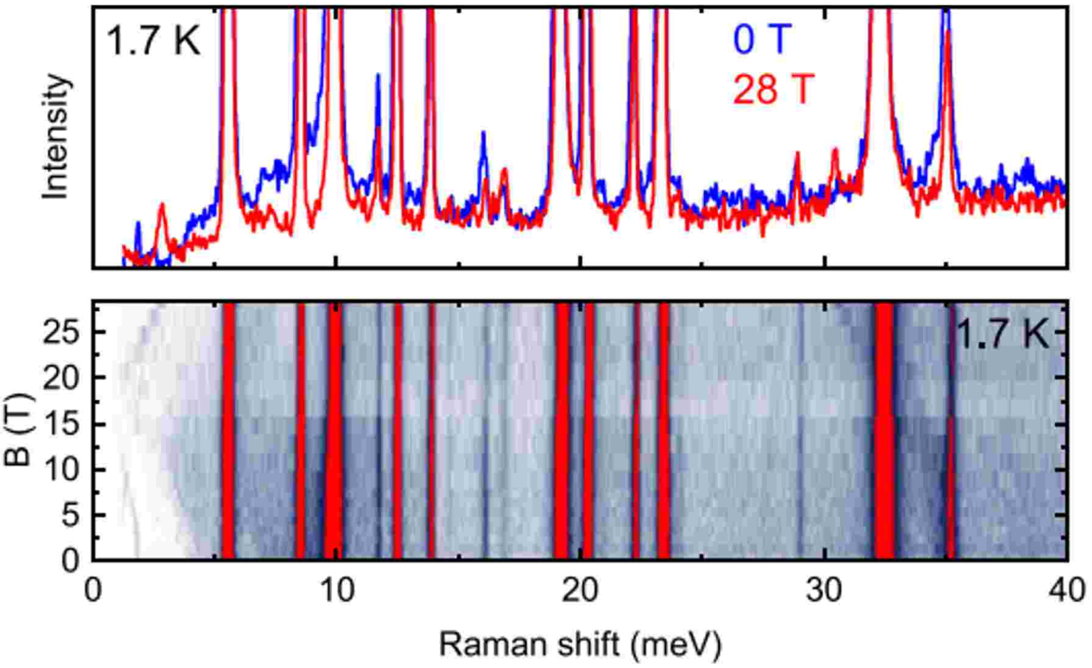

Critical Berezinskii-Kosterlitz-Thouless dynamics in the archetypal two-dimensional spin system $Ba_2CuSi_2O_6Cl_2$

One of the most remarkable properties of low-dimensional (low-D) systems is that they are characterized by a critical behaviour over their entire ungapped regime. Due to the unavoidable finite 3D coupling of their low-D elements, the corresponding quasi-1D and quasi-2D antiferromagnetic quantum spin materials exhibit a 3D-ordered low-temperature phase between the two critical magnetic fields H_{c1} and H_{c2}, which can be described in the framework of Bose-Einstein condensation (BEC). These compounds, and in particular their low-energy spin dynamics measured by the nuclear magnetic resonance (NMR) spin-lattice relaxation rate T_1^{-1} have been instrumental in defining the appropriate theoretical description.

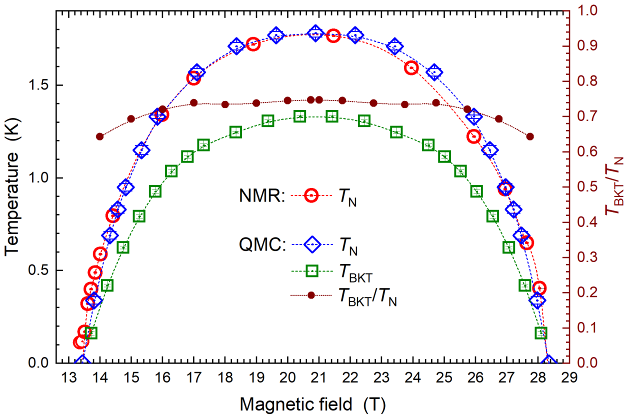

FIG. 44. *Magnetic field–temperature (H–T) phase diagram of* $Ba_2CuSi_2O_6Cl_2$ *is obtained by NMR (red circles) from the maximum of critical fluctuations at the phase transition (*T_N*), measured by the peak of the* $T_1^{-1}(T)$ *or* $T_1^{-1}(H)$ *data. It is overlapped by the theoretical fit by the QMC simulations (blue diamonds). This fit allows for the QMC determination of the corresponding, purely 2D, Berezinskii-Kosterlitz-Thouless (BKT) transition temperature* T_{BKT} *(green squares and brown dots for the* T_{BKT}/T_N *ratio).*

Using NMR, we have investigated $Ba_2CuSi_2O_6Cl_2$, a perfectly stoichiometric and structurally simple compound, which is an archetypal quasi-2D spin system having the big advantage that its critical fields are conveniently accessible: $H_{c1} = 13.4$ T and $H_{c2} = 28.4$ T for $H \parallel c$ axis. Unlike the quasi-1D system, whose spin dynamics is perfectly accounted for in the framework of Tomonaga-Luttinger liquid (TLL) description, and the 3D compounds, in which the critical spin fluctuations are strongly localized at the BEC ordering temperature T_N (within ±10-20%), quasi-2D spin compounds present strong, far-extending spin fluctuations above the BEC transition, which are not theoretically described and require state-of-the-art numerical simulations by quantum Monte Carlo (QMC) methods. Confronting our NMR T_1^{-1} data with the corresponding QMC simulations allowed us to confirm the validity of the applied theoretical spin model by unprecedented agreement between the measured and the modeled phase diagram (see figure 44), and to establish the temperature range (1.2-2.2)$\times T_N$ where the 2D-critical description is fully applicable. We could thus replace the temperature scale in the measured $T_1^{-1}(T)$ dependences by the corresponding 2D-critical correlation length $\xi_{2D}(T)$ and thus experimentally confirm the expected critical behaviour $T_1^{-1}(\xi) \propto \xi^{z-\eta}$, where $z-\eta = 1.0 \pm 0.1$ (see figure 45). While a perfect agreement is established between the experimental and the predicted T_1^{-1} at H_{c1} and H_{c2}, *i.e.*, at the quantum critical points, the QMC predictions for the critical exponents are found to be anomalously low above the BEC phase. This is probably related to the employed analytic continuation procedure.

Our results present the most comprehensive set of experimental data on the 2D-critical BKT spin dynamics, confronted with the theoretical modeling by QMC simulations [Ranjith *et al.*, preprint, arXiv:2511.17381]. We regard these data and the analysis as a benchmark that will stimulate further research in the field.

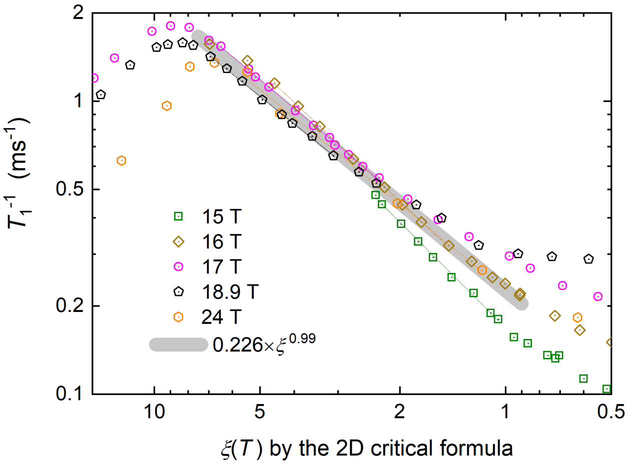

FIG. 45. *The* T_1^{-1} *data plotted versus* ξ *determined by the 2D-critical formula* $\xi_{2D}(T)$ *presents a critical and nearly field-independent behaviour in the relevant* ξ *range (*$7 > \xi > 1$*). The corresponding power-law fits are given by the thin straight lines. Thick gray line displays the average critical behaviour.*

K. M. Ranjith, S. Krämer, M. Horvatić
M. Dupont, S. Capponi, N. Laflorencie (Laboratoire de Physique Théorique, Toulouse), E. Orignac (ENS de Lyon), N. Kurita, H. Tanaka (Institute of Science Tokyo)

Field- and temperature-driven magnetic excitations in rouaite $Cu_2(OH)_3NO_3$

Quantum spin systems consisting of sublattices with distinct spin topologies, dimensionalities, and degrees of frustration in a single material bring about a rich array of exotic magnetic phases and excitations at zero magnetic field, as well as a wealth of field-induced magnetic phases. In these systems, dominant exchange interactions and their underlying geometries primarily dictate the characteristics of higher-energy excitations. Conversely, residual exchange interactions fine-tune the details of magnetic ground states, magnetic structures, and lower-energy excitations.

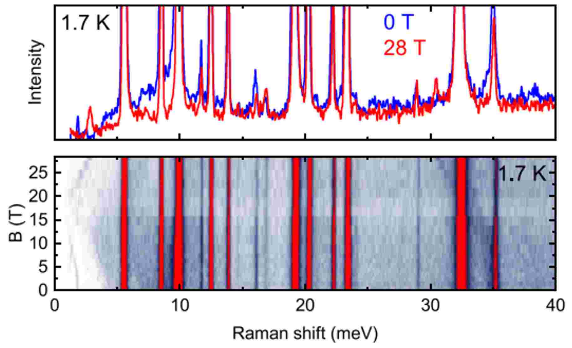

FIG. 46. *Magneto-Raman scattering response of rouaite* $Cu_2(OH)_3NO_3$. *(Top) Comparison between the 0 and 28 T Raman spectra taken at* $T = 1.7\,K$ *and (bottom) the corresponding color contour plot. All Raman spectra were collected in the unpolarized condition.*

A notable example is $SeCuO_3$, in which the simultaneous occurrence of three fundamentally different types of spin excitations-magnons, triplons, and spinons has been observed. In this compound, Cu1 sites form strong dimers, while Cu2 sites constitute a network of coupled spin chains. Another prominent example is the family of layered copper hydroxides $Cu_2(OH)_3X$ (X=halide or nitrate), in which the magnetic behavior is influenced by the species of X. The elementary magnetic motif comprises a chain of triangles with alternating antiferromagnetic (AFM) and ferromagnetic (FM) interactions. The inserted species (halide or nitrate) controls the character of in-plane and interplane interactions, providing a unique platform to study the confluence of AFM and FM chains, as well as their three-dimensional couplings. We recall that an $s = 1/2$ AFM chain has deconfined spinons as low-energy excitations, while an $s = 1/2$ FM chain features magnons.

With decreasing temperature, the magnetic susceptibility exhibits a broad maximum around 12 K, indicative of the development of short-range magnetic order. Below 12 K, a negative thermal expansion is observed, alluding to strong magnetoelastic couplings. An AFM transition occurs at about $T_{N1} \simeq 8\,\mathrm{K}$, followed by a subsequent weak transition at $T_{N2} \simeq 5\,\mathrm{K}$. It was proposed the coexistence of short-range resonating-valence-bond correlations and magnetic long-range order. In the low-temperature magnetic phase, phase I, the AFM chains exhibit FM canting along the b axis, resulting in small net magnetic moments on the Cu2 chains. These moments rotate by 90° from one chain to another, forming a commensurate cycloidal state. In the intermediate-temperature phase, phase II, the spin arrangement is helically modulated from plane to plane. When an external field is applied along a and [001], phase III is observed over a wide field range of $\mu_0 H \simeq 2 - 15\,\mathrm{T}$, in which the a or c components of the magnetic moment in every second FM chain are flipped. In contrast to the two field orientations, phase I is retained for $H \| b$ (chain direction). Upon further increasing the magnetic field, the AFM phase is suppressed around $\mu_0 H_{2/3} \simeq 15\,\mathrm{T}$, transiting into a 2/3-plateau state that corresponds to fully polarized FM chains. A further field-induced transition to a 5/6-plateau state occurs at 46-52 T. The exact nature of collective magnetic excitations in this intriguing compound remains unknown.

In this study, we employ Raman spectroscopy to probe magnetic and phonon excitations of rouaite $Cu_2(OH)_3NO_3$ as a function of field and temperature to better understand the nature of field-induced phase transitions. Our Raman scattering study first revealed several low-energy soft modes (see figure 46), indicating that a structural degradation around 425 K is driven by the release of HNO_3,H_2O,NO_2, and O_2 groups. Furthermore, these low-energy phonons exhibit significant anomalies across the transition from phase III to a 2/3-plateau phase, highlighting the role of magnetoelastic couplings. Our field- and temperature-dependent study of magnetic excitations unveiled that the plateau phase, characterized by fully polarized ferromagnetic chains, is induced by the suppression of anti-ferromagnetic ordering. The dimensional reduction in the plateau phase is manifested as the step-like decrease of the magnetic continuum excitations across at 15 T. Rouaite thus offers an exciting opportunity to explore a quantum phase transition from a magnetic solid to a Tomonaga-Luttinger liquid within an accessible field range.

More details concerning this work can be found in [Wulferding *et al.*, Phys. Rev. B **111**, 064409 (2025)].

A. Pawbake, C. Faugeras
D. Wulferding (Sejong University, Seoul), S.S. Islam, Y. Choi, G. Ban, S. Lee, K-Y. Choi (Sungkyunkwan University, Suwon)

Spin-orbital-lattice coupling and the phonon Zeeman effect in the Dirac honeycomb magnet $CoTiO_3$

Quasiparticles, which encompass dressed elementary particles (*i.e.*, electrons), composite objects (Cooper pairs), and collective excitations (phonons, magnons), are of fundamental interest in condensed matter physics. Energy, linear momentum, and their unique inter-relationship, the so-called dispersion relation, characterize such quasiparticles. When the symmetry of a crystal allows it, quasiparticles can interact with each other and create hybrid modes whose wave functions inherit properties of the parent quasiparticles. An example of this hybridization is the interaction between photons and polar phonons in insulators. This hybridization can be seen most clearly near avoided crossings of the hybridized modes as a parameter of the system such as momentum, magnetic field, or temperature is varied.

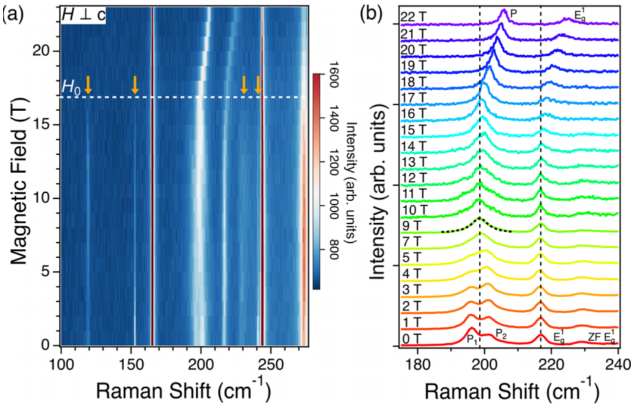

FIG. 47. *High-magnetic-field behavior. a) False color Raman scattering intensity map at 5 K as a function of magnetic field applied perpendicular to the c axis. Zone-folded phonons marked by arrows disappear above the critical field H_0. (b) The same data as in (a), but now focused in the region of P1, P2, and Eg1. The black dashed line at 9 T shows the fit to a single mode P with Lorentzian line shape, the merged P1 and P2 spin orbiton. Above H_0, both P and E_g^1 shift with magnetic field. Dashed vertical lines mark the positions of P and E_g^1 at 9 T.*

Magnetically ordered materials offer a fertile ground for the observation of hybridization between quasiparticles that such systems can host. In insulating materials, magnetic order typically occurs because of the interaction between pure atomic spins with their neighbors. However, it is also possible that the atomic magnetic degrees of freedom that are not of pure spin origin, such as orbital angular momentum, play a role in the magnetic behavior as well. This interplay originates from the electric field generated by the atoms surrounding the magnetic atom, usually called crystal electric field (CEF), and its effect on the electronic energy levels of the atoms in the unit cell of the material. The combination of the CEF, spin-orbit coupling (SOC), small structural distortions, and the interactions between atoms can produce a series of energy levels that must be considered to explain all of the magnetic properties of a material. A recent example of this behavior is $CoTiO_3$, where both magnons and these higher energy spin-orbital states have been found to have dispersion in momentum space and are required to explain many magnetic properties. These spin-orbital states are sometimes called spin-orbit excitons or spin orbitons because they are true quasiparticles with specific energy versus momentum dispersion relations.

In this study, we present a detailed temperature and magnetic-field dependent Raman scattering study and the magnetic field dependence of the infrared spectra to probe the coupling between phonons and spin orbitons in $CoTiO_3$ (figure 47). We provide clear evidence of the hybridization of spin orbitons and a zone center, doubly degenerate E_g phonon via the phonon Zeeman effect measured using magneto-Raman scattering. On the other hand, the infrared active, zone-center phonons did not show any splitting in magnetic field. We also find several phonons that result from the Brillouin zone folding in the magnetically ordered state. Surprisingly, a zone-folded phonon also exhibits the behavior of the phonon-Zeeman effect, thus highlighting the significant coupling between the lattice and the spin orbitons. We report three principal effects: (1) the appearance below T_{Neel} of five zone-folded phonons and their disappearance above H_0 perpendicular to the c axis; (2) observation of the hybridization between two spin orbitons with a nearby phonon with E_g symmetry, giving rise to its Zeeman effect; and (3) the hybridization between an inversion-odd Eu phonon and an additional spin orbiton measured in the infrared spectra in magnetic field also applied along the c axis. While the model that explains the magnon behavior can explain many of the experimental results, it does not do so exactly. This highlights the need to further develop the microscopic theory of the coupling between the spin, orbital, and lattice degrees of freedom in $CoTiO_3$.

More details concerning this work can be found in [Mai *et al.*, Phys. Rev. B **111**, 104419 (2025)].

F. Le Mardele, A. Pawbake, M. Orlita, C. Faugeras
T.T. Mai, K.F. Garrity, R.L. Dally, T. Adel, M. F. Muñoz, J. R. Simpson, A. R. Hight Walker (NIST, Gaithersburg), Y. Li, A. Giovannone, C. Lyon, R. Valdés Aguilar (The Ohio State University, Columbus), D. Shaw, T. DeLazzer, K. Ross (Colorado State University, Fort Collins)

Generation of a nodal line and Weyl points by magnetization reorientation in $Co_3Sn_2S_2$

The interplay between magnetism and topology may fundamentally shape the electronic band structure through symmetries dictated by the magnetic order. This coupling can enable magnetic field control of topological states, which is particularly appealing for applications in spintronics and quantum information technology. Despite the numerous theoretical proposals, experimental demonstrations of such external field control of band topology are scarce.

In this study we demonstrate the magnetic field control of the topological band structure in the emblematic magnetic Weyl semimetal $Co_3Sn_2S_2$. Ab initio calculations predicted nodal loops close to the Fermi energy in the zero spin-orbit coupling limit. Below the Curie temperature $T_c = 177\,\mathrm{K}$, a ferromagnetic moment perpendicular to the kagome planes of $Co_3Sn_2S_2$ develops, and the spin-orbit coupling opens a gap along the nodal loops except in two Weyl points on each. We have tested whether in-plane magnetic fields, forcing the magnetization to the plane, can alter the band structure or not.

The magnetic field-induced changes in the electronic structure were probed using magneto-optical spectroscopy. The measured changes of the infrared reflectivity up to 34 T can be seen in figure 48(a) and (c). To interpret the magnetic field-induced changes, the calculated the field dependence of the optical conductivity for the two orthogonal in-plane field directions is plotted in figure 48(b) and (d)). The most prominent features are the tail of the Drude response dominating the spectra below 15 meV and a peak around 29 meV, which shifts to smaller energies at higher fields. The position of the latter as a function of the field is shown in the respective inset. It follows the same trend as the magnetization for both in-plane field directions, although the magnitude of the shift is larger for $B \parallel a$. As demonstrated earlier [Schilberth *et al.*, Phys. Rev. B **107**, 214441 (2023)], this peak is caused by transitions between bands associated with the partially gapped nodal lines, which can be excited almost exclusively by one of the two circular polarization states of light.

We have calculated the band structure and the optical conductivity spectrum for in-plane magnetization directions. The theory reproduces the experimental features on a broad energy scale. The shift of the nodal line resonance is captured well, although the peak in the theory spectra is not as pronounced as in the experiment. To evaluate the origin of the peak shift, we directly compared the band structures for the in-and out-of-plane configurations and identified that k-space regions around the nodal loops contribute the most to the optical conductivity. The spin-orbit gap is reduced as the dominant spin-orbit matrix element vanishes for in-plane spin orientation. Moreover, this material-specific theory shows the emergence of a completely degenerate nodal line for $B \parallel a$.

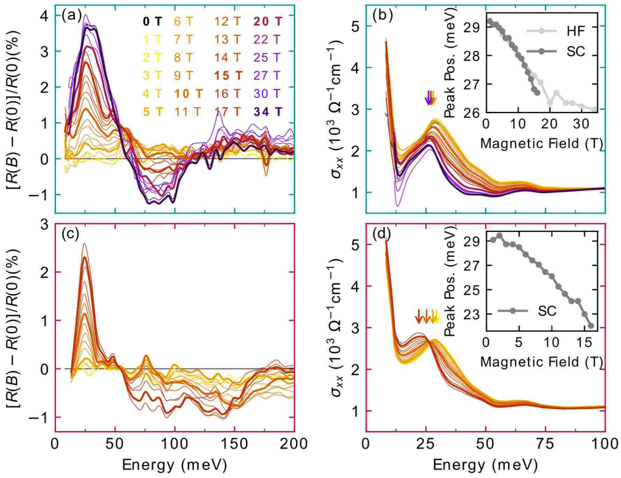

FIG. 48. *(a), (c) Magnetic field dependence of the infrared reflectivity in $Co_3Sn_2S_2$ for $B \perp a$ and $B \parallel a$, respectively. (b), (d) Optical conductivity spectrum in $Co_3Sn_2S_2$ for $B \perp a$ and $B \parallel a$, respectively. The insets show the field evolution of the peak position corresponding to the resonant excitation of the nodal loop gapped by the spin-orbit coupling.*

Compared to quantum oscillation or STM measurements, the direct access to the interband response highlights the unique capabilities of optical spectroscopy to monitor changes in the band structure and its quantum geometry. As the dimension of the degenerate manifolds increases from Weyl points for $B \perp a$ to loops for $B \parallel a$, there is an enhancement of the Hall response and reconstruction of the Hall spectral weight. Following the changes in the topology of the bulk band structure, surface states may also be restructured. Since the nodal loop remains intact for $B \parallel a$, drumhead surface states may be formed on the surface, instead of the Fermi arcs present between the isolated Weyl points. The magnetization reorientation, therefore, provides an exciting pathway to study these exotic surface states, also applicable to other materials.

For more details please see [Schilberth *et al.*, npj Quantum Materials **10**, 67 (2025)].

F. Le Mardelé, I. Mohelsky, M. Orlita
F. Schilberth, I. Kézsmárki (University of Augsburg), M.-C. Jiang, R. Arita (RIKEN-CEMS, Saitama), M. A. Kassem, Y. Tabata, T. Waki, H. Nakamura (Kyoto University), L. B. Papp, S. Bordács (Budapest University of Technology and Economics)

Antiferromagnetic resonance in hexagonal MnTe

Amongst the well-known collinear antiferromagnets MnTe now stands at a priviledged position. The recently discussed properties connected with the broken PT symmetry of the system, bring a surge of interest in this compound, particularly α-MnTe. α-MnTe grows in the NiAs-type polymorph with Mn^{2+} moments aligned in the hexagonal plane. The alignment is governed by strong out-of-plane component of the single-ion anisotropy with only a minor contribution from the in-plane triple axis.

To disentangle the different effects of symmetries on electronic and magnonic bands, the bulk properties of the MnTe must be well established. The previous experiments reporting on magnons in MnTe used inelastic neutron scattering (INS), see *e.g.* [Liu *et al.*, Phys. Rev. Lett. **133**, 156702 (2024)] and Raman scattering spectroscopy [Zhang *et al.* Journal of Raman Spectroscopy, **51(8)**, 1383 (2020)]. The latter approach only observed 2-magnon scattering and there is no further report of the $k = 0$ magnon mode in MnTe observed via optical methods.

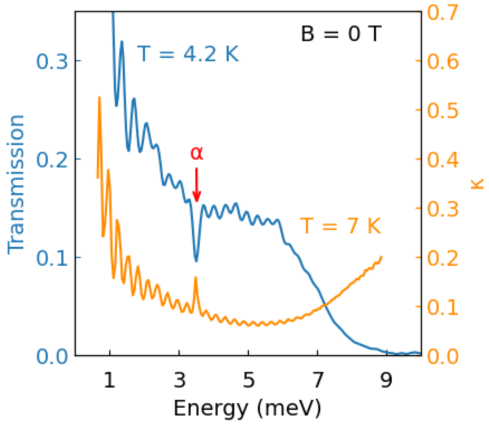

FIG. 49. *Low-temperature THz transmission spectrum of the bulk* α*-MnTe layer with the thickness of* $d = 0.4$ *mm, measured using the frequency-domain Fourier-transform technique, compared with the extinction coefficient* κ *obtained using the time-domain THz spectroscopy. The vertical arrow indicates the energy of a magnetic excitation identified as the* α *mode of antiferromagnetic resonance in this work.*

Here we present a combined theoretical and experimental study of antiferromagnetic resonance in α-MnTe. We profit from a relatively high spectral resolution of optical techniques and obtained a more precise estimate of the single-ion magnetic anisotropy as compared to INS.

The sample presented in this report was synthesized by self-flux technique from pure manganese and telurium. The far-infrared/THz response of MnTe at low temperatures is displayed in figure 49. In the narrow transmission window, a single absorption mode is clearly visible. We associate this mode with the upper branch of the non-degenerate magnon mode at Γ point of the Brillouin zone observed in the INS experiment. The magneto-transmission data in figure 50 shows the evolution of the observed mode with the magnetic field applied perpendicularly to the hexagonal plane, *i.e.* along the hard axis of MnTe.

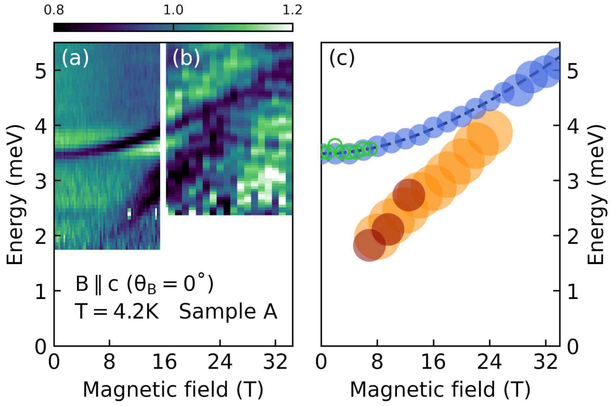

FIG. 50. *A color map of magneto-transmission at liquid helium temperature using (a) superconducting and (b) resistive coils, with the magnetic field perpendicular to the hexagonal plane of MnTe. The magneto-transmission* T_B *is normalized by the transmission averaged over the whole field range. The extracted positions of resonances with a step of 2 T are plotted as blue circles in (c), complemented with data obtained by the time-domain THz and ESR techniques (green and red circles, respectively). The size of the circles corresponds to the error bar. The dashed line represents a LSWT model of antiferromagnetic resonance energy.*

A simple model based on the linear spin wave theory well reproduces the observed dependence (dashed line in figure 50). We conclude that the upper magnon mode can be well theoretically modelled without considering the impact of the in-plane component of the single-ion anisotropy. This confirms dominantly easy-plane character of the antiferromagnetic ordering in hexagonal MnTe. The out-of-plane component of the single-ion anisotropy is evaluated as $D = (40 \pm 10)\,\mu$eV.

For more details please see [Dzian *et al.* Physical Review B, **112(2)**, 024433 (2025)].

J. Dzian, F. Le Mardelé, A.-L. Barra, C. Faugeras, M. Orlita
P. Kubaščík, S. Tázlarů, J. Volný, K. Uhlířová, L. Nádvorník, M. Veis (Charles University, Prague), M. Šindler, C. Kadlec, F. Kadlec, J. Hejtmánek, R. Tesař, J. Železný, K. Výborný (Czech Academy of Science, Prague), K. P. Kluczyk, M. Gryglas-Borysiewicz (University of Warsaw), A. Mycielski, P. Skupiński (Polish Academy of Sciences, Warsaw), M. Białek, (Institute of High Pressure Physics, Warsaw)

Anisotropic collapse of electronic correlations in the ferromagnet UGe_2 under high magnetic field

The interest for U-based ferromagnets was renewed by the proposition that the superconductor UTe_2 may be a nearly ferromagnet with ferromagnetic fluctuations responsible for triplet superconductivity. Later, UTe_2 was proved to undergo long-range antiferromagnetic order under pressure and to be a nearly antiferromagnet at ambient pressure Knafo *et al.*, Phys. Rev. X **15**, 021075 (2025)]. This highlighted the difficulty in determining the nature of electronic correlations using non-wavevector-resolved experimental probes.

We also noted that a systematic study of a reference U-based ferromagnet under wide ranges of temperatures and intense magnetic fields of different directions has never been performed. This motivated us to investigate UGe_2, a textbook U-based ferromagnet with the Curie temperature $T_C \simeq 52$ K and an ordered moment $\mu_m \simeq 1.4\ \mu_B$/U.

In this material, superconductivity emerges within the ferromagnetic state under applied pressure and was proposed to result from triplet mechanism. Within the ferromagnetic phase, electronic correlations were also found to drive broad anomalies in various physical quantities at the temperature $T^* \simeq 30$ K.

We report here electrical-resistivity measurements on UGe_2 under pulsed magnetic field up to 60 T. An anisotropic field-induced suppression of the electronic correlations is revealed. The electrical resistivity strongly decreases when a magnetic field $\mathbf{H}$ is applied along the easy magnetic axis $\mathbf{a}$, while it remains almost unchanged when $\mathbf{H}$ is applied along the hard magnetic axes $\mathbf{b}$ and $\mathbf{c}$.

The field-induced destabilization of the ferromagnetic state is also anisotropic: the anomaly at the Curie temperature T_C disappears in fields higher than $\gtrsim 1$ T for $\mathbf{H} \parallel \mathbf{a}$ and in fields higher than $\gtrsim 20$ T for $\mathbf{H} \parallel \mathbf{b}, \mathbf{c}$. At temperatures below 2 K, we observe quantum oscillations in fields larger than 50 T applied along $\mathbf{b}$, which support the presence of a two-dimensional Fermi surface similar to that previously observed at low fields.

For more details please see [Somesh *et al.*, arXiv:2510.19404 (2025)].

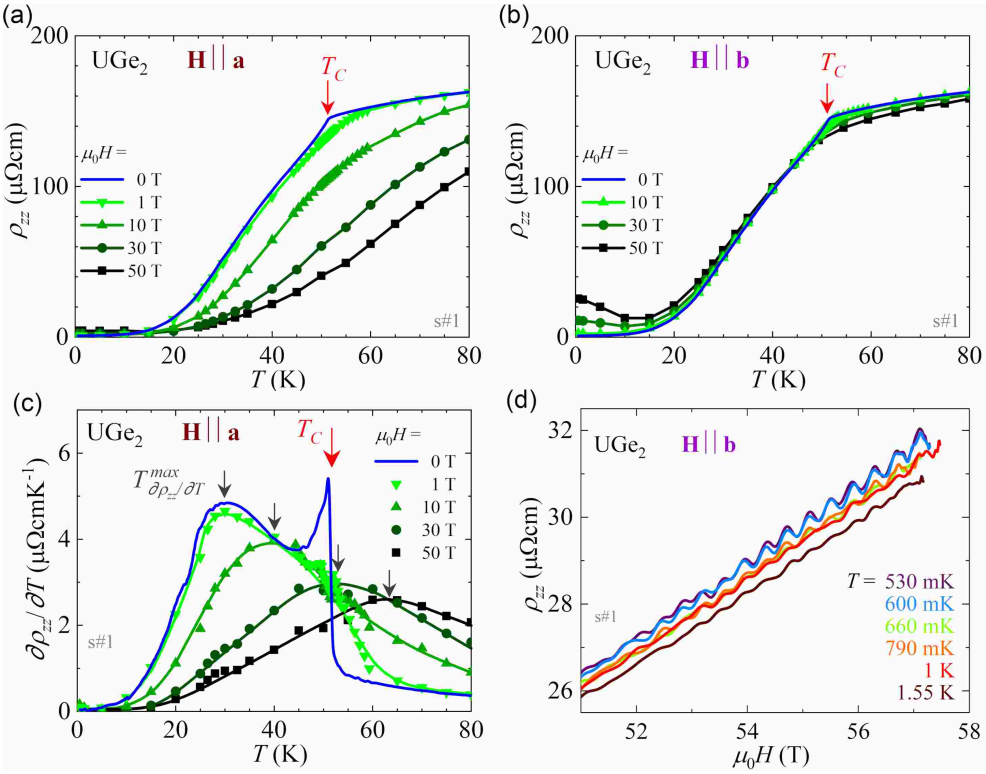

FIG. 51. Temperature dependence of the electrical resistivity ρ_{zz} at constant magnetic fields (a) $\mu_0\mathbf{H} \parallel \mathbf{a}$ and (b) $\mu_0\mathbf{H} \parallel \mathbf{b}$ up to 50 T. (c) Temperature dependance of $\partial\rho_{zz}/\partial T$ at constant magnetic fields $\mu_0\mathbf{H} \parallel \mathbf{a}$ up to 50 T. (d) Shubnikov-de-Haas quantum oscillations in ρ_{zz} versus H at temperatures from 500 mK to 1.55 K under a magnetic field $\mu_0\mathbf{H} \parallel \mathbf{b}$ from 51 to 57.5 T.

K. Somesh, T. Thebault, F. Duc, W. Knafo
V. Taufour, G. Knebel, D. Braithwaite (University Grenoble Alpes, CEA, Grenoble), D. Aoki (Institute for Materials Research, Tohoku University, Ikaraki)

Biology and Molecular Magnetism

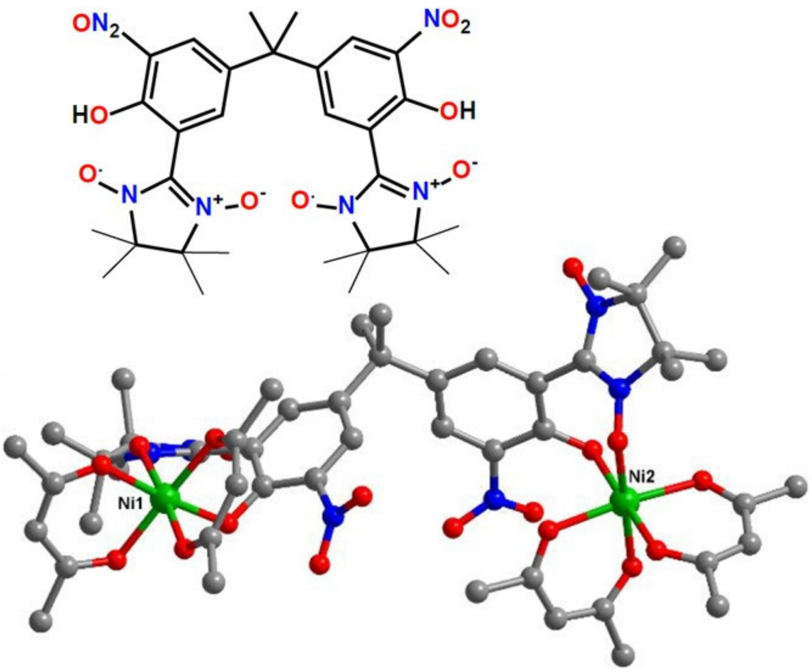

A new synthetic pathway to nitronyl-nitroxide biradical complexes

A new nitronyl-nitroxide biradical, H_2L, has been obtained starting from bisfenol A, through successive nitration, formylation, and Ullman reactions (figure 52(a)). Using this molecule as a ligand, two isostructural binuclear complexes. $(Et_3NH)_2[Co_2L(hfac)_4]\cdot CHCl_3$ (**1**) and $(Et_3NH)_2[Ni_2L(hfac)_4]\cdot CHCl_3$ (**2**), have been synthesized and characterized by single crystal X-Ray diffraction. The crystal structure of 2 consists of anionic dinuclear species, $[Ni_2L(hfac)_4]^{2-}$, triethylammonium cations, Et_3NH^+ (figure 52(b)). Each nickel(II) ion shows an octahedral geometry, being coordinated by four oxygen atoms from the hexafluoroacetylacetonato (hfac-) ligands, and in *cis* positions by the phenoxido and aminoxyl oxygen atoms from the paramagnetic ligand. The two crystallographically independent metal ions are chiral and display D (Ni**1**) and, respectively, L (Ni**2**) configurations.

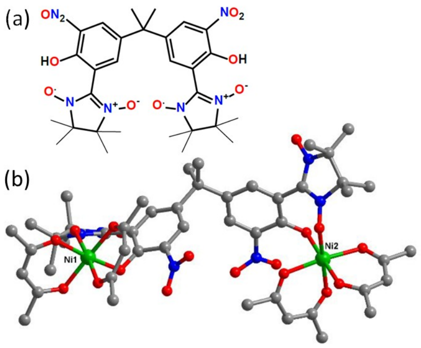

FIG. 52. *(a) The nitronyl-nitroxide ligand H_2L. (b) The X-ray structure of the complex anion **2**, with nickel (green), carbon (grey), oxygen (red), nitrogen (blue) and chlorine (yellow).*

Magnetic measurements suggests that the Co^{II} ion and the radical are coupled even at room temperature. Upon lowering the temperature, $\chi_M T$ decreases slowly to $3.98\,cm^3mol^{-1}\,K$ (100 K), than more and more, reaching $0.41\,cm^3mol^{-1}\,K$ at 2 K. This behavior originates from the magnetic anisotropy of the Co^{II} ion combined with the antiferromagnetic interaction between each cobalt ion and the radical moiety. The magnetization versus H/T curves do not reach saturation, in agreement with the temperature dependence of the $\chi_M T$ product. The experimental data was fitted using the following Hamiltonian,

$$\begin{aligned}\hat{H} = &-2J\hat{S}_1\hat{S}_2 + \mu_B\vec{B}(\alpha\hat{L} + g_1\hat{S}_1 + g_2\hat{S}_2) + \alpha\hat{L}\hat{S}_1\cdot\lambda \\ &+ \alpha^2 B_2^0(3\hat{L}_z^2 - \hat{L}^2) + \tfrac{1}{2}\alpha^2\hat{B}_2^2(\hat{L}_+^2 - \hat{L}_-^2).\end{aligned}$$

The parameters are defined as follows, $\alpha = -(3/2)k$ is the orbital reduction factor, $k = 1$ accounts for the covalency contribution; $S_1 = 3/2$ and $S_2 = 1/2$ corresponds to the spin of Co^{II} and the radical respectively; $L = 1$, effective orbital triplet quantum number for Co^{II}; electron g-factor $g_1 = g_2 = 2.0$; $\lambda = -170\,cm^{-1}$ is the spin-orbit coupling constant. The fit yielded the following optimized parameters, $B_2^0 = 515 \pm 5\ cm^{-1}$ is axial distortion factor which represent energy between, ${}^4A_{2g}$ and ${}^4E_g$; $B_2^2 = -7.85 \pm 53$ represent the rhombohedral distortion and can be assignment to splitting of ${}^4E_g$ levels; $J = -16.5 \pm 0.5\,cm^{-1}$ is the Co^{II}-radical magnetic interaction. In the case of nickel compound the antiferromagnetic interaction was machi stronher. The experimental data were analyzed using the Hamiltonian,

$$\begin{aligned}\hat{H} = &-2J\hat{S}_1\hat{S}_2 + \mu_B\vec{B}(g_1\hat{S}_1 + g_2\hat{S}_2) \\ &+ D_1(\hat{S}_{1,z}^2 - \tfrac{1}{3}S_1(S_1+1)) + E_1(\hat{S}_{1,x}^2 - \hat{S}_{1,y}^2),\end{aligned}$$

where $S_1 = 1$, $S_2 = 1/2$, $g_2 = 2.0$. The resulting best fit parameters are $g_1 = 2.34 \pm 0.01$, $D_1 = 7.7 \pm 1.6\ cm^{-1}$, $|E_1| = 0.27\,cm^{-1}$ and $J = -147.4 \pm 0.3\,cm^{-1}$. The magnetization versus field curves are represented in figure 53. At 2 K, the magnetization reaches the expected value for saturation, taking into account that the g value for Ni^{II} is 2.34, according to the fit to the $\chi_M T$ versus T data. For more details please see [Spinu et al., CrystEngComm. **27**, 6462 (2025)].

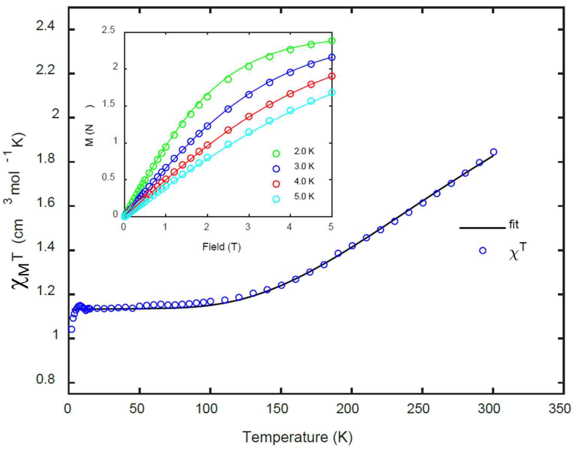

FIG. 53. *$\chi_M T$ versus temperature, and magnetization M versus applied field for compound **2** (Ni).*

G. Novitchi

C.A. Spinu, M. Hillebrand, A. M. Andruh (Faculty of Chemistry, University of Bucharest) T. Mocanu, G. Ionita, (Institute of Physical Chemistry, Romanian Academy) A. Hanganu, V. Tecueanu, M. Andruh (Institute of Organic and Supramolecular Chemistry, Romanian Academy)

EPR study of the clock transition in a mononuclear Ni(II) complex

Coordination complexes appears to be good spin qubits candidates in the solid state, as their structures and electronic properties can be largely modified by chemical design. However, even when diluted in diamagnetic hosts to reduce decoherence due to dipolar magnetic interactions, ensembles of such molecules suffer from the presence of fluctuating nuclear magnetic spins which also lead to decoherence (spectral diffusion). A way to increase the coherence time relies on the use of the clock transition (CT) which minimizes the effect of magnetic fluctuations of the spin bath (figure 54). Ni(II) complexes with an integer spin S=1 and a negative axial zero-field splitting D may exhibit a CT at zero magnetic field, provided they possess a non-zero transverse anisotropy E, the Hamiltonian is then,

$$H = \mu_B \mathbf{S}.\mathbf{g}.\mathbf{B} + D(S_z^2 - S(S+1)/3) + E(S_x^2 - S_y^2),$$

where μ_B is the Bohr magneton and $\mathbf{g}$ the Landé matrix. For $D < 0$, M_S=0 is an excited level while the two lowest spin levels are $\psi_\pm = 1/\sqrt{2}(|+1> \pm |-1>)$. They have an energy gap of $2E$ and can play the role of a qbit in zero field. In order to address the qbit, the radiation of the EPR spectrometer must match the $2E$ value.

The M(II) family of complexes of formula [M(HIM2-py)$_2$(NO$_3$)](NO$_3$), where HIM2-py is the bidentate 2-(2-pyridyl)-4,4,5,5-tetramethyl-4,5-dihydro-1H-imidazolyl-1-hydroxy, and M = Ni (**1**), Co (**2**) and Zn (**3**) (figure 54a) have isomorphous structures allowing the synthesis of solid solution materials, especially diluted solutions of **1** in **3**.

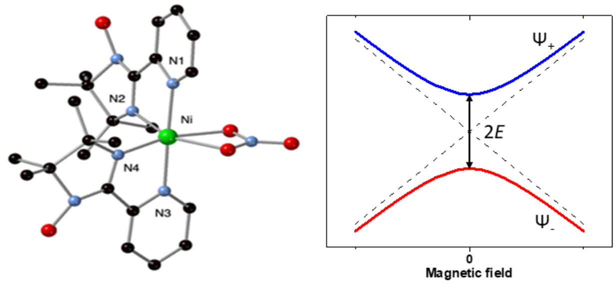

FIG. 54. *(a) Structure of [Ni(HIM2-py)$_2$(NO$_3$)]$^+$, with H atoms removed. (b) Clock Transition scheme for a spin S=1 described by the Hamiltonian above.*

A High-Field EPR (HF-EPR) study was performed on a sample with **1**:**3** = 7% (noted $\mathbf{1}_{07}$). Experimental powder spectra were recorded at 5 and 15 K for several frequencies. The spectra exhibit more signals than expected for a simple $S = 1$ system, indicating that molecules with different anisotropies are present (figure 55). The analysis of the spectra points out to the existence of a non-gaussian distribution of anisotropies, with a camel-back shape. The two maxima of the distribution are reproduced with two sets of parameters: $D_1 = -10.312(31)\,\mathrm{cm}^{-1}$, $E_1 = 0.392(16)\,\mathrm{cm}^{-1}$, $g_{x1} = 2.175(6)$, $g_{y1} = 2.149(8)$ and $g_{z1} = 2.15(5)$; and $D_2 = D_1$, $E_2 = 0.1\,\mathrm{cm}^{-1}$, $g_{x2} = g_{x1}$, $g_{y2} = g_{y1}$ and $g_{z2} = 2.2$ with a population ratio of 2:1. Thus, there are necessarily molecules presenting a gap equal to the X-band frequency.

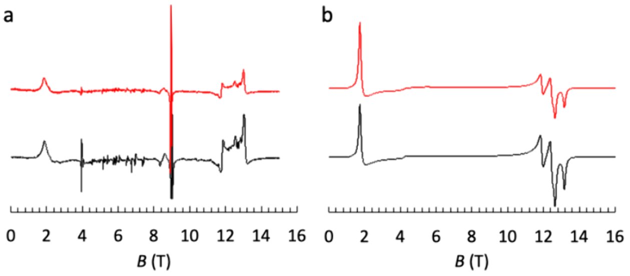

FIG. 55. *(a) Experimental 255.36 GHz powder EPR spectra of $\mathbf{1}_{07}$ at 5 (black) and 15 (red) K. Thin lines at 4 T and 9 T comes from solid O$_2$ and from a S=1/2 impurity. (b) Calculated 255.36 GHz powder EPR spectra of $\mathbf{1}_{07}$ at 5 (black) and 15 (red) K.*

The study of **1** at the CT was performed at X-band. First, echo detected field sweep (EDFS) spectra were recorded on the more diluted sample $\mathbf{1}_{01}$, showing the presence of a resonance near zero field. Then X-band pulsed EPR measurements were performed to determine the relaxation times for $\mathbf{1}_{01}$, as a function of magnetic field up to 200 G. The spin-spin relaxation time T_2 is found constant and maximum up to 20 G (with a value slightly lower than 400 ns), and then decreasing rapidly with the increase of the magnetic field; this is the behaviour expected for a CT at zero field. The protecting property of the CT resulting of rhombic anisotropy was further checked by the study of a mixed dilution sample involving both Ni (1%) and Co (5%), noted $\mathbf{1}_{01}\mathbf{2}_{05}$. Even with the addition of the fluctuating Co spins, the behaviour of the Ni T_2 remains the same and with comparable values.

For more details, please see [Tlemsani *et al.*, J. Am. Chem. Soc. **147**, 4685 (2025)].

A.L. Barra
I. Tlemsani, F. Lambert, C. Herrero, R. Guillot, T. Mallah (ICMMO, University Paris-Saclay, Orsay), N. Suaud (IRSAMC, University of Toulouse), S. Gambarelli (SyMMES, CEA, Grenoble)

Enantioselective magneto-chiral photochemistry rediscovered

Enantioselective magneto-chiral photochemistry (MChPh), which represents the ability of an unpolarized light beam k applied along a magnetic field B to produce an enantiomeric excess, was experimentally demonstrated for the first time 25 years ago. Despite the relevance that this effect can have for the origin of molecular homochirality, no other experiment has been reported in the literature since then.

With the aim of reexploring this enantioselective photochemical reactivity and quantitatively determining the enantiomeric excess achievable through MChPh as a function of the applied magnetic field and the laser irradiation wavelength, we have conducted new magneto-chiral dichroism (MChD) studies and MChPh experiments on potassium tris(oxalato)chromate(III). We have irradiated a racemic mixture of enantiomers in solution ($T = 5°\mathrm{C}$) at $\lambda = 695.5\,\mathrm{nm}$ ($500\,\mathrm{mW}$), the wavelength where MChD is maximum, with magnetic fields of up to 30 T. By irradiating the racemic mixture in these conditions for 30 min under a magnetic field $B = 30\,\mathrm{T}$, an enantiomeric excess of around 0.50% has been obtained. By changing the relative orientation of B and k, an enantiomeric excess of the same magnitude but opposite sign was obtained as predicted by the MChD theory.

Wavelength-dependent MChD and MChPh studies showed that the obtained enantiomeric excess by MChPh is intimately related in magnitude and sign to the MChD of the chromophore. Magnetic field dependent studies up to 30 T showed that the induced enantiomeric excess varies linearly with the magnetic field without any sign of saturation owing to the Zeeman splitting of the involved electronic states at the origin of the corresponding MChD signal (figure 56). Furthermore, we have conducted similar experiments with circularly polarized light (circularly polarized photochemistry (CPPh)) the most accredited mechanism at the origin of molecular homochirality, to compare the obtained enantiomeric excess. Indeed, enantiomeric excess of the same order of magnitude have been obtained by targeting different electronic transitions.

The results of this study demonstrate that by a careful choice of the irradiation wavelength, hence of the involved electronic transition, MChPh can provide an enantiomeric excess of the same order of magnitude of CPPh. It should be highlighted that our CPPh experiments have been performed with a degree of circular polarization > 95% and cannot yield a higher enantiomeric excess. On the contrary, the linear response of MChPh with the intensity of the applied magnetic field B shows that a higher enantiomeric excess should be obtained under higher magnetic fields, reinforcing the relevance of MChPh as one of the potential mechanisms at the origin of molecular homochirality.

For more details please see [Raju *et al.* ACS Central Science **11**, 1147 (2025)].

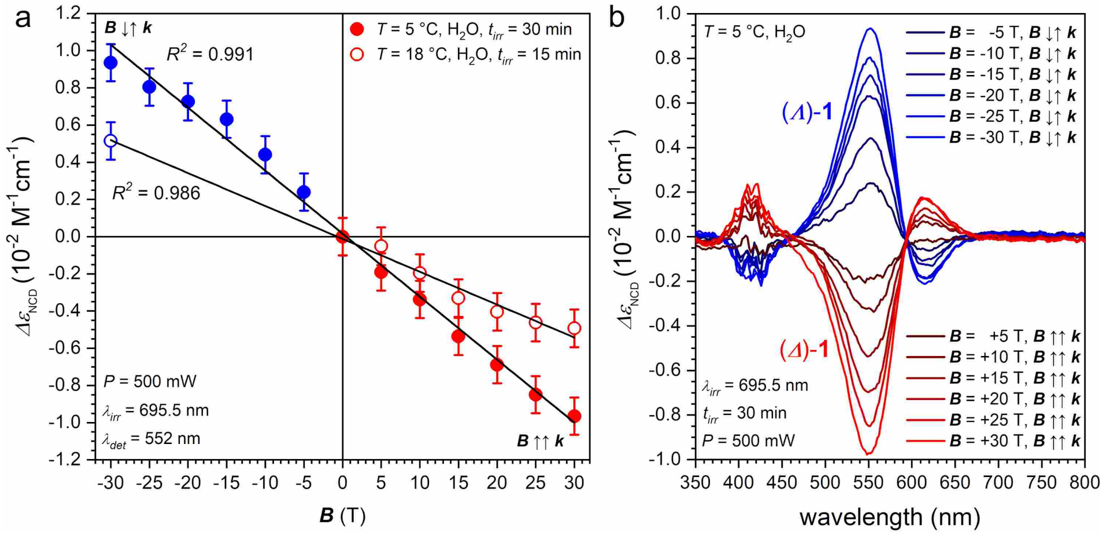

FIG. 56. *Magnetic field dependence of the induced* $\Delta\varepsilon_{NCD}$ ($\lambda = 552\,\mathrm{nm}$) *through MChPh experiments performed at* $T = 5.0$ *and* $18°C$ *at magnetic fields* B *up to* $30\,\mathrm{T}$ *parallel and antiparallel applied with respect to the laser beam* k ($\lambda = 695.5\,\mathrm{nm}$). *(b) Wide range* ($350 - 800\,\mathrm{nm}$) *NCD spectra obtained for each experiment.*

M. S. Raju, M. Aragon-Alberti, K. Cardenas, I. Breslavetz, G.L.J.A. Rikken, C. Train, M. Atzori

Magneto-chiral dichroism at the nanoscale

The interplay between magnetism and chirality within a single material gives rise to fascinating manifestations of the light-matter interaction. Among these, effects that are independent of the polarization state of the incident light hold particular technological promise. Unpolarized light, which can be easily transmitted using optical fibers without requiring polarization generators or polarization-sensitive detectors, simplifies device complexity.

In this context, magneto-chiral anisotropy (MChA) in light absorption, referred to as magneto-chiral dichroism (MChD) has recently emerged as an effective tool for reading magnetic memories stored in chiral single-molecule magnets, the smallest known molecular objects capable of retaining magnetization. However, so far this phenomenon has been mainly observed in single-crystals of molecular systems, which are not the most suitable objects for memory devices. To overcome this limitation, we direct our attention to chiral inorganic magnetic nanomaterials.

In this study we have prepared 3 nm diameter cobalt(II)-based magnetic nanoparticles in the presence of enantiopure (*D* or *L*)-aspartic acid. These NPs have been comprehensively structurally, morphologically and spectroscopically characterized, by using a multitechnique approach to assess their dimension, shape, composition, structure and magnetic response. The chiral ligands coordinate the Co^{2+} ions at the nanoparticle surface inducing a strong natural circular dichroism ($g_{NCD} = 10^{-2}$) for the $^4\mathrm{T}_1(^4\mathrm{P}) \leftarrow {}^4\mathrm{T}_1(^4\mathrm{F})$ electronic transitions of the Co^{2+} ion in octahedral sites.

Magneto-chiral dichroism measurements reveal an unambiguous MChD signal at low temperatures for the same transitions (figure 57). The B and T dependence of the MChD signals indicates that MChD C-terms dominate at low temperatures, as expected for the predominant paramagnetic nature of the investigated system.

To the best of our knowledge, these results represent the first observation of MChD in chiral-functionalized NPs, thus opening alternative perspectives for further studies on MChD in chiral functionalized inorganic nanomaterials. Such materials hold potential for polarization-independent applications in magnetic sensing, optical devices, and biomedical fields.

For more details please refer to [de Souza Lima Mendes *et al.* ACS Materials Lett. **7**, 3853 (2025)].

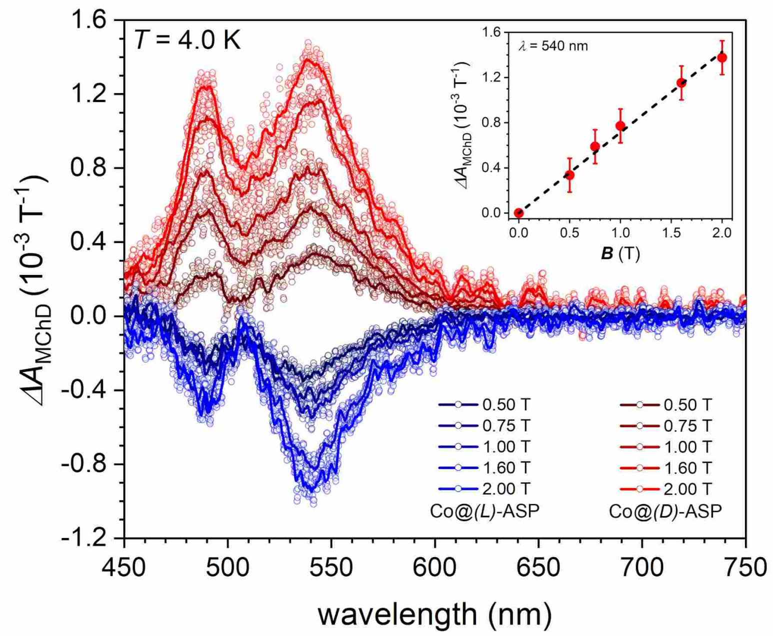

FIG. 57. *Magnetic field dependence of the MChD spectra for the Co@(D)-ASP (red) and Co@(L)-ASP (blue) NPs at* $T = 4.0\,\mathrm{K}$*. The solid lines are smoothed functions of the experimental data(empty dots). The inset shows the magnetic field dependence of the signal at* $\lambda = 540\,\mathrm{nm}$ *for Co@(D)-ASP. The difference in the signal intensity between the two enantiomers is correlated to the different sample thickness.*

L.C. Adi, C. Train, G.L.J.A. Rikken, M. Atzori

M. de Souza Lima Mendes, G. Duroux, A. Boudier, P. Pranee, M. Dosantos Blanco, J. Wang, C. Labrugère-Sarroste, E. Lebraud, S. Nlate, R. Oda, P. Rosa, A. Hillard, E. Pouget (University of Bordeaux), I. Makarchuk, B.P. Pichon (University of Strasbourg), F. Choueikani (Synchrotron SOLEIL, Saint-Aubin), A. Juhin (IMPMC-CNRS, Sorbonne Université, Paris)

Magneto-optical readout of a chiral single-molecule magnet at telecom wavelengths

The accelerating global demand for data storage and readout calls for transformative technologies that are compact, efficient, and sustainable. Magnetic memory devices are at the heart of modern data storage technologies, yet reliably reading magnetic states without perturbing the stored information remains a significant challenge. Optical readout methods, because of their non-invasive and contactless nature, offer a promising alternative. Complementary to conventional magneto-optical effects, such as Faraday rotation or Magnetic Circular Dichroism (MCD), Magneto-Chiral Dichroism (MChD) is emerging as a powerful magneto-optical effect that enables magnetic state detection without the need for polarized light.

Recently, some of us have demonstrated that the magnetic hysteresis of a chiral Dy(III) complex can be optically detected using unpolarized visible light through MChD. However, to integrate such molecular components into state-of-the-art optical devices, this methodology has to be extended to the near infrared (NIR) telecommunication range. In this wavelength range, optical fibers minimize losses in long-distance photon transport. This wavelength range also corresponds to the transparent optical windows of silicon, which allow integration of molecular optically responsive materials into optical components developed for silicon-based telecommunication applications.

To achieve this goal, we have prepared and investigated a new air-stable chiral single-molecule magnet (SMM) formulated as (S)- and (R)-[Dy(bbppn)Cl] (bbppn = N,N'-bis(2-hydroxybenzyl)-N,N'-bis(2-pyridylmethyl)-S-1,2-propanediamine). We demonstrate that the magnetic hysteresis of this SMM, despite exhibiting rapid quantum tunneling of magnetization (QTM) at zero field, can be optically detected using unpolarized light through MChD. Complementary to our seminal study limited to the visible range, we demonstrate that MChD-based readout is also effective for the Dy(III) $f-f$ transitions in the NIR region, confirming the robustness of this method across a broader spectral window (figure 58).

These findings establish MChD as a generalizable optical readout method for molecular magnetic materials, reinforcing its potential for future applications in polarization-free optical data readout technologies and optical communication at telecom wavelengths.

For more details please see [Aragon-Alberti *et al.* Journal of the American Chemical Society (2025) doi:10.1021/jacs.5c17544].

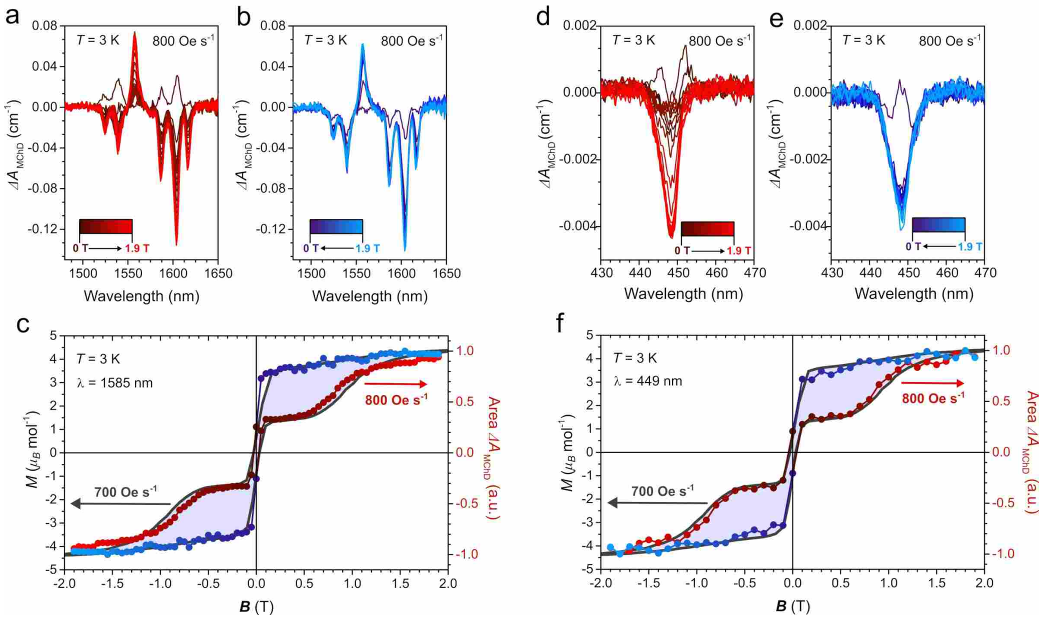

FIG. 58. *MChD spectra recorded at $T = 3.0\,K$ with B and k applied along the (011) axis of a single crystal of (S)-1 by sweeping the magnetic field from 0.0 to 2.0 T at a rate of 800 Oe s^{-1} and (b) from 2.0 to 0.0 T in the NIR range and (d, e) in the visible range under the same experimental conditions. (c, f) Comparison between the area of the MChD signals (dots) obtained by dynamic MChD measurements and magnetization data (grey line and filled area) acquired on a vibrating sample magnetometer at a sweep rate of 700 Oe s^{-1}.*

M. Aragon-Alberti, G. Novitchi, G.L.J.A. Rikken, C. Train, M. Atzori
H. Flichot, M. Gascoin, B. Le Guennic, O. Cador, F. Pointillart (ISCR-CNRS, University of Rennes)

Applied-Superconductivity

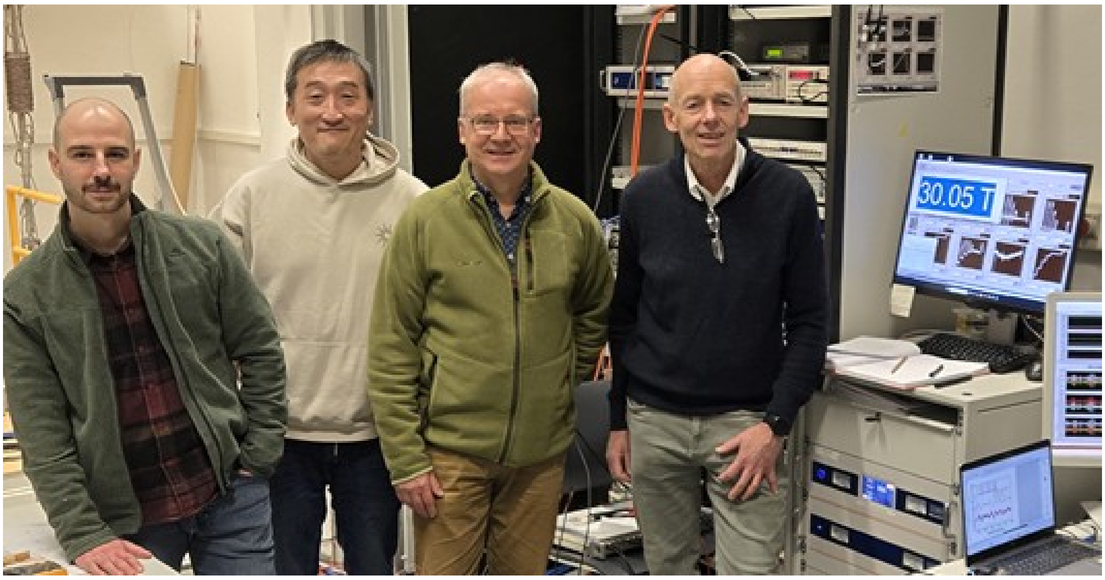

Superconducting critical current measurements in pulsed magnetic field up to 60T

Current research aims to enhance the critical current in high magnetic fields within a previously unexplored regime, around 20 K and above 40 T, and if possible to do so using high growth rate fabrication methods that enable increased manufacturing throughput [Puig *et al.*, Nature Review Physics **6**, 132 (2024)]. The reason is the new cutting-edge electromechanical machines (NMR, nuclear fusion and particle accelerators magnets) operating at large magnetic fields (>20-40 T) at temperatures higher than 4.2 K (*i.e.* $20-40$ K), where energy consumption is largely minimized.

Superconductivity has a fundamental physical limit to the critical current, known as the depairing current, which corresponds to the breakdown of Cooper pairs. However, this limit remains far from being reached in high-temperature superconducting (HTS) tapes. Recent studies from Barcelona and others have shown that increasing the charge carrier density in HTS, to reach the overdoped regime, brings the critical current closer to this limit.

Experimentally, a vast parameter space remains unexplored, particularly regarding the role of natural and artificial pinning centers, such as point defects, stacking faults, nanocolumns, and nanoparticles in the overdoped state.

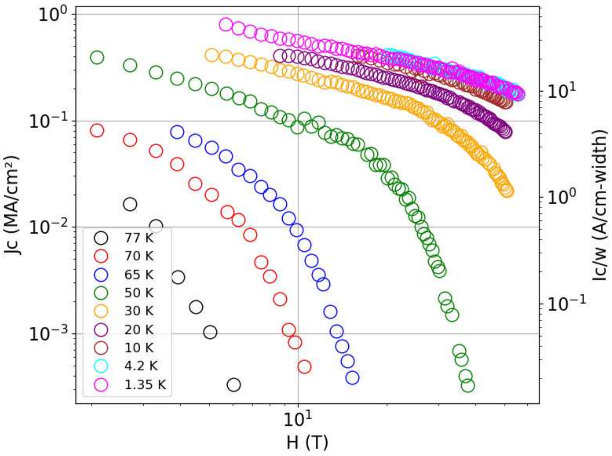

FIG. 59. *Log-log plot of the measured critical current density as a function of magnetic field up to 55 T in a REBCO thin-film for different temperatures in an overdoped sample with nanocomposites.*

The aim of this work is to experimentally investigate how the nanostructures influences the critical current of HTS thin-films in magnetic fields up to 55 T, by measuring four different superconducting REBCO thin-film samples, two pristine and two with nanocomposites, one of each being optimally doped and the other overdoped. The films were fabricated using the transient liquid assisted growth (TLAG) method, which achieves growth rates above 2000 nm/s.
All four samples were measured using an innovative measurement setup to perform transport $V-I$ measurements in pulsed magnetic field [Leroux et al. *et al.*, Phys. Rev. Applied **11**, 054005 (2019)]. However, there are limitations on the width of the bridge imposed by vortex physics. Using narrow bridges makes it possible to acquire a complete J_c versus B curve at one temperature in just a couple of magnetic field shots. Indeed, thanks to the narrow bridges of 20μm, it was possible to measure $V-I$ curves during the whole of the up sweep and down sweeps of the field.

Results for the nanocomposite overdoped REBCO thin-film sample are shown in figure 59, and a $V-I$ curve at 55 T and 1.35 K is shown in figure 60. A preliminary analysis of all samples shows the expected behaviour; the nanocomposite overdoped sample has the largest critical current at high fields of all samples.

A comparison of the high field behavior of the critical current is underway. We see hints of a universal $\log(B)$ scaling in the dependence at high field and low temperature, which could arise from vortex-vortex interaction. Further work is in progress in an attempt to confirm this hypothesis.

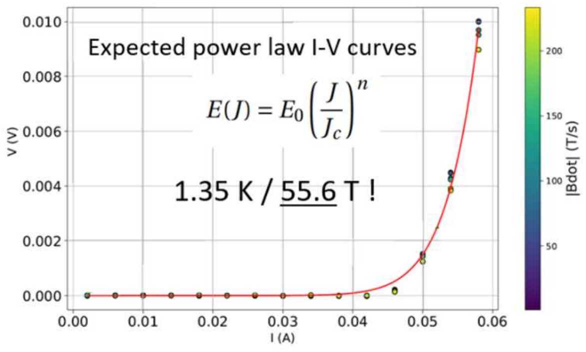

FIG. 60. *Voltage versus current curve in a superconducting REBCO thin-film bridge measured in the extreme conditions of 55.6 T and 1.35 K.*

J. Graglia, N. Bruyant, M. Leroux
O. Mola, C. Torres, J. Gutierrez, T. Puig (Institut de Ciència de Materials de Barcelona ICMAB-CSIC, Bellaterra)

REBCO coated conductors for CERN's high field magnet program

In the context of CERN's high field magnet (HFM) program, REBCO conductor from various manufacturers, see Table II, was procured for exploring HTS magnet technologies for accelerator applications in the range from 14 T up to 20 T. A campaign was launched to conduct mechanical, electrical and thermal characterisation of the REBCO conductor. The results of the planned campaign will be shared with partner institutes and with the broader community as part of the HTS conductor property database.

FIG. 61. *0.5 mm wide, 10 mm long bridge on 4 mm wide REBCO sample from SST. The lobes above and below the bridge can be used for voltage taps.*

Preliminary critical current characterization results for applied fields below 15 T, including a proposed critical current scaling law, were already published [Succi *et al.*, IEEE Trans. Appl. Supercond **34**, 8001007 (2024)]. Nevertheless, there is a great need to characterise the material at operating fields of the magnet designs being developed, *i.e.* magnetic fields in the range of 15-30 T, as well as quantify the critical current dependence on the magnetic field orientation.

TABLE II. Manufacturers of REBCO tapes used here.

Manufacturer	Abbreviation
Faraday Factory Japan	FFJ
Fujikura	FJ
Karlsruhe Institute of Technology	KIT
SuperPower (tape with AP formulation)	SP-AP
SuperPower (tape with HM formulation)	SP-HM
Shanghai Superconductor Technology	SST

Samples were measured in perpendicular and parallel field orientations. To limit the current needed during measurements, for perpendicular field orientation 2 mm wide samples were used when available as received from the manufacturer, and for measurements in parallel field configuration, 1 cm long and 0.5 mm wide bridges were used, made by laser striation on 4 or 12 mm wide tapes, see figure 61. The reduced width samples helped to mitigate issues associated with excessive sample heating and trapped helium bubble formation. Total sample length in each case is 3 cm. All tested samples have 20 μm surround copper coating, and to further stabilize the samples, an additional 120 μm copper strip was soldered to each sample.

The measured critical current values given per centimeter width of the conductor to account for samples of different widths. The critical current results for measurements in perpendicular field are shown figure 62(a). No bridged samples were used for measurements in perpendicular field. Samples from SP-HM and FJ were 2 mm wide, the remainder - 4 mm.

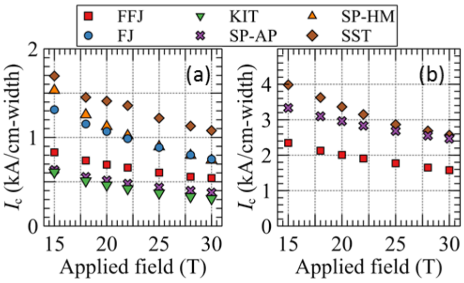

FIG. 62. *Critical current of the of REBCO samples: (a) with $\theta = 90°$, $\perp$ to the applied field direction with respect to tape width and applied current. (b) with $\theta = 0°$, $\parallel$ to the applied field direction with respect to tape width and applied current.*

The critical current with field oriented in the plane of the REBCO tape is typically 2-3 higher compared to performance in perpendicular field. Laser structured bridge samples had to be used with only a few exceptions due to maximum current constrains of the sample holders. The results for measurements in parallel field configuration are shown in Figure 62(b).

Critical current of a sample from SST was measured as a function of magnetic field orientation in a range of angles from 15° to 90° with full-width 4 mm sample, see figure 63. The dataset was extended to 0° by using the data collected using the bridged sample in probe with fixed sample orientation figure 62(b). Several data points for certain field orientations were excluded due to excessive sample heating due to decrease in helium level during the measurement.

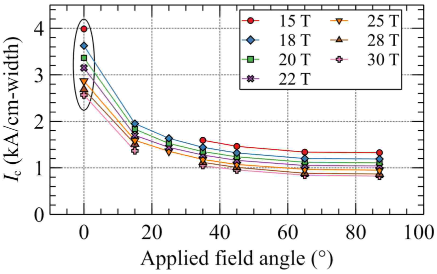

FIG. 63. *Critical current of REBCO from SST as a function of magnetic field orientation with respect to tape surface.*

This work forms an essential contribution to the broader HFM conductor characterization effort, supporting the development of HTS materials and magnet designs for future accelerators at CERN.

H. Himanshu, J. Song, X. Chaud
A. Baskys, A. Saba, A. Ballarino (CERN, Geneva)

High-field transport measurements of 12-layer STAR REBCO wires

STAR® (symmetric tape round) REBCO wires are a class of superconducting conductors designed to combine the high-field performance of coated conductors with the geometric and mechanical advantages of round wires. With overall diameters in the 2-3 mm range and engineered symmetric tape architectures, these conductors can tolerate very small bend radius (down to $\simeq$ 15 mm) while maintaining high critical current over a wide temperature range from 4.2 K up to liquid-nitrogen temperature (77 K). In the symmetric tape configuration, the REBCO layer is positioned close to the neutral bending plane through an optimized combination of thin, high-strength substrate and surrounding copper stabilizer, thereby reducing tensile and compressive strain during bending and operation in high magnetic fields.

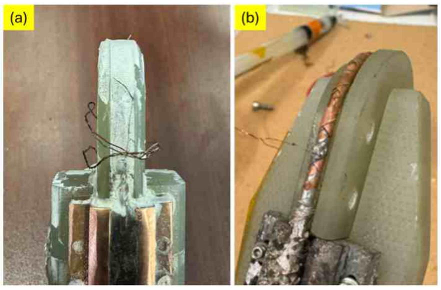

FIG. 64. *12-layer STAR wire samples arranged in a 30 mm bend-diameter configuration: (a) wax-impregnated STAR wire and (b) non-impregnated STAR wire.*

We have investigated wax-impregnated and non-impregnated 12-layer STAR wire cables arranged in a 15 mm bend-radius configuration (figure 64). The voltage-current ($V-I$) curves shown in figure 64(a) correspond to a wax-impregnated 12-layer STAR wire measured in self-field, the wire exhibits a critical current of above 1 kA, with an n-value of approximately 40 obtained from a power-law fit to the transition region. To verify the current injection conditions, additional current ramps up to 4 kA were carried out at 4 K with ramp rates of 0.1 kA s^{-1}. No quench, noticeable temperature rise, or excess voltage noise was observed, indicating stable current transfer to the sample.

Figure 65(b) shows the measured field dependence of I_c. The two curves overlap within the error bars over the entire field range (15-30 T), demonstrating that no measurable degradation occurred during the measurements and confirming that the wax impregnation effectively stabilized the tape under high-field cycling.

All wax-impregnated STAR wire samples could be ramped to fields above 25 T without damage or instability, and full $V-I$ curves were obtained for each. In contrast, the non-impregnated samples showed large voltage noise during high-field ramps, and two of them were damaged during measurement; Lorentz-force-induced bending of the conductor was also observed, as seen in Figure 66.

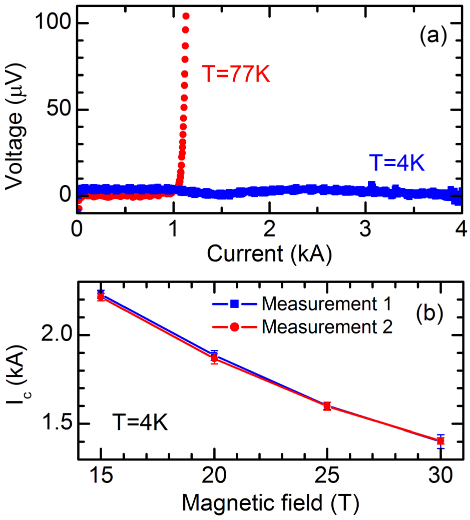

FIG. 65. *(a) $V-I$ curves of a wax-impregnated 12-layer STAR wire in self-field. The 77 K curve shows a critical current above 1 kA with $n \simeq 40$, while the 4 K ramps up to 4 kA demonstrate stable current injection without quench. (b) Magnetic field dependence of I_c.*

FIG. 66. *A non-impregnated STAR wire after high-field measurement, showing Lorentz-force-induced bending and deformation of the wire.*

In summary, the measurements demonstrate that wax impregnation provides the mechanical reinforcement needed to preserve conductor integrity and enable reproducible I_c characterization up to 30 T. The failures, deformation, and noise observed in the non-impregnated samples highlight the importance of impregnation or equivalent mechanical support for reliable operation of STAR wires in extreme field environments.

H. Himanshu, J.B. Song, X. Chaud
M. T. Paulose, J. S. Sandra, V. Selvamanickam (University of Houston, Texas)

Design of all-superconducting user magnets

We are developing all-superconducting magnets, combining high temperature superconductor (HTS) insert magnets, an emerging technology that work in field above 25 T, with low temperature superconductor (LTS) outsert magnets. The use of HTS inserts introduces a change of paradigm by providing an unprecedented combination of high magnetic field and long measurement times for scientific research whilst saving vast amounts of energy, as a complementary offer to power-intensive resistive magnets (up to 38 T).

The design magnetic field targets were 32+T and 40+T. The 32+T design proposed to combined a single stack of HTS pancakes in combination with a 19 T/150 mm LTS magnet. The 40+T design used either a similar arrangement at the sake of a narrower central space, or a design with two nested HTS coils combined with a 15 T/250 mm LTS magnet. We use metallic tape co-wound with the bare HTS tape. This so-called metal as insulation (MI) technology enables a self-protection feature of the HTS coil by allowing the electrical bypass of defects as well as better mechanical performances in a very compact winding [Lécrevisse *et al.*, Supercond. Sci. Technol. **35**, 074004 (2022)].

FIG. 67. *MI HTS mock up coils made of a stack of two double pancakes to test in-situ the HTS tapes close to their operating condition at 4.2 K in magnetic field background up to 20 T.*

While testing tapes from several suppliers, although the critical current capacity not only under high field but also at different angle due to anisotropy is a prominent parameter for the HTS insert dimensioning, some other properties were found even more relevant with regards to the insert fabrication, notably delamination strength and windability. This last criterium has driven the choice to use Theva APC (artificial pinning center) tape.

The design of the HTS inserts is based on a multiphysics parametric study under constraints of geometry, current margin on the load line taking into account different anisotropic fits of the critical current of REBCO conductor, mechanical stress and deformation with analytical formulations of MI windings [Durochat *et al.*, IEEE TAS **34**, 4904305 (2024)]. Examples are given in table III.

The designs are not limited by the critical current of the tape, but rather by the mechanics of the magnet, and the maximum strain at which the critical current of the tape will irreversibly degrade. A value of 0.4% for the maximum strain at the tape level was assumed to be safe. At this stage, mechanical cycling is not considered, but might limit further the performances.

HTS mock-up coils (figure 67) were fabricated and tested under magnetic fields up to 20 T in resistive background field. The measured critical currents are much higher than the nominal current used in the designs, demonstrating a comfortable thermal margin, but lower than the theoretical predictions, indicating some degradation occurs during manufacturing.

The interfacing of an HTS insert with a 19 T/150 mm LTS magnet manufactured by Oxford Instrument, and installed at HZDR, Dresden was developed, providing de facto a test bench for valuable information about the HTS/LTS coupling. Specific simulations conducted in parallel highlighted a quench asymmetry generating axial forces up to 50 tons, requiring mechanical reinforcement of LTS magnets.

This project opens the way for the installation of such a 40 T all-superconducting magnet at the high field facility in Grenoble.

TABLE III. Optimised single 40 T solenoid designs using Theva APC tape

Internal diameter	50 mm	30 mm	40 mm
Double pancake number	21	25	25
Turns per pancake	360	420	380
Total length	3.2 km	4.9 km	4.8 km
Nominal current	312 A	304 A	309 A
Critical current	398 A	373 A	389 A
Current margin	21.6 %	18.5 %	20.6 %
HTS field	21 T	24 T	22 T
Total field	40 T	43 T	41 T
Max. hoop stress	758 MPa	678 MPa	707 MPa
Max. deformation	0.42 %	0.38 %	0.39 %

X. Chaud
Thomas Herrmannsdoerfer (HLD/HZDR, Dresden), U. Zeiltler (HFML, Radboud University, Nijmegen), P. Fazilleau (CEA,Université Paris-Saclay), C. Senatore (DQMP, University of Geneva), M. Dhallé (University of Twente, Enschede), E. Pardo (Institute of Electrical Engineering, Slovak Academy of Sciences, Bratislava), A. Smara (Theva Dunnschichttechnik GmbH, Ismaning), A. Twin (Oxford Instruments NanoScience, Abingdon), P. Revilak (Bilfinger Engineering and Technologies GmbH, Würzburg)

Estimating delamination strength of new REBCO conductors

Here we present a detailed evaluation of the delamination strength of four commercially available REBCO coated conductors-THEVA (TV), Shanghai Superconductor Technology (SST), Faraday Factory Japan (FFJ), and Fujikura (FJK)-using the procedures implemented in the study. Delamination is one of the most critical mechanical reliability indicators for REBCO tapes, as insufficient interlayer bonding can lead to tape failure during winding, joint fabrication, or high-field magnet operation. Previous generations of these tapes, particularly those manufactured around 2022, exhibited significant delamination rates, resulting in frequent coil failure during magnet fabrication. In 2024, new versions of the TV, SST, and FFJ tapes were received, with improved delamination strength and edge thickness uniformity. Table IV summarizes the specifications of the four tapes used in this study. All tapes had a width of 6 mm. The measured total thicknesses of TV, SST, and FJK tapes were approximately 73-76 μm, while the FFJ tape was thinner (60-64 μm) due to a reduced substrate thickness. Notably, the new tapes from TV, SST, and FFJ, produced in 2023-24 to address mechanical shortcomings reported in our previous study [Song *et al.*, IEEE Trans. Appl. Supercond. **34**, 4300206 (2024)], replaced the older tapes manufactured in 2022. The new TV and FFJ tapes have been improved over the old tapes, exhibiting enhanced delamination strength. Furthermore, the new FFJ and SST tapes show significantly reduced edge thickness asymmetry compared to their older counterparts.

TABLE IV. Physical description of REBCO tapes

Unit	**TV**	**SST**	**FFJ**	**FJK**
Width [mm]	6±0.1	6±0.1	6±0.1	6±0.1
Stabilizer thick. [μm]	10±1	10	10±2	5
Substrate thick. [μm]	50	45	37±3	50
Total thick. [μm]	74–76	74–76	60–64	73–75
Produced (old)	09/2022	09/2022	10/2022	12/2022
Produced (new)	01/2024	02/2024	05/2024	-

The delamination strength was evaluated using two practical procedures; (i) adhesion and removal of polyimide tape (figure 68(a)), and (ii) mechanical cutting after solder pre-tinning (figure 68(b)). For each conductor, multiple samples were extracted from every spool to ensure a representative assessment across length. The delamination ratio was defined as the number of samples exhibiting interlayer separation divided by the total number tested. This metric provides a direct comparison of the intrinsic adhesion strength of the REBCO-substrate-stabilizer structure. Figure 69 of the study demonstrates the dramatic contrast between the older and newer versions of the tapes. The SST tape exhibits the most significant delamination strength; none of the tested samples, past or present, show measurable delamination, indicating exceptionally strong interlayer adhesion and high suitability for magnet fabrication. The updated TV tape, whose earlier version suffered extremely high delamination rates approaching complete failure (approximately 93%), now shows a substantial reduction to around 16% in the 2024 production. This improvement reflects a meaningful reinforcement of mechanical integrity, though occasional delamination events indicate that further optimization is still necessary. In the case of FFJ, the tapes also show notable progress, with delamination rates dropping from 50% in the 2022 batch to approximately 6% in the 2024 prouction, demonstrating that the tape's delamination strength is sufficient for coil manufacturing.

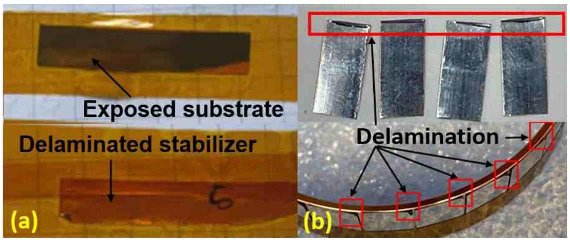

FIG. 68. *Pictures of delaminated tapes after removing polyimide (a) and mechanical cutting after pre-tinning (b).*

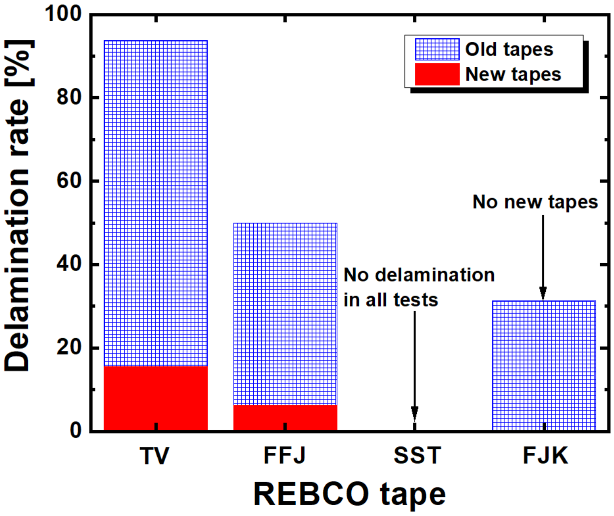

FIG. 69. *Delamination rate of older and newer REBCO tapes.*

Overall, the delamination assessment reveals that recent manufacturing updates have significantly enhanced the mechanical robustness of modern REBCO tapes. SST exhibit excellent interlayer adhesion with no measurable delamination, while TV and FFJ show substantial but incomplete improvement. Despite this progress, the TV tape still requires further improvements to fully eliminate the risk of delamination during coil fabrication.

J. B. Song, H. Himanshu, R. Raison, J. Spitznagel, X. Chaud

Mechanical behavior and stress/strain response of REBCO conductors

Rare-earth barium copper oxide (REBCO) superconducting tapes have experienced a rapid rise in demand and production, driven largely by high-field magnet and fusion applications. With the ongoing push for higher critical current density and long-length deposition, material used and fabrication processes continue to evolve. This makes regular independent evaluation and comparison of commercial products essential. In this work, we benchmarked tapes from four of the major manufacturers, namely THEVA (TV), Fujikura (FJK), Faraday Factory Japan (FFJ), and Shanghai Superconducting Technology (SST), assessing their mechanical performance at room temperature. In addition, two batches of TV conductors from different production years were compared, highlighting improvements in their overall suitability for high-field magnet applications.

The general layered architecture of these tapes consists of a thin film ($1 - 2\,\mu$m) of REBCO superconducting material, deposited on Hastelloy substrate with intermediate buffer layers, and protected by Ag and Cu stabilizer layers on the surface. In this study, we used 6 mm wide tapes from all the manufacturers. To assess mechanical performance, we used MTS system model C43. The tensile properties of the tapes were characterized using traction tests at room temperature. Samples from each manufacturer were held between two sanded Cu pieces (120 grit), with the tape positioned at the center, and then mounted on the test system claws. The load was applied to maintain a constant elongation rate of 0.02 mm/s and load-elongation data were recorded until failure.

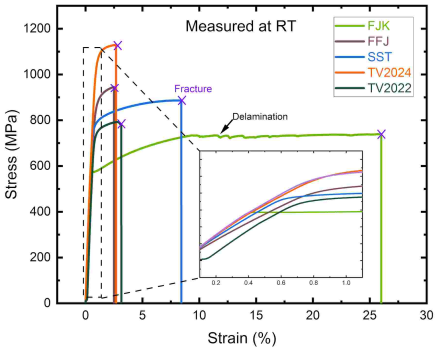

FIG. 70. *Mechanical characterization of HTS tapes at room temperature. Comparison of stress-strain curves of different manufacturers until the break point.*

Stress-strain curves provide a baseline comparison of the mechanical properties. Parameters such as Young's modulus (E), yield strength ($Rp0.2$), and ultimate tensile strength are useful indicators of tape robustness and can guide preliminary magnet design considerations. Although mechanical data for REBCO tapes exist in the literature, they show notable variation, even between batches from the same manufacturer. This may arise from differences in test setups or from ongoing modifications to the Cu stabilizer and Hastelloy substrates that manufacturers are rapidly introducing to improve electrical performance. To strengthen the available database, we have tested four samples from each supplier, and the averaged values are presented in table V. For all the tapes, there is an initial linear elastic region, followed by plastic region (at point $Rp0.2$), where the deformation is irreversible and damage to the material's superconducting properties is expected (often I_c degrades before this point in the elastic regime).

TABLE V. Measured mechanical parameters of different tape companies, Young's modulus (E), Yield strength Rp0.2 (YS), ultimate tensile strength (UTS) and tape fracture strain (TFS).

Sample	E (GPa)	YS (MPA)	UTS (MPA)	TFS (%)
TV2022	136 ± 1	812 ± 5	880	3.1
TV2024	144 ± 1	1016 ± 4	1130	2.7
FJK	134 ± 1	569 ± 2	734	24.8
FFJ	114 ± 1	848 ± 2	943	2.5
SST	127 ± 1	775 ± 3	890	8.4

Good consistency was observed across the four samples from each company. Young's moduli lie between $110 - 150$ GPa, highest for TV2024 and lowest for FFJ. $Rp0.2$ is lowest for FJK tapes (569 ± 2MPa) and highest for TV tapes from 2024 batch (1016 ± 4MPa), highlighting differences in tensile stress tolerance. FJK tapes also showed largest strain levels before fracture (more than 25 %), much higher than the next lower value 9 % for SST. One possible reason could be the fact that FJK tapes have 50 % less Cu on each side and thicker Hastelloy substrate. Together, these two factors may cause Hastelloy's mechanical properties to dominate the stress-strain response. During testing, it was also observed that FJK tapes delaminate at the Ag - REBCO interface, visible as irregular deviations in the otherwise smooth green curve (FJK) in figure 70 near 10 % strain. A comparison of 2 batches of TV tapes reveals that the 2024 batch exhibits better mechanical performance. Both $Rp0.2$ and ultimate tensile strength are higher for the 2024 batch. The 2022 tape breaks at ~ 300 MPa lower stress, possibly due to weak delamination previously reported by Song *et al.*, IEEE TAS **34**, 5 (2024).

The present work provides the mechanical limits of commercial REBCO conductors at room temperature. The electro-mechanical measurements at cryogenic temperatures, essential to fully assess their performance, are currently in progress.

H. Himanshu, J.B. Song, O. Jay, and X. Chaud

Electrical and thermal performance of industrial REBCO tapes

Rare-earth barium copper oxide (REBCO) coated conductors (CCs) have emerged as the leading candidates for building next-generation very high-field magnets. In continuation of our previous work on tape characterization (Song *et al.*, IEEE TAS **34**, 5 (2024)), we have carried out tests of electrical performance at 77 K self-field and thermal stability of tapes from multiple suppliers. We have investigated high-temperature superconducting (HTS) REBCO tapes from four manufacturers, namely, THEVA (TV), Fujikura (FJK), Faraday Factory Japan (FFJ), and Shanghai Superconducting Technology (SST).

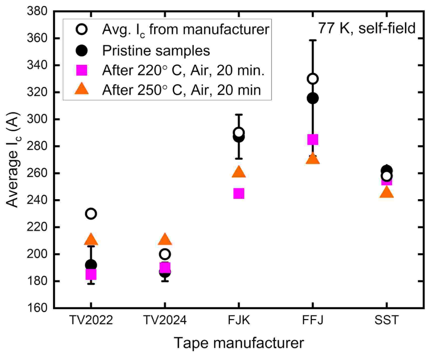

FIG. 71. *Average value of I_c at 77 K for different tape companies before and after heat treatment.*

I_c comparison across manufacturers reflects the performance of different tapes under the same operating conditions. We have measured I_c at 77 K of about 100 samples and the obtained parameters are summarized in figure 71. The measured I_c values are close to the manufacturer specifications, only TV2022 showed slightly lower value. FJK, FFJ and SST tapes show relatively higher I_c than TV, indicating superior current-carrying capability at 77 K without any external field. In addition, standard deviation in I_c values is lowest for SST (1.7), reflecting excellent consistency in electrical behavior. Although FFJ has highest average I_c (315.6 A), the standard deviation is also largest at 42.9. The two TV tape batches do not show any significant differences in this regard.

Thermal stability investigation is another important step to assess the impact of heat exposure on the conductor's performance, and to ensure damage-free joint fabrication. To assess the impact of heat, samples were heat treated in a furnace (in air) at 220°C and 250°C for 20 minutes. Four samples of each manufacturer were treated, and their I_c values were remeasured afterwards (see figure 71). The average I_c of each manufacturer showed no significant degradation, confirming good intrinsic thermal resistance against high-temperature exposure. Furthermore, soldered lap joints in REBCO conductors require the application of heat with pressure from the soldering iron, which can impact the tapes differently compared to uniform furnace annealing. To investigate this, we tested about 25 samples from each manufacturer by tinning them with $\mathrm{Sn_{60}Pb_{40}}$ solder at selected temperatures between 200 − 250°C.

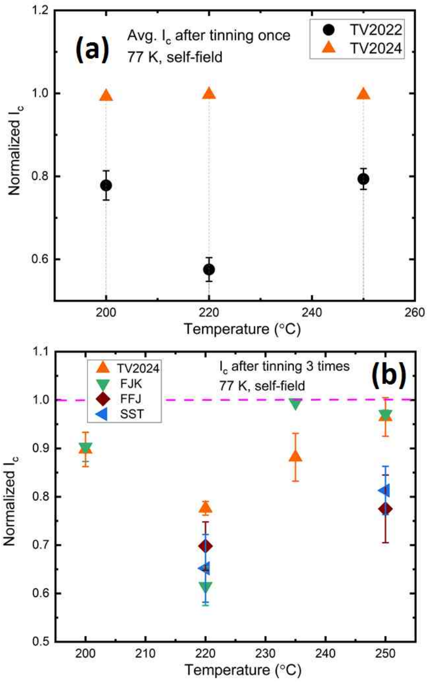

FIG. 72. *Comparison of I_c at 77 K of different tapes after tinning with $\mathrm{Sn_{60}Pb_{40}}$ solder at different temperatures. (a) TV tapes 2022 and 2024 batches after tinning once (b) different manufacturers after tinning 3 times.*

Figure 72(a) compares the two batches of TV conductors (avgerage I_c of 5 samples at each temperature); the TV2022 batch shows significant I_c degradation even at 200°C. The TV2024 batch, on the other hand, displays much greater resilience, confirming improvements in tape quality. Since joint fabrication often involves multiple tinning cycles, we extended the study to all the companies by tinning the same region three times and re-measuring I_c. The results (figure 72(a)) reveal an interesting feature; the strongest degradation occurs at 220°C, while samples treated at other temperatures retain comparatively higher I_c. We hypothesize the possibility of solder wettability, which is slow at 220°C but already damaging in temperature, above 230°C wetting is rapid-minimizing exposure. Our findings suggest that uniform furnace heating is not dangerous but the tape I_c can degrade at certain temperatures while tinning with soldering iron and one needs to attain a more favorable compromise between solder wetting and conductor preservation for damage-free joint fabrication.

H. Himanshu, J.B. Song, O. Jay, and X. Chaud

Estimating windability of new REBCO conductors

In our previous evaluation of windability, we observed that four REBCO coated conductors except those from TV exhibited significant deformation during high-tension double-pancake (DP) winding. SST, FFJ, and FJK tapes showed various forms of lifting, buckling, or conical distortion, preventing reliable coil fabrication unless the winding tension was substantially reduced. Motivated by these limitations and persistent issues reported in 2022-era tapes, particularly delamination and edge-thickness asymmetry, the present study reexamines windability using newly manufactured 2023-2024 versions of TV, SST and FFJ tapes to assess how recent mechanical improvements translate into coil-level performance. DP coils were wound on 50 mm stainless-steel inner rings using a winding tension (WT) of 100 MPa, a stress level required to preserve the turn-to-turn contact during energisation and so the effectiveness of the protection aimed by the metal-as-insulation winding technique. Among the updated conductors, the new TV tape once again exhibited excellent windability (figure 73). Both DP coils were wound and removed from the mandrel without any signs of deformation, such as lifting or conical shaping.

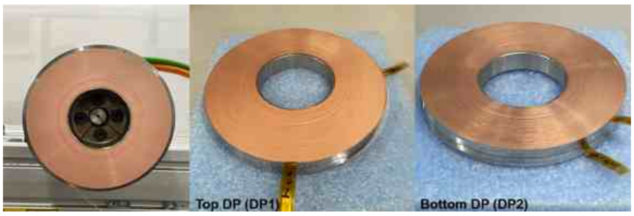

FIG. 73. *Pictures of new TV DP 1 (a) and DP2 (b) coils at a winding tension of 100 MPa.*

The new SST tape shows substantial progress compared to earlier versions. In prior campaigns, SST tape had been particularly prone to deformation arising from edge-thickness asymmetry, which produced repeatable lifting during coil extraction. In the present evaluation, one DP coil was completed without difficulty, while the second exhibited local lifting only during removal from the winding machine. Rewinding the coil with the opposite edge orientation fully eliminated the deformation, in the figure 74(b). This behavior indicates that SST has largely mitigated, but not completely removed, the mechanical asymmetries responsible for its earlier windability issues.

Figure 75 shows the DP coils wound with the new FFJ tape. In previous tests, it was impossible to construct FFJ DP coils with WTs from 100 MPa to 40 MP due to the uneven winding arrangement as well as the conical shape deformation of the coil. In the case of new FFJ tape, although the first DP coil could be fabricated at 100 MPa (figure 75(a)), the second coil repeatedly failed even when tension was reduced to 50 MPa (figure 75(b)). The tape developed severe conical deformation and inconsistent turn geometry that persisted regardless of adjustments to the tape orientation or spool position. These recurring failures made it impossible to obtain two matching DP coils, thereby preventing the construction of a mock-up magnet. Overall, the windability evaluation shows that the TV tape exhibits the best mechanical performance among all conductors tested, enabling the most reliable high-tension DP coil fabrication. In addition, despite the enhanced windability observed in both new SST and FFJ tapes, residual minor deformation persisted, indicating that further advances in thickness uniformity and mechanical winding stability are still needed.

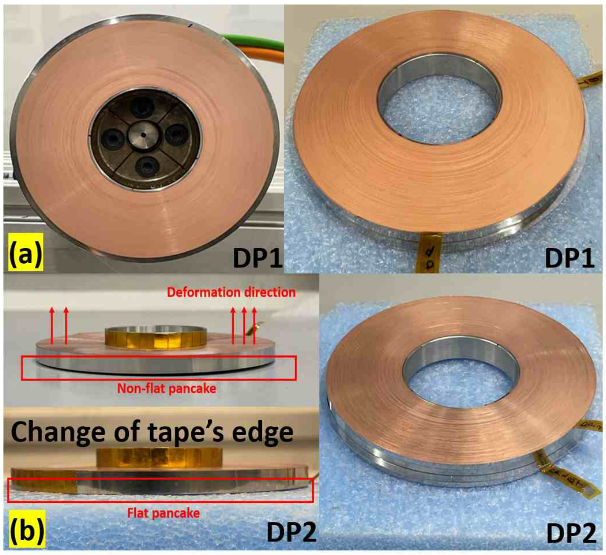

FIG. 74. *Pictures of new SST DP 1 (a) and DP2 (b) coils at a winding tension of 100 MPa*

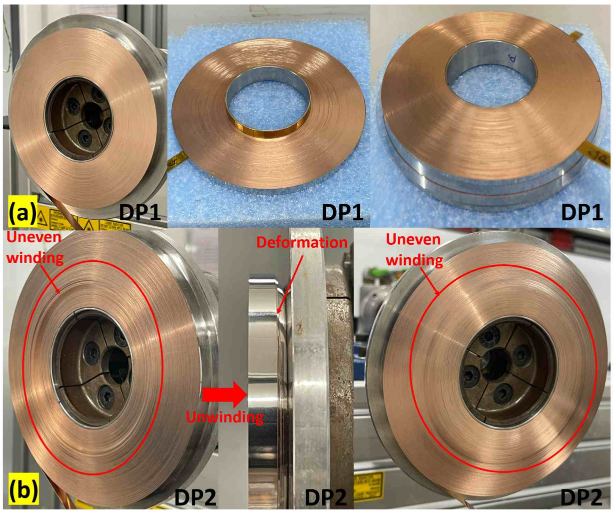

FIG. 75. *Pictures of new FFJ DP 1 (a) and DP2 (b) coils at a winding tension of 100 MPa.*

J. B. Song, H. Himanshu, R. Raison, J. Spitznagel, X. Chaud

Charging tests of REBCO mock-up magnets under B_{ext} at 4.2K

Three mock-up magnets were constructed using the successfully fabricated double pancake (DP) coils from TV, SST, and FJK (used in place of FFJ due to winding failure). Specifications of the magnets are shown in Table VI. Though the magnets share similar geometry, differences in turn counts and winding tension resulted in variations in inductance and coil constants. For instance, the FJK coils were wound at a reduced winding tension (WT) of 50 MPa to avoid deformation.

TABLE VI. Mock-up magnet specifications

Parameter	TV	SST	FJK
DP count	2	2	2
ID/OD [mm]	50/111.5	50/111.4	50/113.8
Turns per SP	281	295	304
Winding tension [MPa]	100	100	50
Overband turns	48	48	48
Overband tension [MPa]	100	100	100
Coil const. [mT/A]	17.2	18.2	18.5
Inductance [mH]	83	91.6	98.5
I_{qi} @ 77 K [A]	48	47	52

Old versus new THEVA magnets

Both the new TV DP coils, the old TV DP coils described in our previous work, were assembled as mock-up magnets. The coils are identical except for the production year of the tape. Figure 76 compares charging performance of mock-up magnets made with old and new TV tapes under various background magnetic fields (B_{ext}) at 4.2 K. The old magnet performed well up to 10 T, but quenched at 405 A at 15 T. After repeated quenches, it showed signs of degradation, likely due to poor delamination strength affecting the joints. This was further confirmed through unwinding the degraded coil. Figure 77 shows the delaminated innermost turn (inner joint region) of the degraded mock-up magnet. In contrast, the new TV magnet charged reliably up to 400 A at 15 T without quench events. At 20 T, it reached 350 A, limited by cryogenic instability (helium bubble trapping). The maximum center field of the new TV magnet was 26.3 T with current density $J_e = 777.8\,\mathrm{A/mm^2}$.

FJK versus SST magnets

Figure 78 shows charging performance of FJK and SST magnets under various B_{ext} at 4.2 K. The FJK magnet was initially tested in an LTS outsert at HLD in Dresden, where it quenched at 303 A in a 17 T field, also triggering a quench of the LTS magnet. Because quench signals were not recorded due to the powering off for LTS protection, it was re-tested in a resistive magnet. The coil was ramping up for a 500 A charging in SF, however, it quenched at 450 A. The I_{quench} of 450 A in SF is lower than the expected current because of (i) a slight kink of tape in the top DP coil during the winding process or (ii) the joints of the coil were damaged during the HTS/LTS quench event. While the FJK magnet at 17 T reached 400 A once, it degraded rapidly to 174 A after two quenches, consistent with weak delamination strength of tape. In the case of new SST tape, the mock-up magnet charged up to 400 A at 20 T (B_{tot} = 27.5 T, J_e = 888.9 A/mm^2) and showed no degradation after multiple quenches. These results confirm that good delamination strength is essential not just for fabrication, but also for magnet reliability under operational stress.

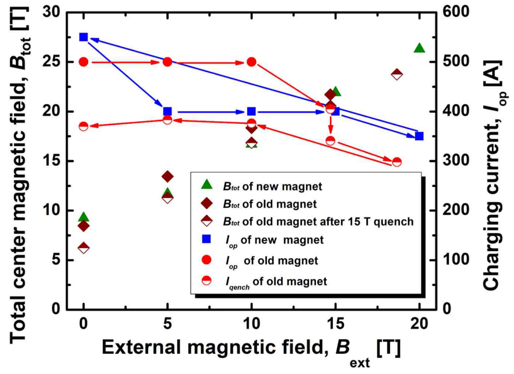

FIG. 76. *Charging/quench currents and total center magnetic fields of old and new TV magnets under various B_{ext}.*

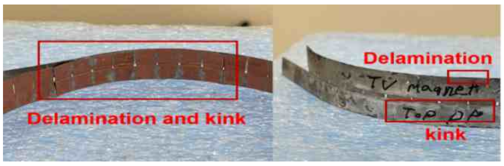

FIG. 77. *Photographs of the internal electrical junction between single pancakes after quench events.*

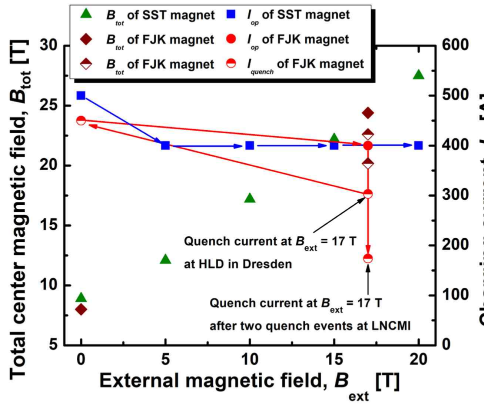

FIG. 78. *Charging/quench currents and total center magnetic fields of SST and FJK magnets under various B_{ext}.*

J. B. Song, H. Himanshu, R. Raison, J. Spitznagel, F. Debray, X. Chaud

Electrical performance estimation of REBCO mock-up magnets

To evaluate the electrical performance of the mock-up magnets, both sudden-discharging tests and quench tests were carried out for each coil. The sudden-discharging tests were used to determine the characteristic resistance of the magnets, while the quench tests allowed us to compare the measured critical currents with the simulated values.

Characteristics resistance change

Figure 79 shows characteristics resistance (R_c) values estimated from sudden discharge tests at 20 A in SF. At 77 K, R_c values were; TV 0.67 Ω, SST 3.3 Ω, and FJK 5.8Ω. The high R_c in the FJK magnet reflects weaker turn-to-turn contact due to the lower winding tension (WT, 50 MPa). Although both TV and SST coils were wound at 100 MPa, the SST coil exhibited a higher R_c, possibly due to a rougher stabilizer surface. Upon cooling to 4.2 K, R_c decreased for all three magnets. This reduction is attributed to increase turn-to-turn pressure, improved surface conditions, and reduced metal resistivity, all of which contribute to lower contact resistance. Subsequent quench events caused minimal change in R_c for the TV and SST magnets, indicating stabilized contact interfaces. In contrast, the FJK magnet exhibited a significant drop in R_c from 3.1Ω to 0.1Ω after repeated quenches. This behavior suggests post-quench mechanical settling of the loose windings in the low-tension FJK coil, leading to improved electrical contact between turns.

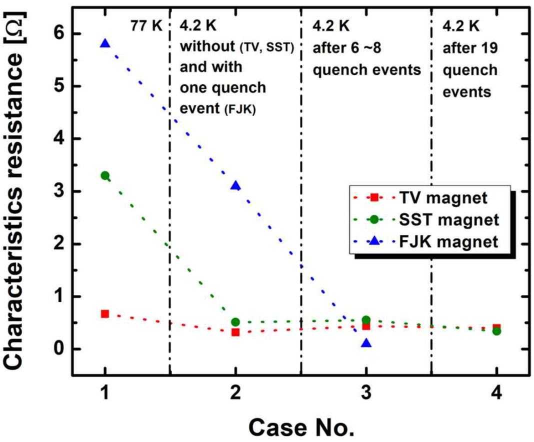

FIG. 79. *The estimated R_c of the magnets in SF at 77 and 4.2 K.*

Quench tests at various B_{ext} and temperatures

To determine critical current (I_c) dependence on field and temperature, quenches were induced by halting the helium flow at chosen operating currents. Results for TV and SST magnets are shown in figure 80, and calculated I_c values of TV and SST tapes are summarized in Table VII.

Note that the calculated I_c values of the tapes are based on the model described in reference Zermeño *et al., Supercond. Sci. Technol.* **28**, 085004 (2015). I_c decreased with increasing temperature at a rate of 10.2 A/K for TV and 3.8 A/K for SST tapes. At 10 T, TV had higher I_c, but SST outperformed TV at fields ≥ 15 T, consistent with the I_c calculated values of tapes. Meanwhile, the measured I_c of the magnet was lower than the average I_c of the tapes, even after accounting for the additional magnetic field generated by the magnet itself. This discrepancy likely reflects Joule heating at the inner and outer joints, local I_c minima along the conductor (points of lowest critical current), and minor degradation introduced during fabrication.

TABLE VII. Calculated I_c at 4.2 K

Field	**TV [A]**	**SST [A]**
0 T	718	593
10 T	608	568
20 T	511	529

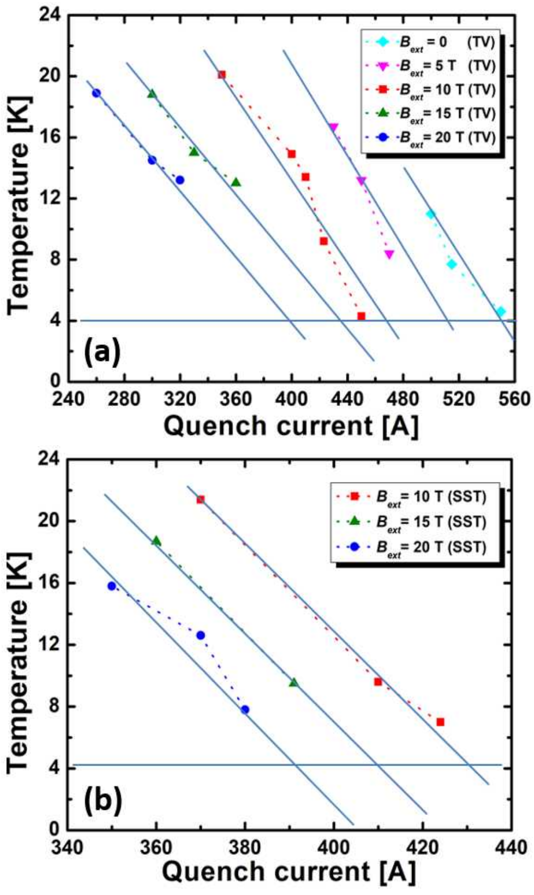

FIG. 80. *Quench currents of new TV (a) and SST (b) magnets as a function of temperature and magnetic field.*

J. B. Song, H. Himanshu, R. Raison, J. Spitznagel, F. Debray, X. Chaud

30T achieved in NOUGAT HTS-LTS hybrid magnet

The forty-Tesla all-superconducting user magnet (FASUM) project aims to develop a forty-tesla, fully superconducting magnet designed to provide reliable and accessible high-field capabilities for future users. To develop the FASUM magnet, we have spent the past three years working in close collaboration with Oxford Instruments to procure a high-performance low-temperature superconducting (LTS) magnet. This magnet provides a usable bore of 19 T / 140 mm and is expected to be delivered around September 2026, where it will serve as the core platform for integrating a high-temperature superconducting (HTS) insert.

In preparation for the final design and manufacturing of this HTS insert, it is essential to evaluate the mutual electromagnetic effects between the HTS and LTS magnets, which can induce currents, modify local magnetic-field distributions, and affect transient responses during charging or quench events, thereby impacting operational stability, energy-dissipation pathways, and protection strategies. To experimentally assess these effects, we carried out integrated LTS tests using an HTS insert fabricated within our previous HTS project, NOUGAT (10 T HTS insert combined with a 20 T resistive outsert).

In this campaign, the NOUGAT insert was integrated into the LTS outsert magnet at HLD in Dresden. The LTS outsert at HLD has specifications very similar to those of the FASUM LTS magnet. Designed and manufactured by Oxford Instruments, it provides a maximum field of 19 T with a bore diameter of 150 mm. Figure 81 shows the installation of the NOUGAT HTS insert inside the HLD outsert magnet.

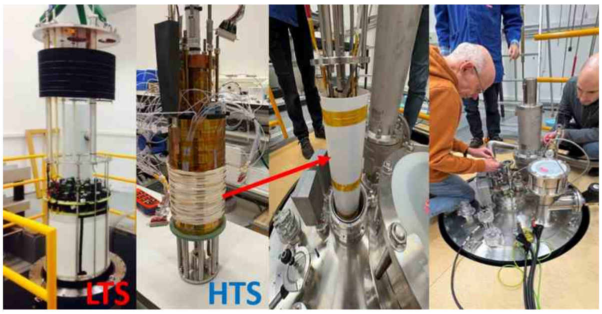

FIG. 81. *Installation of the NOUGAT HTS insert into the LTS outsert magnet at HLD in Dresden.*

Figure 82 presents the magnetic-center fields of the NOUGAT HTS insert, the HLD LTS outsert, and the combined hybrid magnet during the tests. The first test campaign, conducted in October 2025, demonstrated that the LTS/HTS hybrid magnet could be charged up to 28.2 T (10.2 T from the HTS insert with 18 T from the LTS outsert), where the field was stably maintained for approximately five minutes. The second test campaign was carried out during the first week of December 2025. In this run, the hybrid magnet was again energized to 28.2 T and held for about 30 minutes to evaluate helium consumption and overall operational stability. After performing additional investigations, including the vortex-shaking effect, and the impact of different charging sequences, the magnet was successfully ramped to a maximum field of 30 T (12 T from the HTS insert combined with 18 T from the LTS outsert). The system operated for 20 minutes at this field without any signs of instability. These provide highly encouraging validation for the development of the all superconducting FASUM magnet (figure 83).

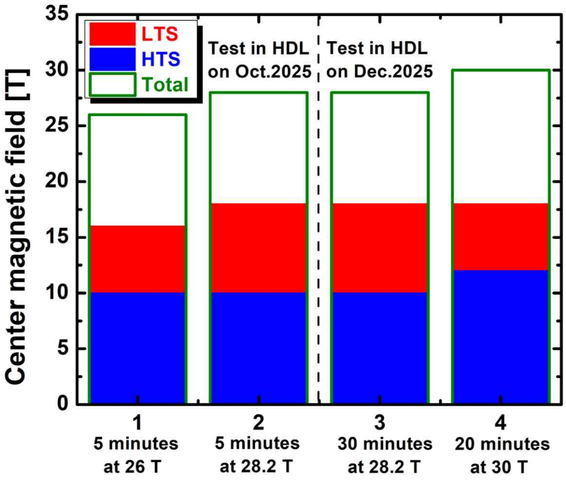

FIG. 82. *Magnetic-center fields of the NOUGAT HTS insert, the HLD LTS outsert, and the combined hybrid magnet during the Dresden tests.*

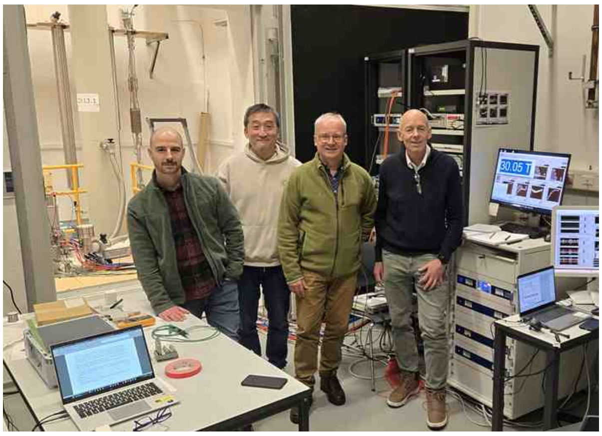

FIG. 83. *Celebratory photograph at HLD marking the attainment of 30 T with the HTS/LTS hybrid magnet.*

J. B. Song, H. Himanshu, R. Raison, J. Spitznagel, X. Chaud
F. Stacchi, T. de Chabannes, T. Lécrevisse, P. Fazilleau (DACM-IRFU-CEA, Université Paris-Saclay), T. Herrmannsdörfer (HLD-HZDR, Dreseden)

Magneto-Science

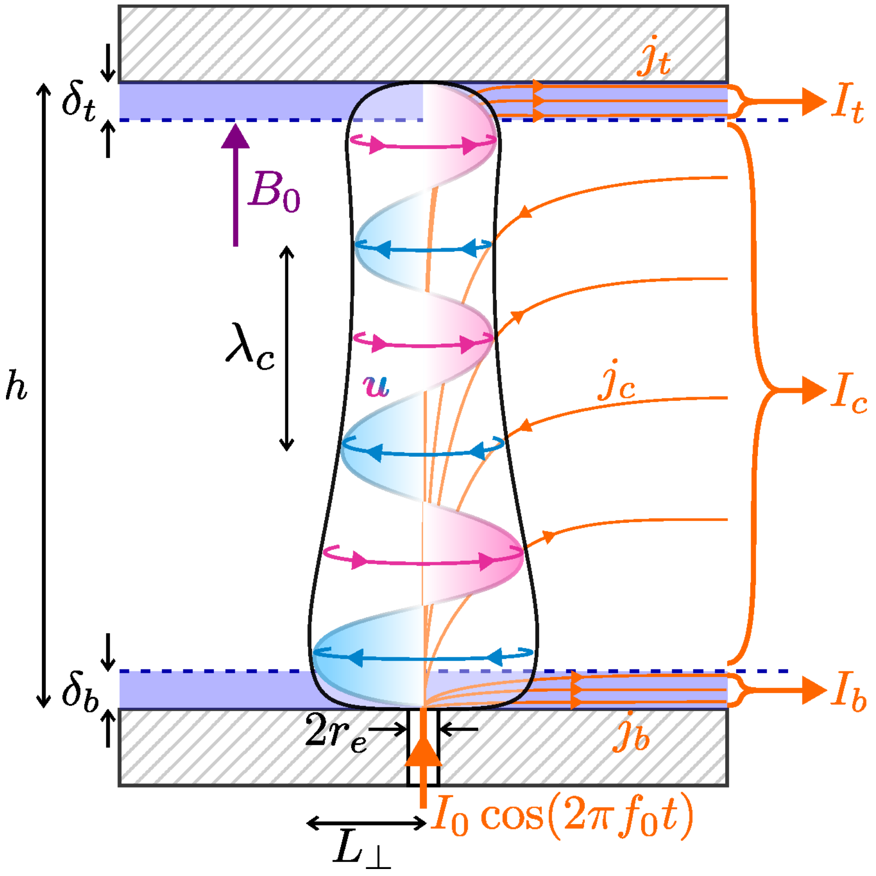

How Alfvén waves evolve with the transition from a Hartmann layer to a Stokes boundary layer

We have investigated the range of existence of magneto-mechanical waves –so called Alfvén waves– in liquid metal subjected to strong (up to 10 T), uniform and static magnetic fields. These waves, first theorised by Alfvén in 1942 [Alfven, Nature, 150 (1942)], were successfully generated during our previous campaign at the high field facility, thereby clarifying their propagation properties and damping [Lalloz *et al.*, J.Fluid Mechanics, 1003 (2025)]. In this previous work, Alfvén waves evolve in a closed cubic vessel (FLOWCUBE apparatus) filled with a Gallium alloy, into which an AC current of frequency f_0 and amplitude I_0 is injected at the bottom wall to drive the wave. Since no-slip conditions are considered at the walls, boundary layers must develop at the vicinity of these static, impermeable and electrically insulated walls. However the impact of the boundary layer on the Alfvén waves dynamics remains unclear. In the present study, we investigate to what extent the transition between two classic boundary layers (BL) –the Hartmann layer and the Stokes layer– can dramatically impact Alfvén wave propagation.

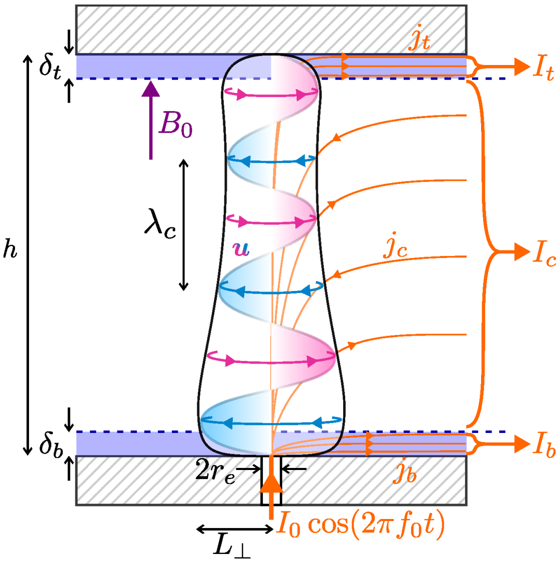

FIG. 84. *Illustration of a flow structure of wavelength* λ_c *evolving between two horizontal walls separated by a distance* h*, and under an axial, uniform and static magnetic field* $\boldsymbol{B}_0$*. The flow is driven by injecting at the bottom wall an AC current of amplitude* I_0 *and frequency* f_0*.* I_t *and* I_b *are the currents flowing in the top boundary layer (depth* δ_t*) and bottom one (depth* δ_b*), resp., while* I_c *denotes the current flowing in the core.*

Since the oscillating flow evolves in liquid metals (see figure 84 for illustration), any flow acceleration or velocity gradient gives rise to electric currents acting in return on the flow via the so-called Lorentz force (hereafter referred to MHD effects). At the boundaries, whether MHD effects are larger than flow acceleration or not, two different (BL) can develop; the Stokes layer (of depth δ_{St}), where acceleration balances viscous effects; the Hartmann layer (of depth δ_{Ha}), where MHD effects balance viscous effects. The transition between these two layers occurs when $\delta_{Ha}/\delta_{St} = 1$, while $\delta_{Ha}/\delta_{St} \propto f_0^{1/2} B_0^{-1}$.

By estimating the current contribution in the different parts of the fluid (*e.g.* the BLs and the core) we show that Alfvén waves cannot exist when Stokes layers are developed (*i.e.* at large frequencies) at the boundaries. In this case, the transverse to $\boldsymbol{B}_0$ components of the electric field $E_\perp$ at the bottom wall is expected to scale with $f_0^{1/2}$, which is recovered from simulations of the flow performed at different B_0 values (solid lines in figure 85). Electric fields measured at the bottom wall of FLOWCUBE through the use of electric potential probes and obtained from our last campaign are also consistent with the simulations (markers in figure 85).

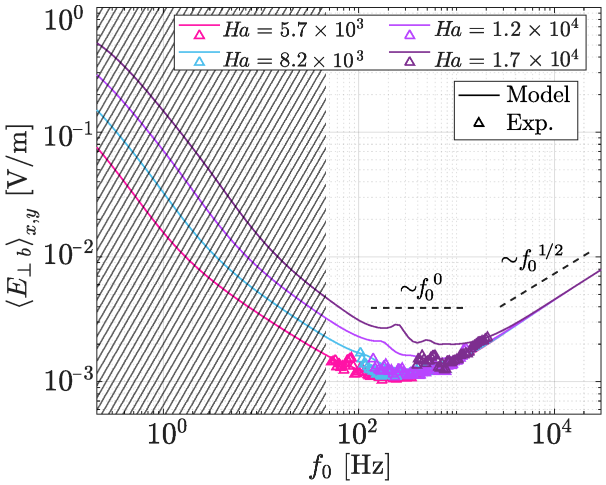

FIG. 85. *Amplitude of the transverse electric field at the bottom wall, spatially averaged in the transverse –to* $\boldsymbol{B}_0$*– directions* (x, y) *versus the forcing frequency* f_0*. Experiments (upper triangle markers) supported by simulations were carried out for four different Hartmann number* Ha*,* i.e *four different magnetic field intensity* B_0*.*

This new result reveals a strong constraint on the emergence of Alfvén waves, imposing a maximum frequency at a given magnetic field. It also suggests that data on Alfvén waves –often hard to access in natural environment– can be gathered directly from the related boundary layer.

F. Debray, J. Spitznagel
L. Davoust (SIMAP, INP-Grenoble), S. Lalloz, A. Potherat (Coventry University)

Quantitative observation of magnetic field accelerated phase transformation in an Fe-based alloy

Magnetic field effects on high temperature austenite (non magnetic) to ferrite (ferromagnetic) are investigated in Fe-1wt%Cu alloy by means of in-situ magnetic measurements at high temperature, using the combination of high temperature furnace in a superconducting magnet and a Faraday balance. We propose a new method to investigate the phase transformation process under magnetic field.

The magnetic field, together with temperature, significantly affects the mechanism of phase transformation, requiring detailed quantitative analysis. In this work, the influence of a magnetic field on the $\gamma - \alpha$ (austenite-ferrite) isokinetic phase transformation process of an Fe-1wt% Cu alloy was quantitatively analyzed through kinetics analysis by in-situ magnetization measurement.

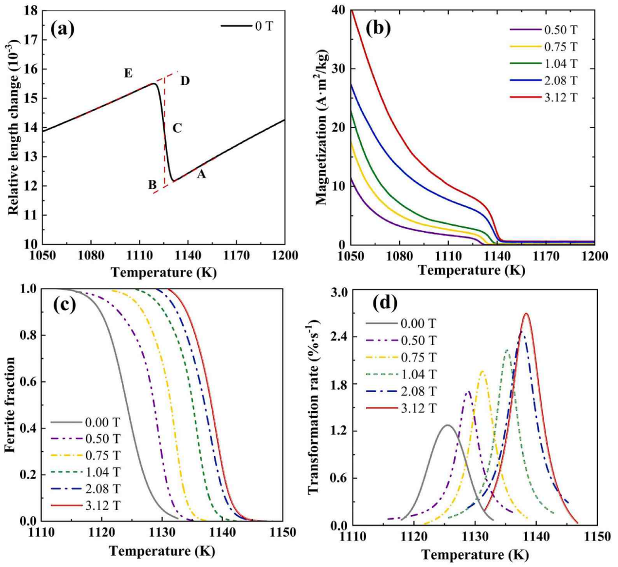

FIG. 86. *(a) Dilatometry curve of an Fe-1wt%Cu alloy without a magnetic field. (b) Magnetization curves of an Fe-1wt%Cu alloy measured at various magnetic fields. (c) Volume fraction curves and (d) transformation rate curves of an Fe-1wt%Cu alloy under different magnetic fields.*

The magnetic field effect on the austenite to ferrite transformation during a continuous cooling rate of 0.17 K/s is displayed in figure 86. The studied sample is a high purity Fe-1wt%Cu alloy, the transformation temperature in zero field as measured by dilatometry, (point C the figure 86(a)) is about 1125 K.

Figure 86(b) gives the magnetization curve of the sample in different magnetic fields during a constat cooling at 0.17 K/s. From these data, figure 86(c) gives the ferrite fraction during cooling in these different magnetic fields. Figure 86(d), as a derivative of figure 86(c), evidences the effect of an external magnetic field on austenite to ferrite transformation rate and equilibrium temperature. Two effects are clearly seen. A higher magnetic field (in this case up to 3.12 T) is shifting the equilibrium point to higher temperatures. In addition, the maximum transformation rate is increased. These effects can be explained by a thermodynamic effect of the magnetization of the material. A high magnetic field promotes the more magnetic field (ferromagnetic ferrite) versus the less magnetic phase paramagnetic austenite). The key point of this study are the in situ high temperature magnetization measurement.

Our detailed kinetic calculations reveal that the magnetic field accelerates the $\gamma - \alpha$ phase transformation, leading to shorter transformation time, increased transformation rate, and grain refinement. The Avrami equation, which describes how solids transform from one phase to another at constant temperature, can be used to calculate the kinetics of crystallization.

A quantitative analysis of the Avrami exponent, driving force, nucleation barrier and activation energy directly indicates that the magnetic field induces a shift from a site saturation nucleation mode to a continuous nucleation mode, increases the driving force of phase transformation. This reduces the nucleation barriers and activation energy, resulting in a higher nucleation rate, faster phase transformation rate, and more uniform and finer grain structure. Simultaneously, the magnetic field alters the impingement mode during iso-kinetic phase transformation, changing it from anisotropic growth impingement to randomly dispersed nuclei impingement.

More details concerning this work can be found in [Yan *et al.*, Journal of Alloys and Compounds **1020**, 179581 (2025)].

E. Beaugnon
Y. Yan, J. Wang, C. Wei, Y. He, W. Y. Wang, J. Li (State Key Laboratory of Solidification Processing, Northwestern Polytechnical University, Xi'an)

Dynamics and energy dissipation of collisional blast waves in a perpendicular magnetic field

This study experimentally investigates how a perpendicular magnetic field (up to 20 T) influences the dynamics and energy dissipation of laser-produced, collisional blast waves (BWs). Such waves are relevant to astrophysical phenomena (*e.g.*, supernova remnants) and magnetized inertial confinement fusion (ICF). The experiment has been conducted at the LULI2000 facility, a laser pulse (600 J, 1.5 ns) irradiates a graphite target, generating a blast wave in ambient air.

A magnetic field was produced using a Helmholtz coil, designed and built by in-house in the pulsed field facility, which generated a uniform field ranging from 0 to 20 T. For diagnostics, we employed Mach-Zehnder interferometry, 2D self-emission imaging, streaked optical pyrometry, and time-resolved optical spectroscopy. These techniques were used to measure electron density, temperature, and blast wave velocity.

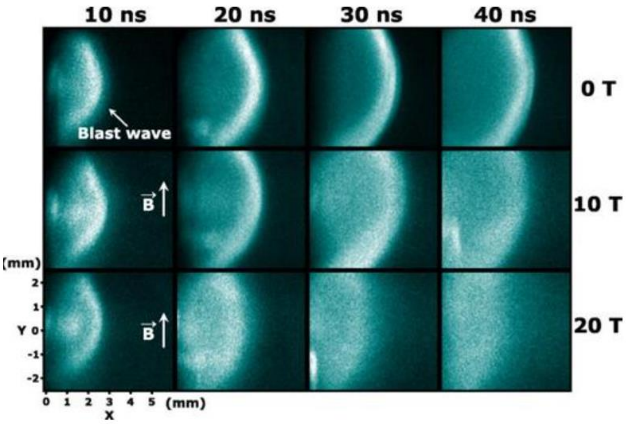

FIG. 87. *Example of 2D self emission of the blast wave plasma in the 580-850 nm wavelength range as a function of time and applied B-field. The target, a graphite pin is outside the field of view on the left of the images.The blast wave propagates in air (8 mbar).*

A typical example of data we obtained for 2D self emission is illustrated in figure 87 where one can see the influence of the B-field on the propagation of the blast wave in air. Our main observations are :

- (i) **Magnetic field impact**. The blast wave deviates from the Taylor-Sedov self-similar expansion solution under a magnetic field. Magnetic pressure increasingly dominates dynamic pressure, slowing and deforming the blast wave.
- (ii) **Super- to sub-magnetosonic transition**. The blast wave transitions from super-magnetosonic ($M_{ms} > 1$) to sub-magnetosonic ($M_{ms} < 1$), drastically altering its structure and energy dissipation.
- (iii) **Dissipation mechanisms**. Resistive diffusion and electron Hall effects are key dissipation mechanisms, while ambipolar diffusion and radiative losses are negligible in this regime.
- (iv) **Blast wave front width**. The front width increases with the magnetic field, indicating complex interactions between field compression and resistive diffusion.

The study demonstrates that magnetic fields significantly alter blast wave dynamics, offering insights for astrophysical plasma modeling and magnetized inertial confinement fusion.

For more details please see our recent publication [Triantafyllidis *et al.*, Physics of Plasmas **32**, 022102 (2025)].

J. Béard, J.M. Lagarrigue
A. Triantafyllidis , J.-R. Marquès, Y. Benkadoum, Y. De León, M. Koenig, B. Albertazzi (Laboratoire pour l'Utilisation des Lasers Intenses, LULI-CNRS, CEA, Sorbonne Universités, Ecole Polytechnique, Institut Polytechnique de Paris, Palaiseau), A. Ciardi (Sorbonne Université, Observatoire Paris, Université PSL, CNRS, Laboratoire d'Étude de l'Univers et des Phénomènes Extrêmes (LUX) Paris), A. Dearling (York Plasma Institute, University of York), N. Ozaki (Graduate School of Engineering, Osaka University)

Investigation of laser plasma instabilities driven by coupled high-power laser beams in magnetized underdense plasmas

Stimulated Brillouin scattering and stimulated Raman scattering (SBS and SRS) are instabilities that affect the propagation of high-power lasers in plasmas, and are particular important in the quest for inertial confinement fusion (ICF).

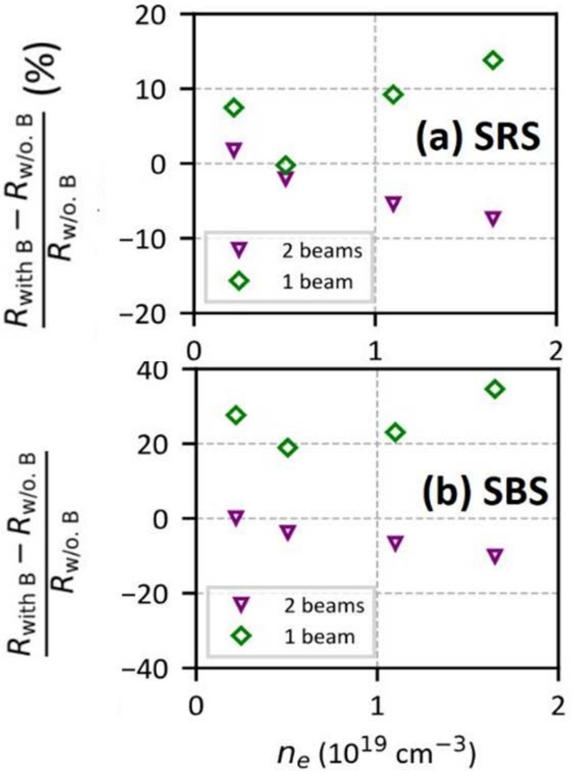

FIG. 88. *Experimental measurements of the variation of the reflectivities (R) of (a) backward stimulated Raman scattering and (b) backward stimulated Brillouin scattering (both normalized to the input laser energy), as function of the plasma electron density* n_e*, when magnetizing the plasma compared to the unmagnetized case. The vertical axis is the difference percentage in diode signals between the case with and without magnetic field, when using two laser beams (purple triangles) or just one beam (green diamonds). The error bars, calculated as the standard deviation of two to three shots per data point, are comparable to the size of the data points.*

They are further affected by cross-talk (CT) effects when multiple laser beams are simultaneously propagated in the plasma, as found in the schemes proposed for inertial confinement fusion.

We have developed a new theoretical model that allows us to evaluate the impact of cross-talk on stimulated Brillouin scattering and stimulated Raman scattering in low-density plasmas. Supported by experiments, we demonstrate that cross-talk can lead to a reduction of both stimulated Brillouin scattering and stimulated Raman scattering, due to the destabilization of the individually triggered instabilities (see figure 88).

We further demonstrate that this destabilization effect is accelerated by applying an externally magnetic field to the plasma, which is also beneficial for the hydrodynamics or fuel heating of inertial confinement fusion. By shedding new light on the promising scheme of magnetized inertial confinement fusion, our findings thus offer beneficial prospects for inertial confinement fusion.

Our model (to be detailed in an upcoming publication) combines fluid and kinetic assumptions. The kinetic aspect of the plasma, such as Landau damping, is crucial to have a good understanding of the stimulated Raman scattering and stimulated Brillouin scattering behavior.

The model considers the general case of the interaction of a single laser beam with a scattered wave, in the presence of a second laser beam, and of an external perpendicular magnetic field. Stimulated Raman scattering and stimulated Brillouin scattering are considered separately.

J. Béard
C.L.C. Lacoste, M. Bardon, E. D'Humières (CELIA, University of Bordeaux-CNRS-CEA, Talence), P. Antici (INRS EMT, Varennes), D. Oportus, I. Cohen, R. Lelievre, T. Waltenspiel, W. Yao, J. Fuchs (Laboratoire pour l'Utilisation des Lasers Intenses (LULI), CNRS-CEA-Ecole Polytechnique-Université Paris VI, Palaiseau), S.N. Chen (ELI-NP, "Horia Hulubei" National Institute for Physics and Nuclear Engineering, Bucharest-Magurele) F.P. Condamine (GenF, Elancourt, and The Extreme Light Infrastructure ERIC, ELI Beamines Facility, Dolnì Břežany)

Zeeman splitting in laser-produced magnetized blast waves

Understanding blast waves (BW) in the presence of a magnetic field is essential in numerous systems. For example, in astrophysics, the interaction between magnetic fields and low-density, collisionless shocks can influence the structure of the interstellar medium and the propagation of supernova remnants.

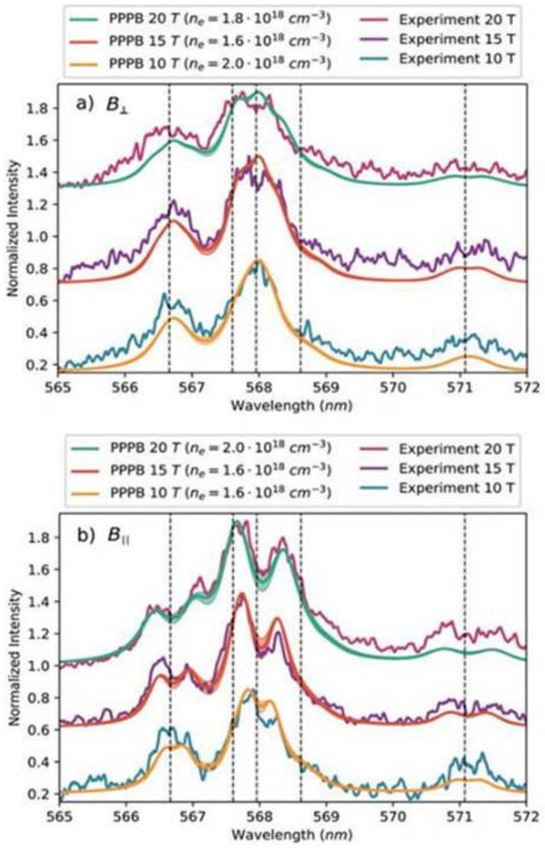

FIG. 89. *PPPB simulations for the NII transitions overlaid on time-integrated (over 50 ns) lineouts for 5, 10 and 20 T: (a) perpendicular and (b) parallel to the magnetic field orientation. Solid curves represent the values indicated in the legend, while the shaded areas correspond to simulations with* $\delta n_e = \pm 0.2 \times 10^{18} cm^3$ *relative to them (here, curves with higher intensities correspond to higher densities). The electron temperature is* $T_e = 5\,eV$ *for all simulated spectra. A linear background has been added to account for the bremsstrahlung emission of the plasma, and the spectra are normalized for each magnetic field and orientation. The dashed vertical lines correspond to the theoretical NII lines from NIST.*

This study focuses on observing the Zeeman effect in spectral lines emitted by a laser-produced, magnetized plasma to diagnose local magnetic fields (up to 20 T) and plasma conditions. Similarly to [Triantafyllidis *et al.*, Physics of Plasmas **32**, 022102 (2025)], the experiments were performed at the LULI2000 facility.

A laser pulse (600 J, 1.5 ns) generated a blast wave (BW) in air, while a controlled magnetic field ($0-20$ T) was applied. For diagnostics, high- and low-dispersion optical spectrometers were used to capture the emission lines of ionized nitrogen (NII) in the visible range ($563-574$ nm).

The PPPB code was employed in simulations to model the Stark-Zeeman line shapes, which were then compared with the experimental data. Our main observations are :

(i) Zeeman effect: A clear splitting of NII spectral lines in the presence of a magnetic field, with separation depending on field orientation (parallel or perpendicular to the line of sight) (see figure 89).

(ii) Magnetic field diagnosis: PPPB simulations determine the electron density ($n_e \simeq 1.6-2\times10^{18}\,cm^3$) and temperature ($Te \simeq 5$ eV), with a magnetic field precision of ± 2 T.

(iii) Resistive MHD regime: The magnetic Reynolds number ($Re_m \simeq 1$) indicates that the magnetic field diffuses into the plasma rather than being compressed.

These results highlight the profound influence of magnetic fields on blast wave dynamics, with implications for understanding astrophysical plasmas and magnetized ICF. Spectroscopic diagnostics and numerical simulations are crucial for interpreting these complex phenomena.

For more details please see [Triantafyllidis *et al.*, Matter Radiat. Extremes **10**, 047603, (2025)].

J. Béard, J-M. Lagarrigue
A. Triantafyllidis , J.-R. Marquès, Y. Benkadoum, Y. De León, M. Koenig, B. Albertazzi (Laboratoire pour l'Utilisation des Lasers Intenses, LULI - CNRS, CEA, Sorbonne Universités, Ecole Polytechnique, Institut Polytechnique de Paris, Palaiseau), A. Ciardi (Sorbonne Université, Observatoire Paris, Université PSL, CNRS, Laboratoire d'Étude de l'Univers et des Phénomènes Extrêmes, LUX, Paris), A. Dearling (York Plasma Institute, University of York), N. Ozaki (Graduate School of Engineering, Osaka University)

Grenoble axion haloscopes (GrAHal) for dark matter search

Two outstanding problems of particle physics and cosmology, namely the strong-CP problem and the nature of dark matter, can be solved by the discovery of a single new particle, the axion. This particle is supposed to be light and feebly interacting and Sikivie proposed in 1983 that it can be detected in the laboratory via photon conversion in a strong background magnetic field. Interestingly, all the required experimental tools are common to those generally used in condensed matter physics, *i.e.* RF cavities, ultra-low temperature, high magnetic field, low noise amplifiers ideally of quantum type. In this context, the modular high magnetic field and flux hybrid magnet platform, which was recently put in operation up to 42 T in 34 mm diameter [Pugnat et al., IEEE Trans. on Appl. Supercond. 36, 4300407 (2025)], offers unique opportunities for axion/axion-like particle search over a broad mass range using various Sikivie haloscopes (table VIII).

TABLE VIII. High magnetic field configurations of the hybrid magnet allowing axion dark matter search over a broad axion mass range. Nominal fields are indicated in parenthesis.

Field (T)	ϕ (mm)	ϕ_{RF} (mm)	f_{TM010} (GHz)	Axion mass (μeV)
42 (43)	**34**	**18.75**	**12.25**	**50.7**
- (40)	50	34	6.67	27.8
17.3 (17.5)	375	291	0.79	3.2
8.5 (9.5)	**812**	**675**	**0.34**	**1.4**

Focus was given first to axion dark matter search experiments using configurations of the hybrid magnet highlighted in bold in table VIII, namely 42 T in 34 mm diameter and 9 T in 812 mm (warm bores). A first experimental run was conducted up to 42 T using a beyond state-of-the-art RF-cavity based on high temperature superconductors (HTS). This cavity was developed and built with EuBaCuO layers extracted from Fujikura tapes. The measured quality factor Q_0 exceeds 600 000 without magnetic field, which is one of the highest values obtained worldwide with a HTS RF-cavity (more than 10 times larger than the value obtained with a high purity copper cavity). This RF-cavity was connected to the extremity of a dedicated instrumented probe prior to being inserted in a LHe cryostat for the 34 mm hybrid magnet. The test and measurement campaign was divided in two main parts. During the first one, focus was given to the precise characterization of the HTS RF-cavity around 12.251 GHz up to 42 T taking great care to not damaged it. The second part was dedicated to a first axion dark-matter search test around 12.251 GHz in 42 T field. Data analysis is currently in progress and will be released in 2026.

In parallel to the GrAHal-DMAG-HF activities, the design of the low frequency haloscope for the 300-600 MHz range (1-3 eV axion mass range) is being pursued for the large Cu RF-cavity [Pugnat et al., Phys. Sci. Forum **11**, 3 (2025)]. Progress has been achieved concerning the conception of the GrAHal-DMAG-LF cryostat and its integration within the hybrid magnet structure. The RF cavity of 675 mm diameter will be cooled down to 50 mK within the cryostat thanks to the connection to a first dilution refrigerator (figure 90). A second dilution refrigerator will be dedicated to the cooling to 100 mK of the RF electronic components, including the near quantum noise amplifier foreseen for the phase-2. A superconducting compensation coil is being designed for this phase with optimized current leads possibly based on HTS. All cryogenic parts will be developed Grenoble before onsite integration in the hybrid magnet. In 2025, complementary funding was secured within the LabEx QuantAlps equipment program (SUPERLINK proposal) to build the cryostat up to the 2-4 K thermal shield acting as the cold bed for the $\frac{1}{2}$m^3 volume hosting the Cu RF-cavity at 50 mK (figure 90). Thanks to the state-of-the-art 8.5 − 9.5 T superconducting outsert coil of the hybrid magnet, haloscopes with unprecedented sensitivity can be built, *i.e.* reaching the Dine-Fischler-Srednicki-Zhitnitskii (DFSZ) limit after only a few years integration time.

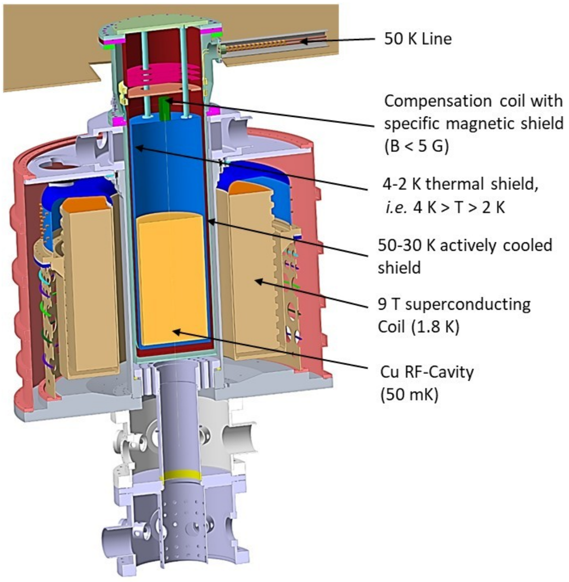

FIG. 90. *Integration of the GrAHal-DMAG-LF cryostat containing the Cu RF-cavity in the 9 T/812 mm warm bore configuration of the Grenoble hybrid magnet.*

H. Abir, R. Barbier, Y. Krupko, R. Pankow, M. Pelloux, R. Pfister, P. Pugnat, L. Ronayette R. Ballou, P. Camus, G. Donnier-Valentin, T. Grenet, J. Lacipière, P. Perrier, A. Talermin, J. Vessaire (Institut Néel, CNRS, University Grenoble Alpes), C. Smith (LPSC, CNRS, University Grenoble Alpes), D. Ahn, O. Kwon, Y. K. Semertzidis, S.W. Youn (IBS-DMAG, Daejeon)

Foil coil second version $N_{2(g)}$ Cotton-Mouton effect measurements

Recently a new Foil coil was designed to reduce acoustic noise that is the currently the main limiting factor for vacuum magnetic birefringence (BMV) measurement [Béard *et al.* Rev. Sci. Instrum. **92**, 104710,(2021)]. We can control the new Foil coil transverse magnetic field $\mathbf{B}_\perp(t)$ profile (figure 91) in short and medium length configuration by configuring the number of capacitor's used in the 3MJ generator, the full bank for a long shot (rise time $\simeq 6$ ms), half bank for a medium shot (4.3 ms) and quarter bank for a short shot (2.6 ms).

For a more in-depth understanding of what the Cotton-Mouton effect is and the basis for its prediction in a vacuum, and also how to measure it, we refer to [Agil *et al.* EPJ H **48**, 2,(2023)] and references therein.

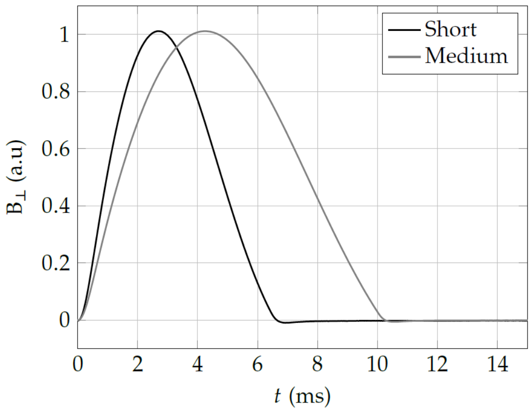

FIG. 91. *Foil coil magnetic field $\mathbf{B}_\perp(t)$ profile in short and medium pulse length configuration with a rise time of 2.6 and 4.3 ms respectively. We can adjust the rise time by adding or removing capacitors in the 3 MJ bank to control current delivery to the Foil coil.*

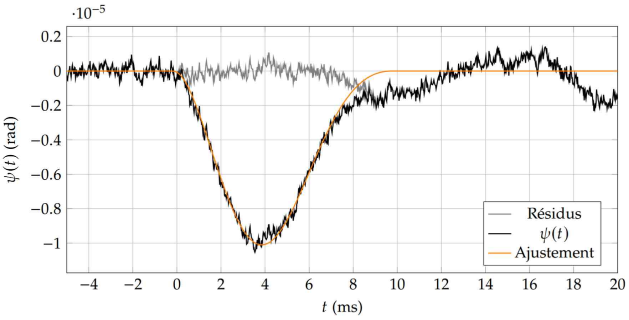

FIG. 92. *Ellipticity signal $\psi(t)$ measured (black) under a magnetic field amplitude of 4.5 T and a pressure 0.92 atmospheres, the fit (orange) gives $k_{CM}(P) = (-2.02 \pm 0.01) \cdot 10^{-13}$ T^{-2}. We represent residuals in gray.*

To calibrate the BMV aparatus we performed Cotton-Mouton effect measurements without an optical cavity in $N_{2(g)}$. An ellipticity signal $\psi(t)$ is shown figure 92 in medium shot length configuration for a magnetic field amplitude $B_\perp = 4.45$ T under $N_{2(g)}$ pressure $P = 0.92$ atmospheres.
Since the Cotton-Mouton produce a linear birefringence $\Delta n = n_e - n_o = k_{\mathrm{CM}} \mathbf{B}_\perp^2$, we can fit the measured ellipticity by $\psi = \frac{\pi}{\lambda} \sin(2\theta) \Delta n$, where λ is the laser wavelength, $\theta(\simeq 45^\circ)$ angle between $\mathbf{B}_\perp$ and linear polarization and k_{CM} is the Cotton-Mouton constant.

We measure $k_{\mathrm{CM}}(P)$ for different pressures, experimental result for a magnetic field amplitude of 4.5 T and a fit $k_{\mathrm{CM}}(P) = \Delta n_u P + b$ are shown figure 93.

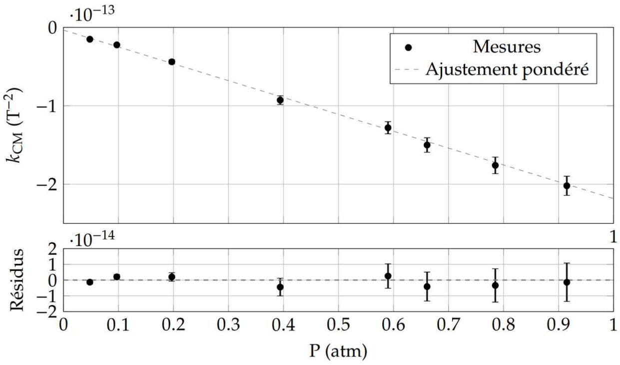

FIG. 93. *Fit for $k_{CM}(P) = \Delta n_u P + b$, where P is the nitrogen pressure. It gives $\Delta n_u = (-2.15 \pm 0.07) \cdot 10^{-13}$ $T^{-2} \cdot atm^{-1}$. Residuals are represented on the bottom.*

TABLE IX. Comparison of our measured value with other published values obtained using a Fabry-Perot cavity. Theoretical values calculated using two different calculus methods are given for $T = 293.15$ K for the Cotton-Mouton constant in $N_{2(g)}$ at $\mathbf{B}_\perp = 1$ T and $P = 1$ atmospheres.

Source	$\Delta n_u \cdot 10^{13}$, $P = 1$ atm, $B = 1$ T
Bregant *et al.* (2004)	(-2.17 ± 0.21) $T^{-2} \cdot atm^{-1}$
Mei *et al.* (2008)	(-2.02 ± 0.18) $T^{-2} \cdot atm^{-1}$
Berceau *et al.* (2012)	(-2.00 ± 0.10) $T^{-2} \cdot atm^{-1}$
This work	(-2.15 ± 0.07) $T^{-2} \cdot atm^{-1}$
MCSCF-GIAO	-2.20 $T^{-2} \cdot atm^{-1}$
MP2	-2.13 $T^{-2} \cdot atm^{-1}$

Our Cotton-Mouton results are compatible within uncertainty with theoretical values shown in table IX. We also have better accuracy and precision without an optical cavity, compared to published values made using an optical cavity. We have now made approximatively 500 shots in vacuum, at different magnetic field amplitude and rise times, using an optical cavity with a finesse around 400 000. An article providing a detailed analysis of these measurements will be published shortly.

E. Rodriguez Alvarez, J. Béard, T. Moraine, J. Billette, J.M. Lagarrigue, R. Battesti and C. Rizzo
J. Agil (Johannes Gutenberg-Universität Mainz)

Instrumentation

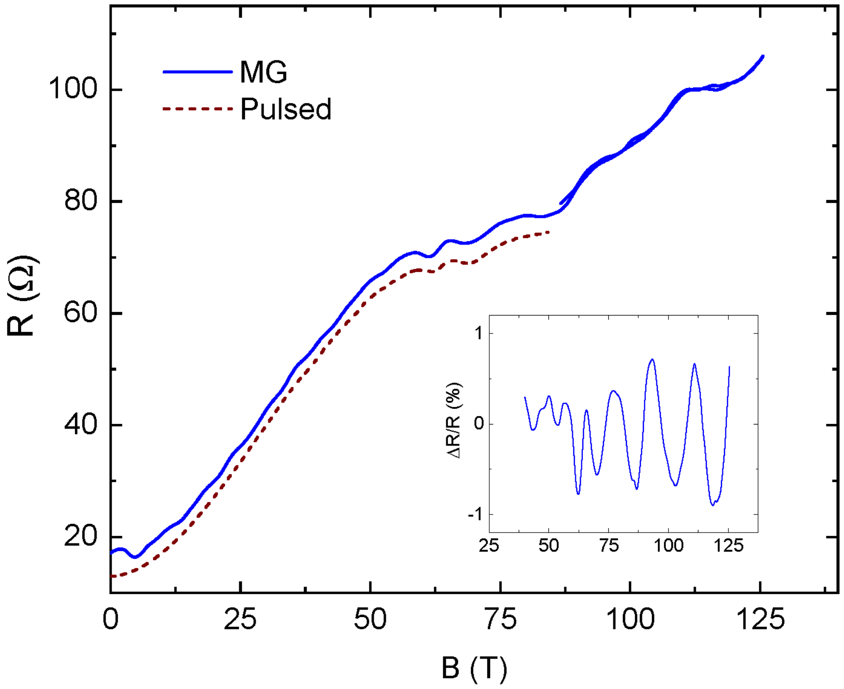

Millimeter-wave optical spectrometer for use in high-field resistive magnets

Many important quantum materials, such as unconventional superconductors and spin liquids, show interesting low-energy degrees of freedom which can couple to light, yet optical spectroscopy in the sub-THz range remains challenging. Conventionally, measurements in this frequency range are performed using time-domain techniques, where picosecond pulses of electromagnetic radiation are generated and detected in reflection and/or transmission. While time-domain spectroscopy has many advantages, including high speed, the possibility of phase-sensitive measurements, and good sensitivity, it is also difficult to use for materials with reflection coefficients close to one. Moreover, the latter include many bulk metallic and superconducting systems of interest, and a different approach is needed to perform high-sensitivity optical spectroscopy on such materials.

We have developed a continuous-wave sub-THz optical spectrometer that is uniquely suitable for highly reflective samples, but can also be used with insulators for studies of magnetic excitations [Rogić *et al.*, Rev. Sci. Instrum. **96**, 083101 (2025)]. Moreover, the instrument is compatible with high dc magnetic fields, and has been successfully tested in the 30 T resistive magnet in Grenoble.

The spectrometer combines two major components; a broadband source of millimeter-wave radiation, and a thermal detection setup designed for use at liquid helium temperatures. The radiation is obtained using a photomixer diode with two near-infrared laser inputs. The photomixer generates electromagnetic waves at a frequency that corresponds to the difference of the laser frequencies, and the latter can be tuned using a custom-made controller. We employ distributed-feedback laser diodes in the telecom wavelength range with a known wavelength temperature coefficient, which enables precise control of the laser wavelengths with temperature. The nominal ambient-temperature wavelengths are chosen in such a way that the full tuning range corresponds to photomixer output frequencies from zero to around 850 GHz, with a peak output power of $\simeq 200\,\mu$W at 100 GHz. The practical lower frequency limit is around 50 GHz, since the output power strongly decreases at lower frequencies. The frequency can be swept uninterrupted over the entire range, which enables high-resolution continuous-wave measurements.

In contrast to both time-domain and Fourier-transform spectrometers, the optical absorption coefficient of the sample is measured directly, through small sample temperature oscillations when the incoming radiation is chopped, *i.e.* the sample itself is employed as a bolometer. This technique is made possible by the use of a continuous-wave source, and enables extremely high relative sensitivities: the typical noise floor for measurements at 1.5 K and with cernox sensors on the sample is of the order of 1 pW, which gives a relative sensitivity better than 10^6 for the absorption coefficient.

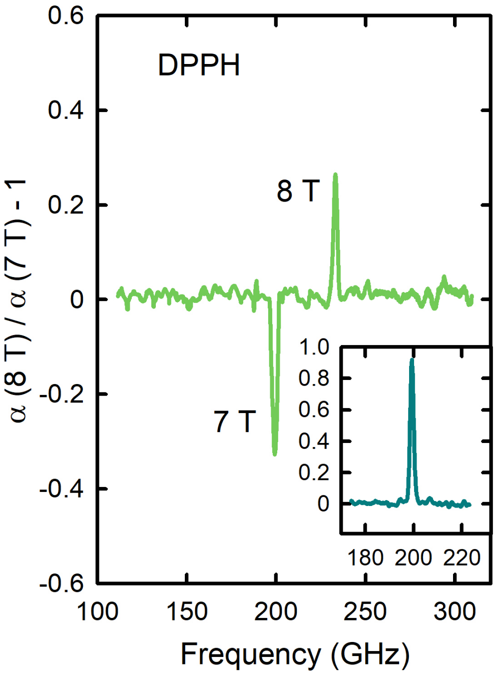

FIG. 94. *Electron spin resonance (ESR) measurements on the compound DPPH, using our novel millimeter-wave spectrometer in the resistive dc magnet. The main panel shows the ratio between sample absorption coefficients at 7 T and 8 T, with the resonances clearly visible. The insert shows a similar measurement in a superconducting magnet, which showcases the difference in signal-to-noise ratios.*

The spectrometer probe is designed to be compatible with narrow-necked cryostats, and we have performed tests in a 30 T resistive magnet, using electron spin resonance (ESR) to demonstrate both the frequency resolution and the sensitivity of the instrument. Figure 94 shows ESR measurements on a small single crystal of the reference free-radical compound 2,2-diphenyl-1-picrylhydrazyl (DPPH) performed at 1.5 K. The signal-to-noise ratio is somewhat worse than in a superconducting magnet (insert), but this test clearly demonstrates that the spectrometer can be used in high-field resistive magnets, and the instrument will be highly valuable in future studies of metallic and superconducting systems where time-domain spectroscopy is not feasible.

M. Orlita
N. Somun, L. Rogić, D. Pelc (Faculty of Science, University of Zagreb)

First observation of quantum oscillations by transport measurements in semi-destructive pulsed magnetic fields up to 125 T

High magnetic fields have proven instrumental in exploring the physical properties of condensed matter, leading to ground-breaking discoveries such as the quantum Hall effect in 2D heterostructures and quantum oscillations in cuprate superconductors. The ability to conduct precise measurements at progressively higher magnetic fields continues to push the frontiers of knowledge and enable new discoveries. In our work [Massoudzadegan *et al.* Rev. Sci. Instrum. **96**, 113904 (2025)], we present the development of a microwave technique for performing two-point transport measurements in semi-destructive pulsed magnetic fields (up to 125 T) and at low temperatures (down to 1.5 K) with unprecedented sensitivity leading to, notably, the first observation of Shubnikov-de-Haas oscillations in WTe_2 at magnetic fields beyond 100 T.

Detecting quantum oscillations (QO), which probe the topology of the Fermi surface of metals, is challenging because their amplitude strongly depends on temperature and is often small compared with the magnetoresistance background. A good signal to noise ratio is therefore essential. The detection of QO in the megagauss installation was possible due to the improvement in signal-to-noise. To reach that level of sensitivity, the setup was tested on various samples, including InAs and $La_{2-x}Sr_xCuO_4$. Here, we focus on measurements of the Weyl semi-metal WTe_2. Its Fermi surface consists of two pairs of electron-like pockets and two pairs of hole-like pockets, corresponding to quantum oscillation frequencies ranging from $F = 88\,T$ to $F = 158\,T$. The pockets are in the nested Russian-doll arrangement, allowing the observation of magnetic breakdown between pockets of the same sign, e.g. frequency combination.

Fig. 95 compares measurements in WTe_2 performed in the megagauss installation up to 125 T (semi-destructive mode 40 kV in blue) with data from the conventional pulsed field up to 86 T at $T = 20\,K$ (dashed wine). Note the reproducibility of the data at 40 kV during the rise above 88 T and the fall of the field pulse, which indicate a negligible heating in this field range. Furthermore, QO observed up to 86 T are in excellent agreement with measurements in the conventional pulsed field installation. However, comparing the amplitudes of QO allows to estimate heating of the sample at the beginning of the pulse to be about $\Delta T \approx 17\,K$. This value aligns well with our simple adiabatic model, which predicts $\Delta T \approx 18\,K$.

Despite the heating of the sample and due to the light effective mass of WTe_2, our setup enabled the observation of QO in the megagauss installation for a semi-destructive pulse. In the inset of Fig. 95, the oscillatory part of the signal up to $B = 125\,T$ is shown as a function of magnetic field. From a plot of position of maxima and minima of QO, we found two frequencies at approximately 450 T and 620 T. They originate from magnetic breakdown between the four main pockets and the 620 T oscillation was never observed before.

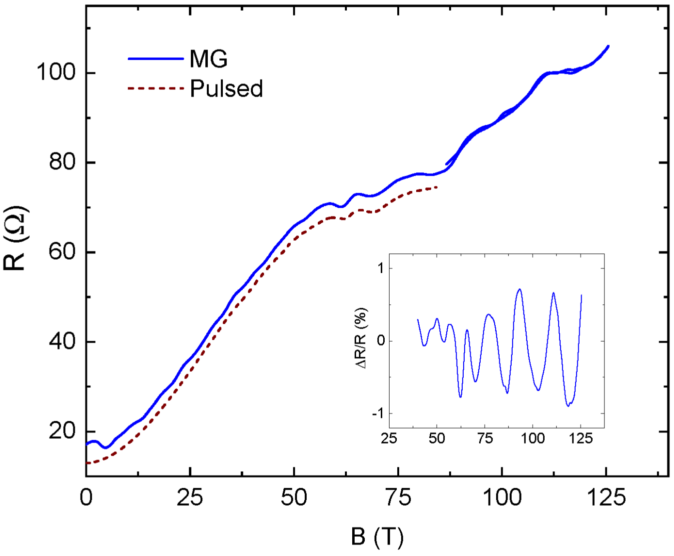

FIG. 95. *Measurement in the semi-destructive mode at 40 kV (solid blue line) showing quantum oscillations up to 125 T. The base temperature before the pulse was $T = 2.5\,K$. The dashed line corresponds to measurement in the conventional pulsed field at $T = 20\,K$ for comparison (the data are shifted for clarity). Note the reproducibility of the data at 40 kV during the rising field above 88 T and the falling field data. Data for the rising of the field below 88 T is too noisy to make a comparison because of the trigger noise. Inset: Quantum oscillations as a function of magnetic field with the spline background subtracted.*

In conclusion, we have reported the development of a transport measurement with an excellent signal to noise ratio in the megagauss installation, leading to the first observation of quantum oscillations in a megagauss experiment above 100 T. To reduce heating of the sample, work is in progress to reduce their size, in particular using the focusing ion beam technique. Our work paves the way for studying transport properties in quantum materials at fields up to 200 T in the megagauss facility.

M. Massoudzadegan, S. Badoux, N. Bruyant, I. Gilmutdinov, I. Haik-Dunn, G. de Oliveira Rodrigues, N. Lourenco Prata, A. Zitouni, M. Nardone, O. Drachenko, O. Portugall, D. Vignolles, C. Proust
B. Reulet (Institut Quantique, Sherbrooke), S. Wiedmann (HFML, Nijmegen), B.Fauqué (JEIP, Paris)

Commissioning of a dry cryostat enabling mechanical tests at cryogenic temperatures in the Institut Clément Ader facility

A cryostat, developed at the pulsed field installation, was delivered to the Institut Clément Ader site in February 2025.

The cryostat includes 2 Cryomech PT425-RM cold heads, a thermal anti-radiation screen and an experimental cell. The system uses the cooling power generated on the 1st and 2nd stages of the cold heads to cool the screen and the experimental cell, respectively. Helium gas introduced at a pressure of 1 bar into the cell prior cooling allows thermal coupling between the specimen and the copper cell. Fused silica windows were added to the experimental tank and the vacuum chamber in order to obtain images of the mechanical deformations throughout the tensile strength tests.

The system was integrated into a vertical tensile-compression test stand equipped with two articulated columns that can pivot to provide access to the cryostat's upper flange and allow for the loading of test specimens. The two cryo-coolers equipping the cryostat were connected to the electrical grid and to a chiller. User training was provided during a series of final cryogenic tests conducted on-site (see figure 96).

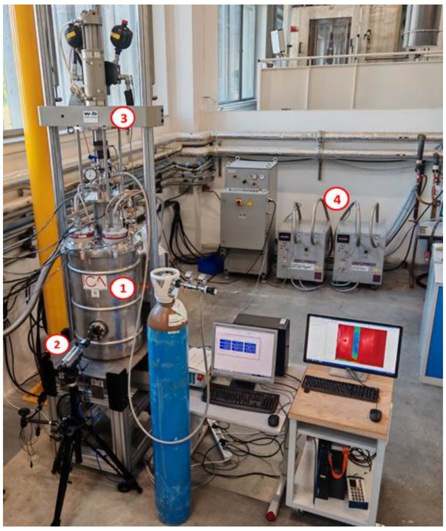

FIG. 96. *View of the system installed at the Institut Clément Ader, (1) cryostat, (2) CCD camera, (3) test stand, and (4) cryo-cooler compressors.*

In the second half of 2025, compression-tensile tests on polylactic acid (PLA) specimens enabled the development of the test stand control procedure. During the experiments, the deformation of the specimen is monitored, through the windows of the cryostat, by a CCD camera positioned outside the cryostat (see figure 97). The full-field displacement and strains on the specimen are determined using digital image correlation method.

The specimen is illuminated using two RL50 type light emitting diodes, which can operate at cryogenic temperatures and are placed inside the experimental chamber. This arrangement suppresses the need for a dedicated optical path through two additional windows thus greatly simplifying the cryostat construction.

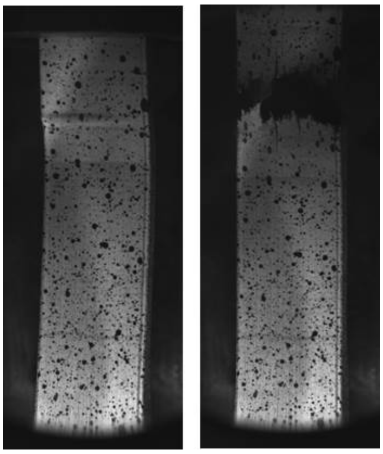

FIG. 97. *Compression-tensile test on PLA specimen.*

Tensile tests at 20 K on carbon fibre reinforced polymer (CFRP 8552As4 aero grade) specimens are currently underway (see figure 98). In the medium term, impact tests are also planned.

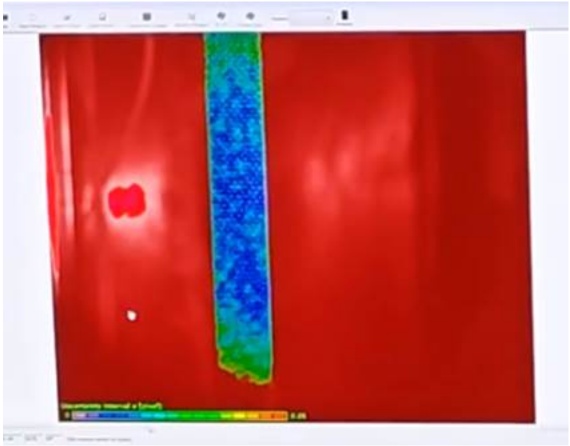

FIG. 98. *Digital image of carbon fibre reinforced polymer specimen during tensile test at 20 K.*

M. Nardone, A. Zitouni, M. Barragan, L. Bendichou, J-M. Lagarrigue, R. Martin
L. Narbonne, N. Laurien, S. Orieux, P. Navarro (Institut Clément Ader, CNRS, Université Toulouse III)

Magnet Development

Towards routine operation for science of the Grenoble hybrid magnet up to 42 T, as a first step

The highest DC magnetic fields are obtained today with hybrid magnets, *i.e.*, from magnets combining superconducting and water-cooled Cu-alloy resistive technologies. The Grenoble hybrid magnet, which is now entering in operation phase, is a modular user platform providing the various high DC magnetic field and flux configurations summarized in table X enlarging the scientific discovery potential. In 2024, the resistive inserts of the hybrid magnet were connected to the recently upgraded 12 + 18 MW electrical power installation and successfully commissioned as a first step, up to 42 T in 34 mm diameter [Pugnat *et al.*, IEEE Trans. on Appl. Supercond. **36**, 4300407 (2025)]. In 2025, three scientific preselected experiments were successfully performed up to 42 T requiring the installation of dedicated cryogenic setups like the one shown in figure 99 and compatible with other resistive magnet sites. The hybrid magnet operation in 2025 was ended by a fully dedicated field quality measurement campaign to investigate dynamic effects.

TABLE X. Possible magnetic field and flux configurations of the hybrid magnet together with commissioned field values. Magnetic fields reached are shown without parenthesis. Electrical power is for the resistive coils (helix+Bitter), water cooling (pumps) and cryogenics (He liquifier, 1.8 K pumps and cryoplant ancillaries) respectively.

B(T) (nominal)	Warm ϕ (mm)	Hybrid magnet configuration	Electrical power (MW)
42(43)	34	14 helix + 2 Bitter + SC	20.7 + 2.8 + 0.4
34(35)	34	14 helix + SC	10.6 + 1.1 + 0.4
17.3(17.5)	375	2 Bitter + SC	10.9 + 1.1 + 0.4
8.5(9.5)	812	SC only	0.4

The magnetic field profile at the center for a nominal field obtained by ^{27}Al NMR at 42 T was found to follow the relation,

$$B(x,y,z) = B_0(1 - G_{z2}(z^2 - \tfrac{1}{2}(x^2 + y^2))),$$

with the precisely determined NMR magnetic field $B_0 = 41.885$ T and $G_{z2} = 18$ ppm/mm^2. The second-order gradient term G_{z2} is a about 20% lower than typical values found in the 24 MW purely resistive magnets containing only Bitter and polyhelix magnets. This is due to the highly homogeneous superconducting outsert that provides $\simeq$ 20% of the total magnetic field at 42 T. The short time magnetic field fluctuations at 42 T recorded by 100 single scan ^{27}Al NMR experiments during 17 minutes exhibit a standard deviation $\sigma = 5$ ppm. Using a 3σ criterium for the peak-to-peak amplitude of the fluctuations, their value is given by 15 ppm. This value about 25% lower than in purely resistive magnets. Since their origin is mostly due to ripples induced by the power supplies, the large inductance of the superconducting magnet acts as a filter that partly reduces these fluctuations. Another element that can reduce fluctuations is the low temperature eddy-current shield between the superconducting and resistive part of the magnet. For the long-term drift, a value of 15 ppm was found after one hour at 42 T that did not change during the entire experiment time of 6.5 hours at 42 T. These values are typical high field magnets and can be explained by temperature variations in the water-cooling circuit for the resistive magnets.

In summary, the field homogeneity and field stability of the Grenoble hybrid magnet at 42 T are perfectly suitable for solid state physics NMR experiments, one of the most demanding experimental requirements. Unfortunately, the first scientific experimental campaign with the Grenoble hybrid magnet had to be interrupted prematurely because of the pollution of the LHe circuit with H_2, jeopardizing the turbines of the fully dedicated He liquefier. The superconducting magnet was warmed-up to 100 K before to proceed with the depollution of all the stored He and be ready for the next cool down beginning of 2026 for the continuation of the science campaign up to 42 T. Dedicated investigations were launched, the origin of the problem identified and mitigating measures will be implemented.

FIG. 99. *User platform of the 42 T hybrid magnet showing the xy-table which supports a ^{4}He bath cryostat with a ^{3}He insert and NMR probe. Vacuum tubes for ^{4}He and ^{3}He bath pumping are also visible. The magnetic field center is $\simeq$ 1.8 m below the wooden platform. The cold bore diameter is 16 mm for a room temperature magnet bore diameter of 34 mm. As seen, the cryostat is raised by about 1 m with respect to its position during scientific experiments.*

H. Abir, R. Barbier, J. Chastagnier, F. Debray, C. Grandclément, S. Krämer, Y. Krupko, K. Payot, R. Pfister, P. Pugnat, L. Ronayette
F. Molinié (CEA-Saclay, Gif-sur-Yvette)

Expected maximum DC field with the Grenoble hybrid magnet

The highest DC magnetic field produced today with a user magnet 45.22 T in a 32 mm warm bore aperture using 26.9 MW electrical power. It was obtained in August 2022 with the hybrid magnet of the Chinese Academy of Sciences in Heifei. It is worth noting that reducing the diameter of the warm bore has a significant impact on the expected maximum magnetic field strength. Assuming the Fabry relation with the same electrical power or considering the same limiting Hoop stress at the internal radius for the resistive insert of the Grenoble hybrid magnet, a field strength of 42 T in a 34 mm warm bore corresponds to about 43 T in 32 mm.

The main argument for the 42 T limitation of the hybrid magnet comes from detailed calculations for the polyhelix insert that give a maximum von Mises stresses of 480 MPa for a total magnetic field of 43 T with 25.5 T provided by the polyhelix (figure 100). The current polyhelix is made from cold spray process with CuAg5% alloy have a significant temperature dependent yield stress (YS) with values of 495 MPa at 100°C and 460 MPa at 150°C [Tardieu et al., Magnetochemistry **10**, 15, (2024)]. As the peak temperature was calculated within these temperature range (figure 101), it was decided not to try to exceed 42 T with the present polyhelix, giving the priority perform first scientific experiments up to 42 T instead of trying to further increase the magnetic field.

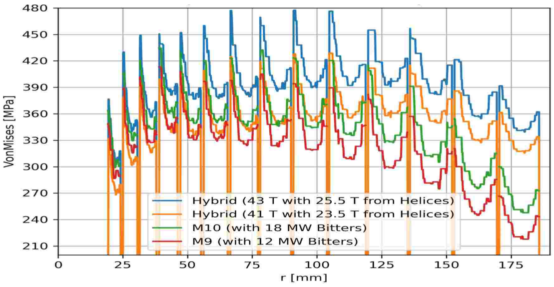

FIG. 100. *Calculated von Mises stress for the polyhelix coil insert for various configurations.*

Two main developments are being pursued to reach higher magnetic field values in the near future; (i) increasing the magnetic field produced by resistive inserts, mostly from the polyhelix coils, and (ii) by pushing the magnetic field produced by the superconducting coil [Pugnat *et al.*, IEEE Trans. on Appl. Supercond. **36**, 4300407 (2025)]. Thanks to the increase of the water-cooling flow and to the use of a new Cu-Ag alloy grade, polyhelix inserts can be expected to produce at least 26.5 T central field. An important first step in this direction will be made end of 2025 and beginning of 2026 with the test of the new polyhelix insert in CuAg10% alone up to 39 T. If successful, the enhanced cooling design will be applied to the polyhelix insert of the hybrid magnet. Due to the higher constraints encountered by polyhelix insert in the hybrid magnet configuration (the background magnetic field increases from 12 T to 17.5 T), the new copper silver alloy grade will be tested on the most critical helix to enhance the YS by 10% without decreasing the electrical conductivity. As a consequence, magnetic field of 43 T in a 34 mm diameter bore could be then reached with a 10% margin on the constraints allowing to perform long duration experiments at this field value.

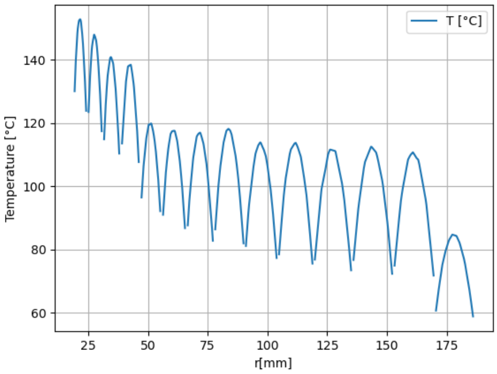

FIG. 101. *Calculated temperature distribution in the polyhelix insert of the hybrid magnet at 45 T.*

Concerning the superconducting outsert, a sufficient margin exists for the critical current density of the RCOCC not to limit the maximum field that can be produced which is limited by the mechanical stress. The YS measured on stabilizer samples in CuAg0.05% hollow profile are larger than 290 MPa at 4.2 K allowing to reach at least a central magnetic field of 10 T with 33% of margin. Additional margins are coming from the soft-soldering of the Rutherford cable as well as from the selection of double-pancakes during their stacking to locate conductors with the highest YS in the most stressed parts of the coil.

The extreme scenario in case of severe short-circuit in Bitter coils has been revised and has validated that the hybrid magnet is well suited for inserts of power levels reaching 36 MW. This suggest that the magnetic field of the hybrid can pushed beyond 45.5 T in a 34 mm warm bore aperture. Further detailed FEM calculations are required to fully validate this statement. As a function of the results of the operation at 42 T and 43 T, together with dedicated additional computations of the mechanical stresses, it will be decided if higher magnetic fields can be reached without damaging components of the hybrid magnet.

F. Debray, O. Jay, R. Pfister, P. Pugnat, L. Ronayette, C. Trophime
F. Molinié (CEA-Saclay, Gif-sur-Yvette)

How can participation be introduced into the energy modelling process implemented in the European FlexRICAN project?

As part of the European project FlexRICAN (Flexibility in research infrastructures for global carbon neutrality), which aims to study energy flexibility within European research infrastructures (figure 102), a modelling of the energy systems of these infrastructures is currently underway. During this study, the question arose as to whether groups or individuals who may impact the system or be impacted by it should be included in the modelling. This inclusion during the modelling phase is termed participatory modelling [Étienne *et al.* (2010)] [Voinov *et al.* (2016)].

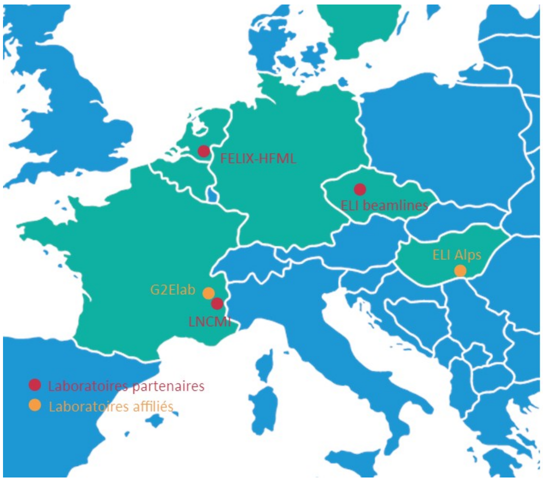

FIG. 102. *Partner research infrastructures modelled within the FlexRICAN framework.*

As part of the flexrican project, a study was lunched to investigate the potential of participatory modelling. This study had 2 main objectives; (i) to review the state of the art on participatory modelling of energy systems and (ii) to adapt and test an existing participatory modelling framework at the various consortium RIs : ELI Beamlines in the Czech Republic, ELI Alps in Hungary and HFML in the Netherlands.

Three tools were used for participation:

- **Semi-structured interviews**. Interviews with one user of the facilities, one operator and one manager for each laboratory (8 in total) using a qualitative rather than quantitative approach.
- ***Rich Picture***. Respondents were asked to represent their dream vision of flexibility within their infrastructure as shown in figure 103.
- ***Rebound Archetype***: Participatory workshop created by [Bornes (2024)] to see the rebound effects of an intention. Aim to analyze the behaviour of actors in a participatory context.

As a result, the literature review highlights five conditions necessary for successful participatory modelling: (i) The objective of the modelling must be clear to everyone, well defined, and the process must be legitimate; (ii) The actors involved in the participatory exercise must be diverse; (iii) There must be a climate of trust and transparency throughout the process; (iv) Financial, material, human and time resources must be available to everyone; (v) Use a method adapted to the socio-cultural context.

The analysis of the feasibility of including participation in the various research infrastructures is summarized in the Table below.

TABLE XI. *Table showing validation (✓) or non-validation (×) of the laboratories visited in terms of the conditions necessary for the proper conduct of participatory processes highlighted in the literature. Condition (v) is not shown because it relates to the implementation of the participatory process, whereas this study is based on a prospective analysis.*

Conditions	ELI BL	ELI Alps	HFML
(i)	×	×	✓
(ii)	×	×	✓
(iii)	✓	✓	✓
(iv)	×	×	✓
Total	×	×	✓

This analysis paves the way for a similar study currently underway at LNCMI-Grenoble. The results of the study will also be disseminated to FlexRICAN partners as well as external stakeholders (other research infrastructures and industrial partners). In addition, the application of participatory methods in the modelling currently underway at HFML is under consideration.

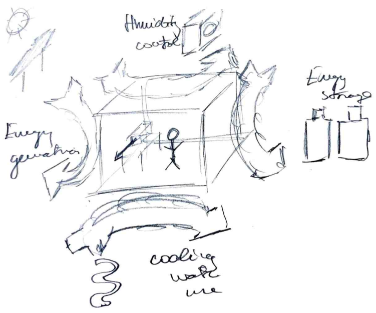

FIG. 103. *Example of Rich Picture drawn by a participant*

E. Coquemont, F. Debray, N.K. Twum-Duah, B. Vincent, S. Valla
S. Hodencq (G2Elab, Grenoble)

LNCMI-Grenoble energy consumption mediation tools

As part of a student project during the PISTE (Pour une Ingénierie Sobre Techno et Eco-responsable) semester at Grenoble INP, tools for mediating the laboratory's energy consumption were developed and tested. Semi-structured interviews revealed that consumption and its economic and environmental consequences were poorly understood within the LNCMI-G's. So, these tools were created with the aim of raising awareness among laboratory staff about the infrastructure's energy consumption.

The first tool was the creation of an awareness poster, which was put up in January 2025 in the M9 and M10 magnet handling rooms. The poster shows the orders of magnitude of electrical consumption, economic and environmental costs for one hour of use of resistive magnets. These orders of magnitude are illustrated with real-life examples to avoid them being abstract. For example at 36T, the cost is 10 000 €/h, 1560 kgCO_2eq/h equivalent to the power consumption of a city of approximately 100 000 inhabitants.

FIG. 104. *Photo from the exhibition In The Box visually representing the laboratory's energy consumption.*

The second tool was an exhibition held in January in the lobby of LNCMI (figure 104). The aim was to represent the LNCMI-Grenoble's electricity consumption with a real-life bar chart using cardboard boxes. The stacks of cardboard boxes represent, in order, the annual consumption of an average French person, 10 houses of 120 m^2 for 4 people, a village of 580 inhabitants, the consumption of resistive magnets and the consumption of the LNCMI-G. It can be seen that the last two stacks are almost equivalent, highlighting the fact that almost all of the laboratory's 10 GWh of annual consumption is due to resistive magnets.

Finally, the last tool created is a participatory workshop where participants try to find solutions to critical events in 2025 and 2050. As shown in figure 105, events can be internal, such as in 2050 when a large part of the staff will have to be replaced due to retirement, or they can be external, such as flooding of the Drac river or a surge in helium prices. This workshop therefore places the LNCMI-G in its economic, social and environmental context.

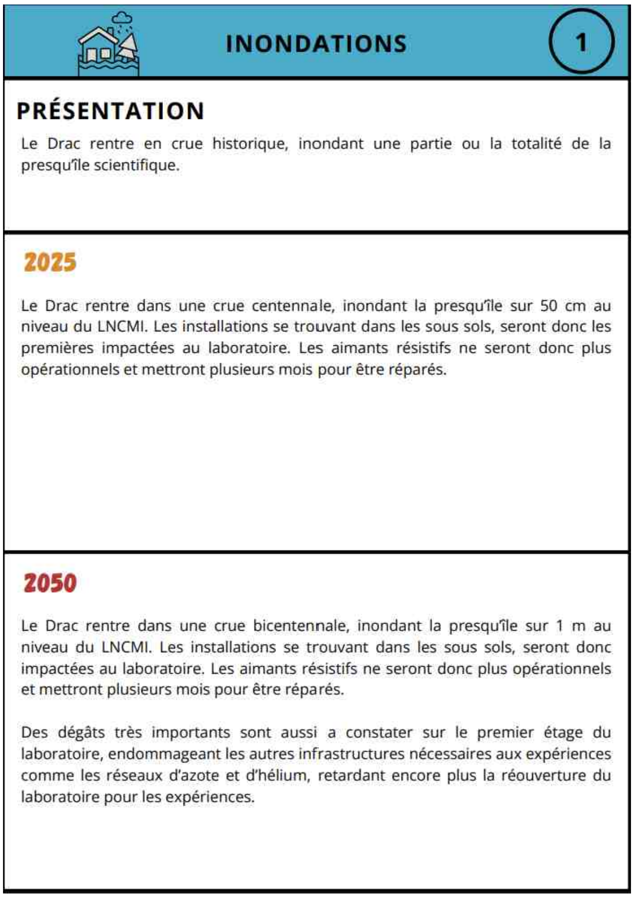

INONDATIONS 1

PRÉSENTATION

Le Drac rentre en crue historique, inondant une partie ou la totalité de la presqu'île scientifique.

2025

Le Drac rentre dans une crue centennale, inondant la presqu'île sur 50 cm au niveau du LNCMI. Les installations se trouvant dans les sous sols, seront donc les premières impactées au laboratoire. Les aimants résistifs ne seront donc plus opérationnels et mettront plusieurs mois pour être réparés.

2050

Le Drac rentre dans une crue bicentennale, inondant la presqu'île sur 1 m au niveau du LNCMI. Les installations se trouvant dans les sous sols, seront donc impactées au laboratoire. Les aimants résistifs ne seront donc plus opérationnels et mettront plusieurs mois pour être réparés.

Des dégâts très importants sont aussi a constater sur le premier étage du laboratoire, endommageant les autres infrastructures nécessaires aux expériences comme les réseaux d'azote et d'hélium, retardant encore plus la réouverture du laboratoire pour les expériences.

FIG. 105. *Workshop flood card. Participants have to find solutions to the critical event*

For more information, please consult [Coquemont, Garnier, Harison et Laumond (2025)] which explains the approach and the creation of the tools.

E. Coquemont, F. Debray, R. Raison, B. Vincent
S. Hodencq (G2Elab, Grenoble)
A. Garnier, S. Harison, V. Laumond (Grenoble-INP, Université Grenoble Alpes)

Development of a 120 T non-destructive pulsed magnet

The laboratory routinely provides users with access to pulsed fields ranging from 60 to 90 T and performs coil replacement. Alongside this service activity, we pursue the development of a 120 T nondestructive pulsed magnet in the framework of the QMAHT project. After establishing a European record for non-destructive magnets in 2017, with a peak field of 98.8 T, the we have attempted again in 2025 to achieve 100 T using a triple-coil magnet system. This time, it was possible to reach 96 T (figure 106) while performing transport measurements above 90 T, providing new insights for researchers.

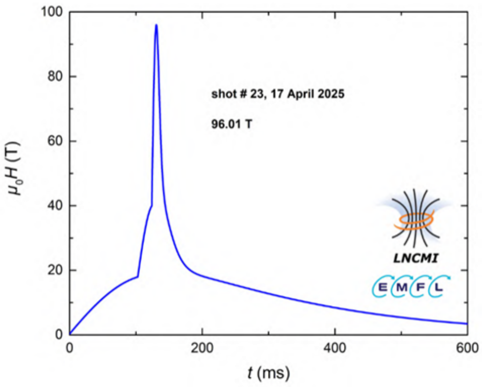

FIG. 106. *The 96 T pulse achieved by the LNCMI Toulouse in April 2025. The inner coil was damaged on the subsequent shot.*

Although the mid-coil was damaged in 2017, it survived the tests carried out in 2025 and has been definitively validated at a field slightly higher than its nominal field.

Currently we are working on a new four coil magnet design. We have performed mechanical and thermal studies on the critical 120 T inner coil. To sustain the Lorentz forces and, as the stress increases with radius, different wire sections have been integrated in the inner coil to optimize the stress distribution. The simulations were performed with COMSOL in a quasi-static model. We obtain (figure 107) a uniform stress distribution between the four conductor layers, and the hoop stress remains below 4 GPa (a reasonable value for the stress exerted on the Zylon fiber for such a small coil).

Additionally, we must use conductors with high mechanical strength to build high-field magnets, but the higher the strength, the lower the conductivity, so we have to deal with materials with higher resistivity than pure copper. It is therefore necessary to ensure that the temperature during the pulse does not become critical and that there is no risk of overheating the wire. We decided to build a thermal model on COMSOL to evaluate the heating in the conductor during the pulse, including magneto-resistance (MR) and the skin effect in our calculations. The MR was measured with a copper sample perpendicular to the field axis and up to 50 T for 3 different temperatures. With these data, we could implement our model and visualize heating within the inner coil in each layer (figure 108). At the end of the pulse, the maximum temperature reached is 317 K. Our goal is to use this thermal model to optimize the wire sections and get a uniform temperature profile across the four layers of conductor to increase the coil efficiency. One way to do this is to increase the current density when the heating is below the reasonable value of 300 K by adapting the conducting part of the copper-stainless steel composite wire cross-section.

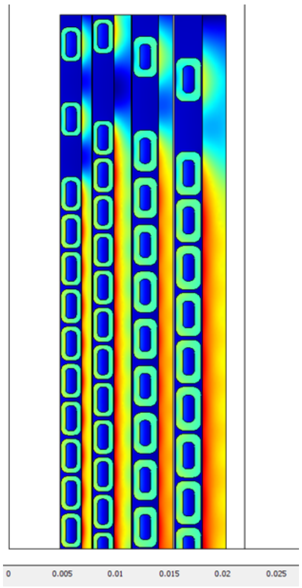

FIG. 107. *COMSOL color plot of hoop stresses in the small coil. This model simulates the coil subjected to a magnetic field of 110 T, reaching 3.9 GPa (red color).*

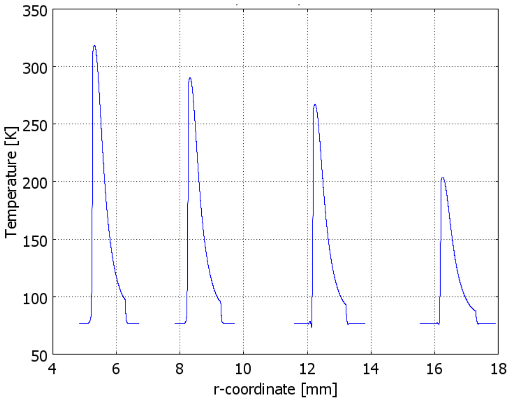

FIG. 108. *COMSOL simulation of the temperature variation on each conductor layer of the small coil. The decreasing heating is mostly due to a low MR as we move away from the field axis, which results in a loss of efficiency.*

J. Béard, J. Billette, J-M. Lagarrigue, T. Lemaire, T. Moraine, E. Noël

Development of copper-tungsten composite wires using cold spray and wire-drawing for high magnetic field application

Cold spray using recycled helium is a suitable additive manufacturing method for depositing copper alloys. Nevertheless, it cannot effectively spray composite powders made of micron-sized Cu and nanometric tungsten because shock waves prevent the finest W particles from reaching the substrate. To overcome this, the feasibility of spraying Cu powder coated with a 100 nm W layer was studied. The Cu powder (figure 109(a)), produced by high-pressure gas atomization, consists of spherical particles (15-45 μm). It was then coated with W using fluidized-bed CVD, without altering particle size or causing agglomeration. The coated powder shows a uniform black appearance (figure 109(b)) and EDS analysis indicates a W content of 1.8%wt.

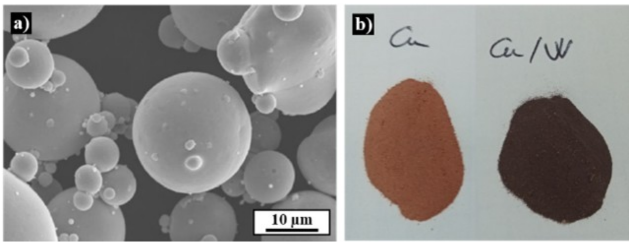

FIG. 109. *Scanning electron microscope image of Cu powder (15-45 μm), (b) Photograph of Cu powder (15-45 μm) before and after W coating.*

The W-Cu powder was cold-sprayed onto an Al substrate, with each vertical pass depositing about 150 μm of material at a flow rate of 106 g/min. The final deposit formed a trapezoidal prism measuring large base: 30 mm, small base; 13 mm, height; 23 mm, length; 50 mm.

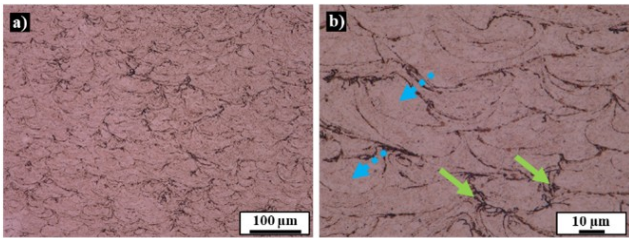

FIG. 110. *Optical microscopy images of the cold spray deposit. Solid arrows indicate highly deformed zones and dashed arrows show slightly deformed zones. In the image, Cu appears in orange and W in black.*

Optical microscopy (figure 110) reveals a typical cold-spray microstructure; heavily deformed, hardened zones with refined grains, and larger grains in the less-deformed particle cores. Coating each Cu particle with W provides a very uniform dispersion of the nanometric second phase throughout the deposit. W-Cu cylinder with diameter $D = 8$ mm, and length $L = 50$ mm was cut from the cold spray deposit. This cylinder was wire-drawn at room temperature without breaking, through conical tungsten-carbide dies in approximately 50 passes, progressively reducing the diameter down to 0.2 mm.

The W-Cu wires exhibit a very good compromise between high ultimate strength (604-757 MPa at 77 K) and low electrical resistivity (95.8% IACS at 293 K; 0.30-0.33 $\mu\Omega$cm at 77 K), as shown in figure 111. The strengthening of this composite conductors comes from the combination of nano-structuring induced by wire drawing, Cu/W interfaces, the presence of a second phase at the nanometric scale and the high velocity of the deposited particles that leads to high initial deformation rates. In addition, the use of large Cu grains allows the preservation of large areas of pure Cu, which makes it possible to maintain low electrical resistivity.

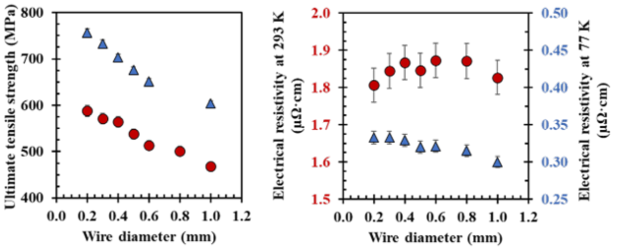

FIG. 111. *Ultimate tensile strength versus wire diameter and electrical resistivity versus wire diameter at 293 K (closed circles, left axis) and 77 K (closed triangles, right axis) for present wires.*

This method made it possible to produce W-Cu wires without breakage. The wires show very low electrical resistivity and a decent ultimate tensile strength, even if not yet at the level of the most advanced high-strength conductors. This initial result is promising, especially since several parameters such as powder particle size distribution can still be optimized. Overall, the findings provide useful guidelines for developing ultra-strong, highly conductive W-Cu wires for advanced scientific and industrial applications.

For more details please see [Tardieu et al., IEEE Transactions On Applied Superconductivity (2025):10.1109/TASC.2025.3626202].

S. Tardieu, N. Ferreira, F. Teyssier, T. Schiavo, F. Lecouturier-Dupouy
C. Verdy (ICB-LERMPS-UTBM, Belfort)

Mechanical and microstructural changes in Cu single-turn coils revealing the effect of high-speed pressurization, deformation and heating during Megagauss field generation

We have investigated the effect of very high-speed deformation on copper single-turn coils (STC) using Vickers microhardness measurements, in order to identify the mechanical and microstructural signatures of rapid deformation. This approach aims to provide quantitative and reproducible data on the local evolution of the copper mechanical properties in poorly understood regimes, and to contribute to the understanding of the mechanisms activated under dynamic conditions.

The Vickers microhardness measurement on raw single turn coil (figure 112) shows a symmetric parabolic profile across its thickness (3 mm), with higher hardness at both the inner and outer surfaces (105 $HV_{0.1}$) and a minimum at mid-thickness (90 $HV_{0.1}$). This distribution reflects the bending process; the outer surface undergoes tensile deformation and work hardening, the inner surface experiences compressive deformation, and the neutral axis at the center shows minimal change, retaining the initial material hardness.

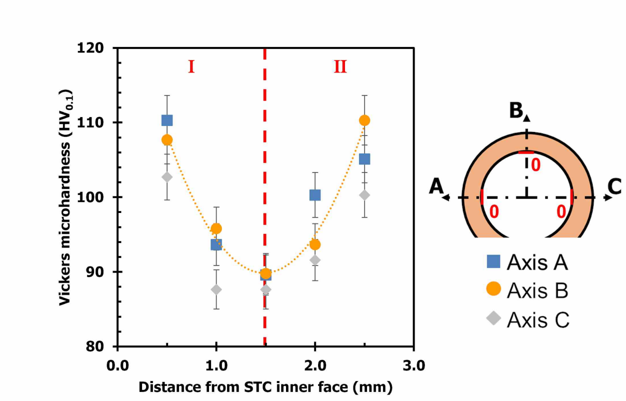

FIG. 112. *Vickers microhardness versus radial position across the "raw coil" thickness (0 mm corresponding to the inner face, 3 mm to the outer face). The dotted line marks the neutral fiber. Zone I: compression; Zone II: tension.*

The magnetic field (50 T) generated under operating conditions of 15 kV and 750 kA induces, according to simulations, a surface temperature exceeding 2000 K, a current density above 100 MA/mm^2, and a pressure greater than 1 GPa. The coil undergoes rapid deformation within a few microseconds: its inner diameter expands by 6%, while the outer diameter changes only slightly (1.3%) due to the stiffening effect of an external stainless-steel ring. At the same time, the coil thickness decreases by about 7.8%, indicating significant axial compression. These fast dimensional changes correspond to a high strain rate of about $1.4 \times 10^4\,\mathrm{s}^{-1}$, characteristic of dynamic loading conditions.

A comparison between the coil that generated a non-destructive 50 T pulse and the raw coil (figure 113(a)) shows a significant drop in microhardness near the inner surface, falling from above 100 $HV_{0.1}$ to lower values. Matching these measurements with thermal simulations (figure 113(b)) indicates that this reduction is caused by strong, localized heating from the skin effect, which anneals and softens the inner region. The outer zones remain cooler but undergo high compressive stresses from Lorentz forces, leading to plastic deformation and work hardening that raise the microhardness to about 115 $HV_{0.1}$.

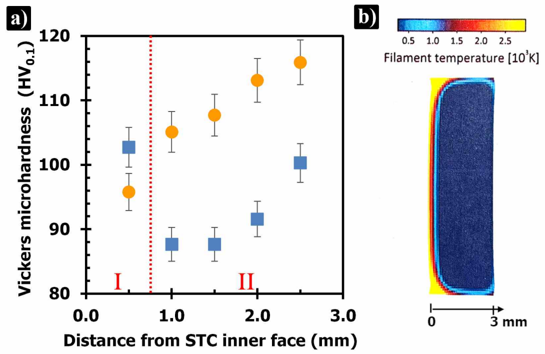

FIG. 113. *(a) Vickers microhardness versus radial position across the coil thickness for raw single turn coil (closed squares) and after an intermediate field generation (closed circles). Zone I: Annealing (≃ 2500 K); Zone II: Work hardening. (b) Simulated temperature distribution within the single turn coil during non-destructive magnetic field generation.*

This work demonstrates the feasibility of using local hardness measurements to assess mechanical and thermal effects in pulsed high-field experiments. Further microstructural characterization (EBSD, SEM or TEM) is planned to investigate possible modifications of the copper microstructure induced by these extreme conditions.

For more details please see [Tardieu et al., IEEE Transactions On Applied Superconductivity (2025):10.1109/TASC.2025.3619454].

S. Tardieu, N. Ferreira, F. Teyssier, T. Schiavo, O. Drachenko, O. Portugall, F. Lecouturier-Dupouy

Scale-up of silver-copper composite wires by spark plasma sintering and room temperature wire-drawing

To produce precursors for wire drawing, cylindrical samples were fabricated using spark plasma sintering (SPS). The initial cylinders, 8 mm in diameter and 30 mm in length, could be drawn successfully without rupture. Until now, the small size of samples produced by SPS has limited their application in magnets. To address this, we are scaling up the production process. The primary challenge is ensuring that macroscopic properties remain consistent with initial specifications during the upscale. Larger cylinders with a diameter of 24 mm and a length of 30 mm were therefore produced. Despite numerous trials, these larger samples could not be drawn without breaking. Since SPS is particularly well suited for producing pellet-type samples that are wider than they are tall, the precursor geometry was then modified. Rectangular bars measuring $10 \times 10 \times 100\,\text{mm}^3$ were fabricated (figure 114), effectively reducing the sample height by a factor of three. With this new geometry the samples were drawn successfully without rupture.

FIG. 114. *Photograph of the 8 mm diameter SPS cylinder and its die (right), the $10 \times 10 \times 100\,mm^3$ SPS bar and its die (bottom left), the SPS die for future $20 \times 20 \times 100\,mm^3$ samples (top left).*

Ag nanowires (30μm long, 200 mm in diameter) were produced at CIRIMAT and blended with commercial Cu powder (1μm particles) to obtain a composite containing 1 vol.% Ag. The so-obtained powder was then heated at 180°C under a hydrogen atmosphere, allowing surface Cu oxide to be reduced and the powder to partially consolidate into a cohesive pre-sintered material suitable for SPS processing. Approximately 80 g of this powder is required to fabricate a rectangular bar precursor. SPS consolidation was carried out at 400°C under 25 MPa for 5 minutes. The resulting bar was subsequently cold-drawn to 0.2 mm in diameter. Mechanical and electrical characterizations were performed on wires with diameters between 0.2 and 1.3 mm (figure 115). The resulting Cu wires showed ultimate tensile strength values in the range of 662-883 MPa, with electrical resistivities of $0.33 - 0.38\mu\Omega$cm at 77 K. These results are close to those obtained from wires produced from 8 mm SPS. The scaled-up Ag-Cu wires exhibit ultimate tensile strengths between 853 and 1170 MPa and electrical resistivities of $0.46 - 0.51\mu\Omega$cm at 77 K. These values are comparable to those measured on Ag-Cu wires obtained from 8 mm SPS cylinders produced with the same route.

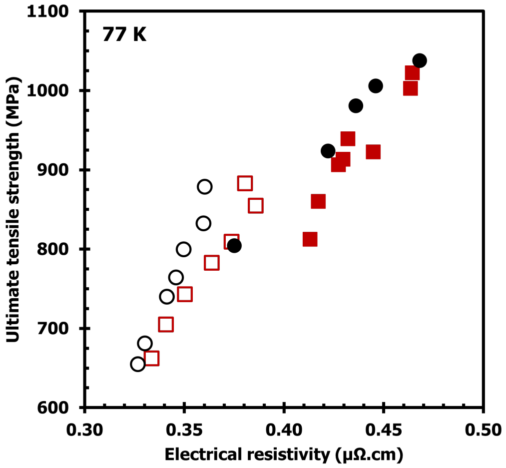

FIG. 115. *Ultimate tensile strength versus electrical resistivity at 77 K for wires obtained from Cu SPS cylinder (open circles), 1Ag-Cu SPS cylinder (closed circles), scaled-up Cu SPS bar (open squares), scaled-up 1Ag-Cu SPS bar (closed squares).*

The combination of well-established processing steps, enables the fabrication of Ag-Cu composite wires that simultaneously exhibit high electrical conductivity and high mechanical strength. The comparable results obtained for both Ag-Cu and pure Cu demonstrate that the SPS-based scale-up route remains robust and reliable, with mechanical and electrical performance effectively maintained across different precursor sizes. Building on these successful scale-up trials, the next step will consist in producing larger SPS precursors in the form of $20 \times 20 \times 100\,\text{mm}^3$ bars (figure 114), requiring approximately 300 g of powder.

For more details please see [Tardieu et al., IEEE Transactions On Applied Superconductivity **35**, 6900204 (2024)].

S. Tardieu, J. Béard, F. Teyssier, N. Ferreira, T. Schiavo, F. Lecouturier-Dupouy
D. Mesguich, A. Lonjon, A. Weibel, C. Laurent (CIRIMAT, CNRS-UPS-INP, Toulouse) G. Chevallier, C. Estournès (Plateforme Nationale CNRS de Frittage Flash, Toulouse)

PhD theses 2025

1. Lou-Anne Veyrat de Lachenal
   Développement d'un dispositif de mesure de la chaleur spécifique d'un gaz d'électrons bidimensionnel dans le régime Hall quantique
   Doctorat de l'Université Grenoble-Alpes
   Thése soutenue le 2 juillet 2025

2. Katarzyna Posmyk
   Determination of the exciton fine structure in two-dimensional metal-halide perovskites
   Doctorat de l'Université de Toulouse en cotutelle avec Wrocław University of Science and Technology, Poland
   Thése soutenue le 27 novembre 2025

List of Publications 2025

---

[1] Langit Cahya Adi, Maxime Aragon-Alberti, Jérôme Rouquette, Geert L. J. A. Rikken, Cyrille Train, Jérôme Long, and Matteo Atzori, "Coexistence of room temperature magneto-chiral dichroism and magneto-electric coupling in a chiral nanomagnet," Nanoscale **17**, 1954–1958 (2025).

[2] Hamid Pashaei Adl, Christoph Bennenhei, Marti Struve, Paulina Peksa, Mateusz Dyksik, Michal Baranowski, Kok Wee Song, Moritz Gittinger, Christoph Lienau, Jonas K. König, Jamie M. Fitzgerald, Naga Prathibha Jasti, Falk Eilenberger, Paulina Plochocka, Ermin Malic, Oleksandr Kyriienko, Martin Esmann, and Christian Schneider, "Tunable Room-Temperature Polaritons in the Very Strong Coupling Regime in Quasi-2D Ruddlesden-Popper Perovskites," Adv. Optical Mater. **13**, e01392 (2025).

[3] Munkhtuguldur Altangerel, Quentin Barthélemy, Étienne Lefrançois, Jordan Baglo, Manel Mezidi, Gaël Grissonnanche, Ashvini Vallipuram, Emma Campillo, Anne Forget, Dorothée Colson, Ruixing Liang, D. A. Bonn, W. N. Hardy, Cyril Proust, and Louis Taillefer, "Thermal Hall conductivity in the strongest cuprate superconductor: Estimate of the mean free path in the trilayer cuprate $HgBa_2Ca_2Cu_3O_{8+\delta}$," Physical Review B **112**, 014522 (2025).

[4] D. Aoki, Y. Homma, H. Harima, and I. Sheikin, "Quasi-two-dimensional Fermi surfaces of the antiferromagnet U_2RhIn_8 revealed by de Haas–van Alphen measurements," Physical Review B **111**, 035155 (2025).

[5] Maxime Aragon-Alberti, Hadrien Flichot, Mathieu Gascoin, Boris Le Guennic, Olivier Cador, Ghenadie Novitchi, Geert L. J. A. Rikken, Cyrille Train, Fabrice Pointillart, and Matteo Atzori, "Magneto-Optical Readout of a Chiral Single-Molecule Magnet at Telecom Wavelengths," J. Am. Chem. Soc. (2025), 10.1021/jacs.5c17544.

[6] Matteo Atzori and Alessandro Lunghi, "Optical control of spin states in magnetic molecules," Trends in Chemistry **7**, 413–416 (2025).

[7] Nathan Aubergier, Vincent T. Renard, Sylvain Barraud, Kei Takashina, and Benjamin A. Piot, "Wide Electrical Tunability of the Valley Splitting in a Doubly Gated Silicon-on-Insulator Quantum Well," Nano Lett. **25**, 13557–13562 (2025).

[8] Seul-Ki Bac, Florian Le Mardelé, Jiashu Wang, Mykhaylo Ozerov, Kota Yoshimura, Ivan Mohelský, Xingdan Sun, Benjamin A. Piot, Stefan Wimmer, Andreas Ney, Tatyana Orlova, Maksym Zhukovskyi, Günther Bauer, Gunther Springholz, Xinyu Liu, Milan Orlita, Kyungwha Park, Yi-Ting Hsu, and Badih A. Assaf, "Probing Berry Curvature in Magnetic Topological Insulators through Resonant Infrared Magnetic Circular Dichroism," Physical Review Letters **134**, 016601 (2025).

[9] M. Bialek, Y. Todorov, K. Stelmaszczyk, D. Szwagierczak, B. Synkiewicz-Musialska, J. Kulawik, N. Palka, M. Potemski, and W. Knap, "Hybridization of Terahertz Phonons and Magnons in Disparate and Spatially-Separated Material Specimens," Adv. Funct. Mater. **35**, 2416037 (2025).

[10] D. J. Campbell, M. Frachet, V. Oliviero, T. Kurosawa, N. Momono, M. Oda, J. Chang, D. Vignolles, C. Proust, and D. LeBoeuf, "Impact of low-energy spin fluctuations on the strange metal in a cuprate superconductor," Nature Physics **21**, 1759 (2025).

[11] Chang-woo Cho, Timothée T. Lortz, Kwan To Lo, Cheuk Yin Ng, Shek Hei Chui, Abdel Rahman Allan, Mahmoud Abdel-Hafiez, Jaemun Park, Beopgil Cho, Keeseong Park, Noah F. Q. Yuan, and Rolf Lortz, "Evidence for orbital Fulde-Ferrell-Larkin-Ovchinnikov state in the bulk limit of $2H\text{-}NbSe_2$," Nature Communications **16**, 7599 (2025).

[12] Daniel Delony, Arnd Fitterer, Martin Diefenbach, Florian Wätjen, Sandipan Maji, Serhiy Demeshko, Matthias Otte, Milan Orlita, Vera Krewald, Max C. Holthausen, and Sven Schneider, "Evaluating Spin-Orbit Effects on the Thermochemistry of Proton-Coupled Electron Transfer," Inorg. Chem. (2025), 10.1021/acs.inorgchem.5c05144.

[13] Caitlin Duffy, "Lessons in support," Physics World **38**, 19 (2025).

[14] Mateusz Dyksik, Michal Baranowski, Joshua J. P. Thompson, Zhuo Yang, Martha Rivera Medina, Maria Antonietta Loi, Ermin Malic, and Paulina Plochocka, "Steric Engineering of Exciton Fine Structure in 2D Perovskites," Advanced Energy Materials **15**, 2404769 (2025).

[15] J. Dzian, P. Kubaščík, S. Tázlarů, M. Białek, M. Šindler, F. Le Mardelé, C. Kadlec, F. Kadlec, M. Gryglas-Borysiewicz, K. P. Kluczyk, A. Mycielski, P. Skupiński, J. Hejtmánek, R. Tesař, J. Železný, A.-L. Barra, C. Faugeras, J. Volný, K. Uhlířová, L. Nádvorník, M. Veis, K. Výborný, and M. Orlita, "Antiferromagnetic resonance in $\alpha-$MnTe," Physical Review B **112**, 024433 (2025).

[16] Yuchen Fu, Hugh Lohan, Marcello Righetto, Yi-Teng Huang, Seán R. Kavanagh, Chang-Woo Cho, Szymon J. Zelewski, Young Won Woo, Harry Demetriou, Martyn A. McLachlan, Sandrine Heutz, Benjamin A. Piot, David O. Scanlon, Akshay Rao, Laura M. Herz, Aron Walsh, and Robert L. Z. Hoye, "Structural and electronic features enabling delocalized charge-carriers in $CuSbSe_2$," Nature Communications **16**, 65 (2025).

[17] L. Heinze, T. Kotte, R. Rausch, A. Demuer, S. Luther, R. Feyerherm, E. L. Q. N. Ammerlaan, U. Zeitler, D. I. Gorbunov, M. Uhlarz, K. C. Rule, A. U. B. Wolter, H. Kühne, J. Wosnitza, C. Karrasch, and S. Süllow, "Atacamite $Cu_2Cl(OH)_3$ in High Magnetic Fields: Quantum Criticality and Dimensional Reduction of a Sawtooth-Chain Compound," Physical Review Letters **134**, 216701 (2025).

[18] Nico Huber, Ivan Volkau, Alexander Engelhardt, Ilya Sheikin, Andreas Bauer, Christian Pfleiderer, and Marc A. Wilde, "Fermi surface and magnetic breakdown in PdGa," Physical Review B **112**, 085116 (2025).

[19] Teresa Insinna, Anne-Laure Barra, and Clare P. Grey, "Overhauser Dynamic Nuclear Polarization of Lithiated Graphite Anodes: Probing Bulk and Surface Structures," Chem. Mater. **37**, 5167–5182 (2025).

[20] Ivan Jakovac, Tonči Cvitanić, Denis Arčon, Mirta Herak, Dominik Cinčić, Nea Baus Topić, Yuko Hosokoshi, Toshio Ono, Ken Iwashita, Nobuyuki Hayashi, Naoki Amaya, Akira Matsuo, Koichi Kindo, Ivor Lončarić, Mladen Horvatić, Masashi Takigawa, and Mihael S. Grbić, "Properties of an organic model $S = 1$ Haldane chain system," Physical Review B **111**, 064407 (2025).

[21] Dipankar Jana, Swagata Acharya, Milan Orlita, Clement Faugeras, Dimitar Pashov, Mark van Schilfgaarde, Marek Potemski, and Maciej Koperski, "Deconstruction of the Anisotropic Magnetic Interactions from Spin-Entangled Optical Excitations in van der Waals Antiferromagnets," Adv. Sci. , e05834 (2025).

[22] Dipankar Jana, Diana Vaclavkova, Rajesh Kumar Ulaganathan, Raman Sankar, Milan Orlita, Clement Faugeras, Maciej Koperski, M. E. Zhitomirsky, and Marek Potemski, "Strong and selective magnon-phonon coupling in the van der Waals antiferromagnet $CoPS_3$," Physical Review B **112**, 165427 (2025).

[23] Jakub Jasiński, Joakim Hagel, Samuel Brem, Edith Wietek, Takashi Taniguchi, Kenji Watanabe, Alexey Chernikov, Nicolas Bruyant, Mateusz Dyksik, Alessandro Surrente, Michal Baranowski, Duncan K. Maude, Ermin Malic, and Paulina Plochocka, "Quadrupolar excitons in $MoSe_2$ bilayers," Nature Communications **16**, 1382 (2025).

[24] Alexander Kazakov, Valentine V. Volobuev, Chang-Woo Cho, Benjamin A. Piot, Zbigniew Adamus, Tomasz Wojciechowski, Tomasz Wojtowicz, Gunther Springholz, and Tomasz Dietl, "Topological phase diagram and quantum magnetotransport effects in (Pb,Sn)Se quantum wells with magnetic barriers (Pb,Eu)Se," Physical Review B **111**, 245419 (2025).

[25] T. Klein, C. Marcenat, A. Demuer, J. Sarrade, D. Aoki, and I. Sheikin, "Exotic magnetic phase diagram and extremely robust antiferromagnetism in Ce_2RhIn_8," Physical Review B **111**, L201110 (2025).

[26] W. Knafo, T. Thebault, S. Raymond, P. Manuel, D. D. Khalyavin, F. Orlandi, E. Ressouche, K. Beauvois, G. Lapertot, K. Kaneko, D. Aoki, D. Braithwaite, and G. Knebel, "Incommensurate Antiferromagnetism in UTe_2 under Pressure," Physical Review X **15**, 021075 (2025).

[27] R. Komar, A. Lopion, K. Mosina, A. Söll, Z. Sofer, W. Pacuski, C. Faugeras, P. Kossacki, and T. Kazimierczuk, "The polarization switching in nanoscale with an anisotropic 2D magnetic semiconductor," Solid State Communications **397**, 115798 (2025).

[28] Yulia E. Kovalenko, Michael V. Yakushev, Vladimir I. Grebennikov, Vladimir A. Golyashov, Vyacheslav V. Marchenkov, Milan Orlita, Yuri S. Ponosov, Evgeniy I. Patrakov, Svetlana G. Titova, Robert W. Martin, Konstantin A. Kokh, Oleg E. Tereshchenko, and Tatyana V. Kuznetsova, "Electronic, magneto-optical, and magnetotransport properties of the topological insulator Sb_2Te_2Se," Phys. Rev. B **112**, 245114 (2025).

[29] Yulia E. Kovalenko, Michael V. Yakushev, Vladimir I. Grebennikov, Milan Orlita, Konstantin A. Kokh, Oleg E. Tereshchenko, and Tatyana V. Kuznetsova, "Determination of the Verdet constant in the topological insulator $Bi_{1.1}Sb_{0.9}Te_2S$," Materials Letters **389**, 138325 (2025).

[30] Samy Lalloz, Laurent Davoust, François Debray, and Alban Pothérat, "Alfvén waves at low magnetic Reynolds number: transitions between diffusion, dispersive Alfvén waves and nonlinear propagation," Journal of Fluid Mechanics **1003**, A19 (2025).

[31] Woo Seok Lee, Yeongsu Cho, Katarzyna Posmyk, Paulina Peksa, Mateusz Dyksik, Nicholas Samulewicz, Paulina Plochocka, Michal Baranowski, Heather J. Kulik, and William A. Tisdale, "Excitonic Anisotropy in Single-Crystalline 2D Silver Phenylchalcogenides," Adv. Optical Mater. **13**, e02435 (2025).

[32] Thuc T. Mai, Yufei Li, K. F. Garrity, D. Shaw, T. DeLazzer, R. L. Dally, T. Adel, M. F. Muñoz, A. Giovannone, C. Lyon, A. Pawbake, C. Faugeras, F. Le Mardele, M. Orlita, J. R. Simpson, K. Ross, R. Valdés Aguilar, and A. R. Hight Walker, "Spin-orbital–lattice coupling and the phonon Zeeman effect in the Dirac honeycomb magnet $CoTiO_3$," Physical Review B **111**, 104419 (2025).

[33] Florian le Mardelé, Ivan Mohelsky, Jan Wyzula, Milan Orlita, Philippe Turek, Filippo Troiani, and Athanassios K. Boudalis, "Probing spin-electric transitions in a molecular exchange qubit," Nature Communications **16**, 1198 (2025).

[34] Chiara Massetti, Carolina Crosta, Florian Le Mardelé, Ivan Mohelsky, Christian Martella, Alessandro Molle, Milan Orlita, Carlo Grazianetti, and Fabio Pezzoli, "Quantum confinement effects in the topological Dirac semimetal α-Sn on InSb(111)," Matter **8**, 102194 (2025).

[35] Maxime Massoudzadegan, Sven Badoux, Nicolas Bruyant, Ildar Gilmutdinov, Isaac Haik-Dunn, Gabriel de Oliveira Rodrigues, Nuno Lourenco Prata, Abdelaziz Zitouni, Marc Nardone, Oleksiy Drachenko, Oliver Portugall, Steffen Wiedmann, Benoît Fauqué, David Vignolles, Bertrand Reulet, and Cyril Proust, "First observation of quantum oscillations by transport measurements in semi-destructive pulsed magnetic fields up to 125 T," Rev. Sci. Instrum. **96**, 113904 (2025).

[36] Anne Missiaen, Hadrien Mayaffre, Steffen Krämer, Dan Zhao, Yanbing Zhou, Tao Wu, Xianhui Chen, Sunseng Pyon, Tomohiro Takayama, Hidenori Takagi, David LeBoeuf, and Marc-Henri Julien, "Spin-Stripe Order Tied to the Pseudogap Phase in $La_{1.8-x}Eu_{0.2}Sr_xCuO_4$," Physical Review X **15**, 021010 (2025).

[37] Iman Motie, Brahim Lamine, Alain Blanchard, Rémy Battesti, and Carlo Rizzo, "The optical analogy between a Lorentz-violating cosmos and a magneto-electric medium," The European Physical Journal C **85**, 1048 (2025).

[38] Sagar Paul, Malay Dolai, Juli Nanda Goswami, Biswajit Bhattacharya, Franziska Emmerling, Michael G. B. Drew, Shouvik Chattopadhyay, Rabi Sankar Sarkar, Appu Sunil, Ghenadie Novitchi, Eufemio Moreno-Pineda, and Wolfgang Wernsdorfer, "From strong to weak interaction: reconciling SQUID and μSQUID-EPR data in anomalous Co(II) dimers," Inorg. Chem. Front. **12**, 2025, 12, 6460–6472 (2025).

[39] Amit Pawbake, Florian Petot, Florian Le Mardelé, Tristan Riccardi, Julien Lév̂que, Benjamin A. Piot, Milan Orlita, Johann Coraux, Michal Hubert, Jan Dzian, Martin Veis, Yurii Skourski, Bing Wu, Zdenek Sofer, Benoît Grémaud, Andrés Saúl, and Clément Faugeras, "Magnetic Phases and Zone-Folded Phonons in a Frustrated van der Waals Magnet," ACS Nano **19**, 23693–23702 (2025).

[40] Paulina Peksa, Maciej Ptak, Mateusz Dyksik, Alessandro Surrente, Michal Baranowski, Dawid Drozdowski, Anna Gagor, Julia Osmólska, Agnieszka Kuc, Adam Pikul, Daria Szewczyk, Paulina Plochocka, and Adam Sieradzki, "Tunable Broadband Emission via Self-Trapped Excitons and Mn^{2+} Energy Transfer in a 0D Hybrid Manganese Bromide," Small **21**, e04786 (2025).

[41] Flavia Pop, Nabil Mroweh, Pascale Auban-Senzier, Geert L. J. A. Rikken, Daichi Hirobe, Hiroshi M. Yamamoto, Arkadiusz Frackowiak, Iwona Olejniczak, Sébastien Pillet, El-Eulmi Bendeif, Pere Alemany, Enric Canadell, and Narcis Avarvari, "Chiral Metallic DM-EDT-TTF Radical Cation Salts: Anion Size-Dependent Structural and Electronic Transitions, Charge Ordering, and Chirality-Induced Spin Selectivity," J. Am. Chem. Soc. **147**, 27749–27767 (2025).

[42] Victor Porée, Alberto Zobelli, Amit Pawbake, Jakub Regner, Zden ěk Sofer, Clément Faugeras, and Alessandro Nicolaou, "Resonant x-ray spectroscopies on CrSBr: Probing the electronic structure through chromium $d-d$ excitations," Physical Review B **112**, 125103 (2025).

[43] Pierre Pugnat, Rafik Ballou, Philippe Camus, Guillaume Donnier-Valentin, Thierry Grenet, Ohjoon Kwon, Jérôme Lacipière, Mickaël Pelloux, Rolf Pfister, Yannis K. Semertzidis, Arthur Talarmin, Jérémy Vessaire, and SungWoo Youn, "Progress in GrAHal-CAPP/DMAG for Axion Dark Matter Search in the 1-3 μeV Range," Physical Sciences Forum **11**, 3 (2025).

[44] P. Pugnat, R. Barbier, F. Debray, C. Grandclément, S. Krämer, F. Molinié, R. Pfister, L. Ronayette, B. Vincent, and C. Simon, "The Grenoble Hybrid Magnet: From Commissioning to First Operation up to 42 T," IEEE Transactions on Applied Superconductivity , 1–7 (2025).

[45] Maria Sara Raju, Maxime Aragon-Alberti, Kevin Cardenas, Ivan Breslavetz, Geert L. J. A. Rikken, Cyrille Train, and Matteo Atzori, "Enantioselective Magneto-Chiral Photochemistry Rediscovered," ACS Cent. Sci. **11**, 1147–1153 (2025).

[46] Tristan Riccardi, Suman Sarkar, Anike Purbawati, Aloïs Arrighi, Marek Kostka, Abdellali Hadj-Azzem, Jan Vogel, Julien Renard, Laëtitia Marty, Amit Pawbake, Clément Faugeras, Kenji Watanabe, Takashi Taniguchi, Aurore Finco, Vincent Jacques, Lei Ren, Xavier Marie, Cedric Robert, Manuel Nuñez Regueiro, Nicolas Rougemaille, Nedjma Bendiab, and Johann Coraux, "Laser patterning of the room temperature van der Waals ferromagnet $1T-$CrTe$_2$," Phys. Rev. Mater. **9**, 024001 (2025).

[47] Aleksander Rodek, Mateusz Hajdel, Kacper Oreszczuk, Anna Kafar, Muhammed Aktas, Lucja Marona, Marek Potemski, Czeslaw Skierbiszewski, and Piotr Kossacki, "Hybrid Electroluminescence Device for On-Demand Single Photon Generation at Room Temperature," Adv. Optical Mater. **13**, 2401879 (2025).

[48] L. Rogić, N. Somun, S. Griffitt, A. Najev, M. Spaić, S. Hameed, Y. Shemerliuk, S. Aswartham, M. Orlita, A. Alfonsov, and D. Pelc, "Cryogenic continuous-wave optical spectrometer for sub-thz frequencies," Rev. Sci. Instrum. **96**, 083101 (2025).

[49] Pablo Roseiro, Nadia Ben Amor, Ghenadie Novitchi, Cyrille Train, Saad Yalouz, and Vincent Robert, "Modulated Ligand-Ligand Exchange Coupling and Elusive Spinmerism in a Bis(verdazyl)iron(II) Complex," Inorg. Chem. **64**, 12691–12697 (2025).

[50] F. Schilberth, M.-C. Jiang, F. Le Mardelé, L. B. Papp, I. Mohelsky, M. A. Kassem, Y. Tabata, T. Waki, H. Nakamura, G.-Y. Guo, M. Orlita, R. Arita, I. Kézsmárki, and S. Bordács, "Generation of a nodal line and Weyl points by magnetization reorientation in Co$_3$Sn$_2$S$_2$," npj Quantum Materials **10**, 67 (2025).

[51] Ilya Sheikin, "JPSJ News Comments," J. Phys. Soc. Jpn. **22**, 6 (2025).

[52] Israa Shioukhi, Langit Cahya Adi, Vincent Dorcet, Olivier Cador, Geert L. J. A. Rikken, Boris Le Guennic, Jeanne Crassous, Cyrille Train, Fabrice Pointillart ORCID, Matteo Atzori, and Ori Gidron, "Magneto-chiral dichroism in a chiral twistacene ytterbium(III) one-dimensional assembly of single-molecule magnets," Inorg. Chem. Front. **12**, 5783–5791 (2025).

[53] Y. Skourski, M. D. Kuz'min, K. P. Skokov, N. Shayanfar, A. V. Andreev, S. Zherlitsyn, S. Yasin, L. Zvyagina, O. Drachenko, O. Portugall, and J. Wosnitza, "Orthogonality point and intersublattice exchange in Dy$_2$Fe$_{17}$ determined in strong magnetic fields," Phys. Rev. Mater. **9**, 064404 (2025).

[54] Matheus de Souza Lima Mendes, Langit Cahya Adi, Iryna Makarchuk, Gautier Duroux, Anthony Boudier, Piyanan Pranee, Marion Dosantos Blanco, Jingxian Wang, Christine Labrugère-Sarroste, Eric Lebraud, Sylvain Nlate, Reiko Oda, Cyrille Train, Geert L. J. A. Rikken, Patrick Rosa, Fadi Choueikani, Amélie Juhin, Benoit P. Pichon, Matteo Atzori, Elizabeth A. Hillard, and Emilie Pouget, "Magneto-Chiral Dichroism at the Nanoscale: Experimental Observation in Chiral Paramagnetic Nanoparticles," ACS Materials Lett. , 3853–3858 (2025).

[55] Cristian Andrei Spinu, Ghenadie Novitchi, Mihaela Hillebrand, Teodora Mocanu, Gabriela Ionita, Anamaria Hanganu, Victorita Tecuceanu, and Marius Andruh, "Design of a new nitronyl-nitroxide biradical and its complexes: synthesis, crystal structures and magnetic properties," CrystEngComm **27**, 6462–6472 (2025).

[56] S. Tardieu, N. Ferreira, F. Teyssier, T. Schiavo, O. Drachenko, O. Portugall, and F. Lecouturier-Dupouy, "Mechanical and microstructural changes in Cu single-turn coils revealing the effect of high-speed pressurization, deformation and heating during Megagauss field generation," IEEE Transactions on Applied Superconductivity , 1–4 (2025).

[57] S. Tardieu, C. Verdy, N. Ferreira, F. Teyssier, T. Schiavo, and F. Lecouturier-Dupouy, "Development of Copper-Tungsten Composite Wires Using Cold Spray and Wire-Drawing for High Magnetic Field Applications," IEEE Transactions on Applied Superconductivity (2025), 10.1109/TASC.2025.3626202.

[58] Idris Tlemsani, François Lambert, Nicolas Suaud, Christian Herrero, Régis Guillot, Anne-Laure Barra, Serge Gambarelli, and Talal Mallah, "Assessing the Robustness of the Clock Transition in a Mononuclear S $=1$ Ni(II) Complex Spin Qubit," J. Am. Chem. Soc. **147**, 4685–4688 (2025).

[59] A. Triantafyllidis, J.-R. Marquès, Y. Benkadoum, Y. De León, A. Ciardi, J. Béard, J.-M. Lagarrigue, A. Dearling, N. Ozaki, M. Koenig, and B. Albertazzi, "Dynamics and energy dissipation of collisional blast waves in a perpendicular magnetic field," Phys. Plasmas **32**, 022102 (2025).

[60] A. Triantafyllidis, J.-R. Marquès, S. Ferri, A. Calisti, Y. Benkadoum, Y. De León, A. Dearling, A. Ciardi, J. Béard, J.-M. Lagarrigue, N. Ozaki, M. Koenig, and B. Albertazzi, "Zeeman splitting observations in laser-produced magnetized blast waves," Matter Radiat. Extremes **10**, 047603 (2025).

[61] Mikhail V. Vaganov, Nicolas Suaud, François Lambert, Benjamin Cahier, Christian Herrero, Régis Guillot, Anne-Laure Barra, Nathalie Guihéry, Talal Mallah, Arzhang Ardavan, and Junjie Liu, "Chemical tuning of quantum spin-electric coupling in molecular magnets," Nature Chemistry **17**, 1903 (2025).

[62] T. Vasina, D. Aoki, A. Miyake, G. Seyfarth, A. Pourret, C. Marcenat, M. Amano Patino, G. Lapertot, J. Flouquet, J.-P. Brison, D. Braithwaite, and G. Knebel, "Connecting High-Field and High-Pressure Superconductivity in UTe_2," Physical Review Letters **134**, 096501 (2025).

[63] Arthur Veyrat, Klaus Koepernik, Louis Veyrat, Grigory Shipunov, Iryna Kovalchuk, Saicharan Aswartham, Jiang Qu, Ankit Kumar, Michele Ceccardi, Federico Caglieris, Nicolás Pérez, Romain Giraud, Bernd Büchner, Jeroen van den Brink, Carmine Ortix, and Joseph Dufouleur, "Dissipationless transport signature of topological nodal lines," Nature Communications **16**, 6711 (2025).

[64] Jun Wang, Xingyue Zhang, Chen Wei, Jinshan Li, and Eric Beaugnon, "Microstructure evolution of undercooled binary Co-Sn near eutectic alloys under high magnetic field," Journal of Materials Research and Technology **39**, 9399–9408 (2025).

[65] Zheyu Wang, Lingfei Wang, King Yau Yip, Ying Kit Tsui, Tsz Fung Poon, Wenyan Wang, Chun Wai Tsang, Shanmin Wang, David Graf, Alexandre Pourret, Gabriel Seyfarth, Georg Knebel, Kwing To Lai, Wing Chi Yu, Wei Zhang, and Swee K. Goh, "Discovery of a New Phase in Thin Flakes of KV_3Sb_5 under Pressure," Adv. Sci. **12**, 2415012 (2025).

[66] Dirk Wulferding, Shams Sohel Islam, Youngsu Choi, Gyungbin Ban, Seungyeol Lee, Amit Pawbake, Clément Faugeras, and Kwang-Yong Choi, "Field- and temperature-driven magnetic excitations in rouaite $Cu_2(OH)_3NO_3$," Physical Review B **111**, 064409 (2025).

[67] M. V. Yakushev, T. V. Kuznetsova, D. V. Belyaev, V. I. Grebennikov, M. Orlita, G. Martinez, K. A. Kokh, R. W. Martin, and O. E. Tereshchenko, "Splitting of the absorption edge in the topological insulator $Bi_{1.1}Sb_{0.9}Te_2S$: mid-infrared magneto-optical study," Journal of Physics D: Applied Physics **58**, 145101 (2025).

[68] Yujie Yan, Jun Wang, Chen Wei, Yixuan He, William Yi Wang, Eric Beaugnon, and Jinshan Li, "Experimental quantitative observation of magnetic field accelerated $\gamma - \alpha$ phase transformation in an Fe-based alloy," Journal of Alloys and Compounds **1020**, 179581 (2025).

[69] H. Yang, S. Yi, H. D. Kim, K. C. Je, J. S. Kim, J. H. Kyhm, M. Eto, L. S. Dang, M. Potemski, R. A. Taylor, J. D. Song, and K. Kyhm, "Light-Controlled Optical Aharonov-Bohm Oscillations in a Single GaAs/AlGaAs Quantum Ring," in *Physics of Quantum Rings*, edited by V.M. Fomin (Springer Nature Switzerland, 2025) pp. 317–345.

[70] Zhuo Yang, Toshihiro Nomura, Atsuhiko Miyata, Laurence Eaves, Amalia Patanè, Duncan K. Maude, and Yoshimitsu Kohama, "Magneto-optical transmission spectroscopy up to 60 T of indirect excitons in the van der Waals semiconductor SnSe," Physical Review B **112**, 085203 (2025).

[71] D. Yavorskiy, F. Le Mardelé, I. Mohelsky, M. Orlita, Z. Adamus, T. Wojtowicz, J. Wróbel, K. Karpierz, and J. Łusakowski, "Low-energy excitations in multiple modulation-doped CdTe/(CdMg)Te quantum wells," Physical Review B **111**, 125414 (2025).

[72] Rui Zhou, Igor Vinograd, Michihiro Hirata, Tao Wu, Hadrien Mayaffre, Steffen Krämer, W. N. Hardy, Ruixing Liang, D. A. Bonn, Toshinao Loew, Juan Porras, Bernhard Keimer, and Marc-Henri Julien, "Signatures of two gaps in the spin susceptibility of a cuprate superconductor," Nature Physics **21**, 97–103 (2025).

[73] Rui Zhou, Igor Vinograd, Hadrien Mayaffre, Juan Porras, Hun-Ho Kim, Toshinao Loew, Yiran Liu, Matthieu Le Tacon, Bernhard Keimer, and Marc-Henri Julien, "Robust Charge Density Wave Correlations in Optimally Doped $YBa_2Cu_3O_y$," Physical Review Letters **135**, 106503 (2025).

Collaborating External Laboratories

Belgium
Hasselt University: 29

Canada
Institut Quantique, Sherbrooke: 88
Université de Sherbrooke: 39
University of British Columbia, Vancouver: 39

China
Southern University Shenzhen: 43
State Key Laboratory of Solidification Processing, Northwestern Polytechnical University, Xi'an: 78

Croatia
Faculty of Science, University of Zagreb: 87

Czech Republic
Charles University, Prague: 21,51
Czech Academy of Science, Prague: 51
The Extreme Light Infrastructure ERIC, ELI Beamines Facility, Dolnì Břežany: 80
University of Chemistry and Technology, Prague: 16,17,19,21

France
CEA, INP, IRIG, PHELIQS, Grenoble: 42
CEA, LETI, Grenoble: 32
CEA-Saclay, Gif-sur-Yvette: 93,94
CELIA, University of Bordeaux-CNRS-CEA, Talence: 80
CINaM, Marseille: 21
CIRIMAT, CNRS-UPS-INP, Toulouse: 100
DACM-IRFU-CEA, Université Paris-Saclay: 73
ENS de Lyon: 47
G2Elab, Grenoble: 95,96
GenF, Elancourt: 80
Grenoble-INP, Université Grenoble Alpes: 96
ICB-LERMPS-UTBM, Belfort: 98
ICMMO, University Paris-Saclay, Orsay: 56
INRS EMT, Varennes: 80
Institut Clément Ader, CNRS, Université Toulouse III: 89
Institut Néel, CNRS, Grenoble: 18
Institut Néel, CNRS, University Grenoble Alpes: 82
IMPMC-CNRS, Sorbonne Université, Paris: 58
IRIG-PHELIQS, CEA Grenoble: 40,43
IRSAMC, University of Toulouse: 56
ISCR-CNRS, University of Rennes: 59
JEIP, Paris: 88
L2C, University of Montpellier: 18
Laboratoire de Physique Théorique, Toulouse: 47
Laboratoire pour l'Utilisation des Lasers Intenses (LULI), CNRS-CEA-Ecole Polytechnique-Université Paris VI, Palaiseau: 79,80,81
LPCNO, INSA, Toulouse: 18
LPSC, CNRS, University Grenoble Alpes: 82
Plateforme Nationale CNRS de Frittage Flash, Toulouse: 100
SIMAP, INP-Grenoble: 77
Sorbonne Université, Observatoire Paris, Université PSL, CNRS, Laboratoire d'Etude de l'Univers et des Phénoménes Extrêmes (LUX) Paris: 79,81
SyMMES, CEA, Grenoble: 56
Synchrotron SOLEIL, Gif-sur-Yvette: 19
Synchrotron SOLEIL, Saint-Aubin: 58

Institute of High Pressure Physics, Warsaw: 51
Polish Academy of Sciences, Warsaw: 51
University of Warsaw: 13,29,51
Wroclaw University of Science and Technology: 14,15,16,17,26,27,28,29,30

Romania
ELI-NP, “Horia Hulubei” National Institute for Physics and Nuclear Engineering, Bucharest-Magurele: 80
Faculty of Chemistry, University of Bucharest: 55
Institute of Organic and Supramolecular Chemistry, Romanian Academy: 55
Institute of Physical Chemistry, Romanian Academy: 55

Singapore
National University of Singapore: 20

Slovakia
Institute of Electrical Engineering, Slovak Academy of Sciences, Bratislava: 66

South Korea
IBS-DMAG, Daejeon: 82
Sejong University, Seoul: 48
Sungkyunkwan University, Suwon: 48

Spain
Institut de Ciència de Materials de Barcelona ICMAB-CSIC, Bellaterra: 63

Sweden
Chalmers University of Technology, Gothenburg: 14

Switzerland
CERN, Geneva: 64
DQMP, University of Geneva: 66
University of Zurich: 38

The Netherlands
HFML, Nijmegen: 88
HFML, Radboud University, Nijmegen: 66
Institute of Physics, University of Amsterdam: 31
University of Twente, Enschede: 66

United Kingdom
Cavendish Laboratory, University of Cambridge: 30
Coventry University: 77
King’s Collage London: 16
Oxford Instruments NanoScience, Abingdon: 66
University of Bath: 32
University of Nottingham: 25
University of Sheffield: 28
York Plasma Institute, University of York: 79,81

USA
Colorado State University, Fort Collins: 49
Massachusetts Institute of Technology, Cambridge, Massachusetts: 15
National Renewable Energy Laboratory, Golden: 16
NIST, Gaithersburg: 49
NHMFL, Tallahassee: 43
The Ohio State University, Columbus: 49

Author Index
(Contributors of LNCMI to this annual report)

INDEX

CONTINUOUS MAGNETIC FIELDS
LNCMI-G, CNRS
25 avenue des Martyrs, B.P. 166
38042 GRENOBLE cedex 9 - France
Tel : +33 (0)4 76 88 10 48

PULSED MAGNETIC FIELDS
LNCMI-T, CNRS
143 avenue de Rangueil
31400 TOULOUSE - France
Tel : +33 (0)5 62 17 28 60

direction@lncmi.cnrs.fr
https://www.lncmi.cnrs.fr

LNCMI is a founding member of EMFL

Création couverture : Alexandra GASPARINI, LNCMI
Photos : Service communication DR11 / Jérôme BEARD, LNCMI / Graal, LNCMI / Ilya Sheikin, LNCMI